Joana Patrícia Machado Morgado
Bachelor of Science

Absorbed dose maps of patients submitted to ^{68}Ga-PSMA-11 PET/CT

Dissertation submitted in partial fulfillment of the requirements for the degree of
Master of Science in
Biomedical Engineering

Advisers: Paulo Ferreira, Medical Physics Expert and Researcher
at the Nuclear Medicine-Radiopharmacology Department,
Champalimaud Foundation

Ricardo Vigário, Assistant Professor,
NOVA University of Lisbon

FACULDADE DE
CIÊNCIAS E TECNOLOGIA
UNIVERSIDADE NOVA DE LISBOA

November, 2020

Absorbed dose maps of patients submitted to ^{68}Ga-PSMA-11 PET/CT

To my mother

Acknowledgments

I would like to express my gratitude to Professor Doctor Durval C. Costa for having me welcomed in the group of Nuclear Medicine-Radiopharmacology at the Champalimaud Foundation. Thank you for the valuable transmitted knowledge and for always demanding my best.

I would like to thank my advisor Doctor Paulo Ferreira for constantly being available to provide the guidance and support needed, always allowing me to discuss my thoughts on the work done.

To Doctor Salvatore di Maria, thank you for your valuable work on calculating the S-values, explanations, and clarifications about the Monte Carlo software.

I would also like to thank Professor Doctor Ricardo Vigário for his eagerness to help me at any moment, motivating me with challenging and valuable advice.

To my college friends, thank you for the moments of true happiness and for being the listeners I needed in the most challenging days during these five years.

Last but not least, a special acknowledgment to my family, especially my parents Alzira, João, and sister Ana, by unconditionally encouraging me throughout this journey. Thank you for all the patience and care given to me at all times.

Abstract

Although nuclear medicine (NM) procedures are highly effective diagnostic tools, they have been contributing significantly, together with other medical diagnostic and therapeutic methodologies, to the increase in exposure to ionizing radiation in recent years. There is an urgent need to optimize NM techniques, to maintain diagnostic quality at a minimum possible radiation absorbed dose. ^{68}Ga-prostate-specific membrane antigen positron emission tomography/computed tomography (^{68}Ga-PSMA-11 PET/CT) imaging has rapidly gained notoriety in the NM field and, at the same time, personalized dosimetry studies using voxel-based methods have been performed. This study aimed to calculate the absorbed dose at the voxel level in the kidneys, liver, spleen, and red bone marrow, compare the results with other studies and draw conclusions regarding the safety of using ^{68}Ga-PSMA-11 in NM clinics.

Whole-body PET/CT images from six patients were acquired after a single ^{68}Ga-PSMA-11 injection. After registration of the CT and PET images, the target organs were manually segmented in the CT and resampled to the PET voxel size. Voxel S-values were computed for specific tissues using the Monte-Carlo N-Particle transport 6.1 code. The absorbed dose rates were obtained by convolution of the PET activity images with the specific S-values of each tissue. A time integral was then applied to each distribution to account for all ^{68}Ga decay. Statistical dose values were computed and compared with the available literature.

Considering all the patients included in this study, the kidneys received the highest radiation, with a mean overall absorbed dose of 0.0561 mGy/MBq and a median overall absorbed dose of 0.0499 mGy/MBq. In contrast, the red bone marrow received the lowest absorbed dose values (mean dose: 0.0015 mGy/MBq, median dose: 0.0013 mGy/MBq). The present study showed lower dosimetry values than the literature, resulting in deviations ranging from -38.1% (in the liver) to -91.3% (in the red bone marrow).

The present study employs a voxel-based approach, which considers a non-uniform biodistribution of the radiopharmaceutical in the organs and leads to dosimetry estimates closer to the real ones. The reasonable low absorbed doses in the four organs herein studied is an argument in favor of using ^{68}Ga-PSMA-11 in NM clinics. In the Future Work chapter, a more specific dynamic NM imaging methodology, taking into consideration the radiopharmaceutical pharmacokinetics, is presented.

Keywords: Nuclear Medicine, Positron Emission Tomography, Voxel-based Dosimetry, Absorbed dose

Resumo

Embora os procedimentos em medicina nuclear (do inglês, *Nuclear Medicine,* NM) sejam ferramentas de diagnóstico altamente eficazes, nos últimos anos têm contribuído de forma significativa, juntamente com outros meios de diagnóstico e terapêutica, para o aumento da exposição à radiação ionizante. Existe uma necessidade urgente de otimizar as técnicas de NM, o que implica manter a qualidade de diagnóstico com a mínima dose de radiação absorvida possível. A tomografia por emissão de positrões/tomografia computorizada com ^{68}Ga acoplado ao antigénio de membrana específico da próstata (do inglês, *^{68}Ga-prostate-specific membrane antigen positron emission tomography/computed tomography*, ^{68}Ga-PSMA-11 PET/CT) tem adquirido rapidamente notoriedade no campo de NM, e têm sido realizados estudos de dosimetria personalizada ao nível do voxel. Este estudo teve como objetivo calcular a dose absorvida ao nível do voxel nos rins, fígado, baço, e medula óssea vermelha, comparar os resultados com outros estudos e tirar conclusões relativamente à segurança da utilização do ^{68}Ga-PSMA-11 nas clínicas de NM.

Após uma única injeção de ^{68}Ga-PSMA-11 foram adquiridas imagens de PET/CT de corpo inteiro em seis doentes. Após o registo das imagens CT e PET, os órgãos-alvo foram segmentados manualmente no CT e reamostrados para o tamanho de voxel do PET. Os *S-values* ao nível do voxel foram obtidos para tecidos específicos usando a versão 6.1 do código de simulação Monte Carlo. As distribuições de taxa de dose absorvida foram calculadas através de operações de convolução das imagens de atividade PET com os *S-values* específicos de cada tecido. Uma integração temporal foi então aplicada a cada distribuição para contabilização de todos os decaimentos do ^{68}Ga. Os valores estatísticos destas distribuições de dose absorvida nos órgãos em estudo foram depois calculados e comparados com a literatura disponível.

Considerando todos os pacientes incluídos neste estudo, os rins receberam os valores mais altos de dose absorvida, com uma dose média global de 0.0561 mGy/MBq e uma dose absorvida mediana global de 0.0499 mGy/MBq. Por outro lado, a medula óssea vermelha recebeu os valores mais baixos de dose absorvida (dose média: 0.0015 mGy/MBq, dose mediana: 0.0013 mGy/MBq). O presente estudo obteve valores dosimétricos inferiores aos da literatura, originando desvios que variaram entre -38.1% (no fígado) e -91.3% (na medula óssea vermelha).

O presente estudo seguiu uma abordagem ao nível do voxel, que considera uma biodistribuição não uniforme do radiofármaco nos órgãos e conduz a estimativas dosimétricas mais próximas das reais. As baixas doses absorvidas nos quatro órgãos aqui estudados é um argumento a favor do uso de ^{68}Ga-PSMA-11 em clínicas de NM. No capítulo final deste trabalho, é apresentada uma metodologia de aquisições dinâmicas mais específica que tem em consideração a farmacocinética do radiofármaco.

Palavras-chave: Medicina Nuclear, Tomografia por Emissão de Positrões, Dosimetria a nível do voxel, Dose absorvida

Contents

List of Figures

List of Tables

Abbreviations

^{68}Ga-PSMA-11	^{68}Ga-Prostate-specific Membrane Antigen
ALARA	As Low As Reasonably Achievable
BGO	Bismuth Germanate
CCC	Champalimaud Clinical Centre
cDVH	cumulative Dose-volume Histogram
CT	Computed Tomography
DICOM	Digital Imaging and Communications in Medicine
DPK	Dose-Point Kernel
DVH	Dose-volume Histogram
EANM	European Association of Nuclear Medicine
EGS	Electron Gamma Shower
FOV	Field-of-View
HU	Hounsfield Unit
IAEA	International Atomic Energy Agency
ICRP	International Commission on Radiological Protection
ICRU	International Commission on Radiation Units and Measurements
LOR	Line-of-Response
LSO	Lutetium Oxyorthosilicate
MCNP	Monte-Carlo N-Particle Transport
MIRD	Medical Internal Radiation Dose
NIfTI	Neuroimaging Informatics Technology Initiative
NM	Nuclear Medicine
PET	Positron Emission Tomography
PMT	Photomultiplier Tube
ROIs	Regions-of-Interest
SD	Standard Deviation

SNMMI	Society of Nuclear Medicine and Molecular Imaging
TOF	Time-of-Flight

1

Introduction

1.1 Context and Motivation

Nuclear medicine (NM) is a medical specialty that uses radioactive isotopes to examine organ function and structure for diagnosis, therapy, and biomedical research. It plays an important role in modern medicine since it offers the potential to identify disease (appearance, progress, or recurrence) in its earliest stages and, consequently, makes treatment more effective [1].

Hybrid technology – positron emission tomography/computed tomography (PET/CT) – combines the strengths of the two well-established image modalities. PET molecular imaging measures tumor metabolic activity, providing insight into biological processes, while CT highlights anatomical information about the tumor and its involvement in adjacent organs and vasculature. PET/CT scanner hybrids facilitate localization and interpretation of tumors and metastases, treatment planning, and follow-up monitoring in a non-invasive way. Therefore, this imaging technology is established in clinical practice and has added significant value in the areas of neurology, cardiology, and, especially, oncology [2].

Labeling of prostate-specific membrane antigen (PSMA) with the ^{68}Ga radionuclide leads to the formation of the ^{68}Ga-prostate-specific membrane antigen (^{68}Ga-PSMA-11) radiopharmaceutical. This radiotracer has been identified as the most promising radiopharmaceutical for imaging prostate cancer primary disease, recurrence, and metastasis [3]. There is an ongoing widespread adoption of ^{68}Ga-PSMA-11 PET/CT imaging in diagnosis, staging, and restaging of prostate cancer in recent years. Despite being mainly used in patients with prostate cancer, there have been reports of its application in patients with other malignancies with increase PSMA expression.

Regarding the imaging equipment, Philips Vereos Digital PET/CT is the first truly digital PET/CT scanner. This type of machine has higher temporal and spatial resolution than any analog

PET/CT commonly used in NM clinics. It offers improved detectability and characterization of malignancies for a fast, simple, and confident path staging and treatment monitoring [4]. Philips Vereos Digital PET/CT is available at the Champalimaud Foundation, and images from this scanner were used in this study.

Medical application of ionizing radiation is a massive and increasing activity globally. While the use of ionizing radiation in medicine brings tremendous benefits to the global population, the associated risks due to stochastic (e.g., cancer) and deterministic (e.g., skin injuries) effects make it necessary to protect patients from potential harm. Thus, after almost 70 years of using radionuclides for diagnostic purposes, there is now a rapidly increasing awareness of the need to assess risk as soon as possible to ensure the safe use of radioactively labeled drugs in medical practice [5]. This fundamental change is being spurred on by the need for evidence-based medicine and the emerging interest in voxel dosimetry and personalized treatment. Procedures that utilize ionizing radiation should be performed in accordance with the As Low As Reasonably Achievable (ALARA) philosophy. This principle states that the radiation activity and consequent absorbed dose should be as low as possible for the patient, ensuring that tracer uptake in target structures is discernible [6]. This type of evaluation and the analysis of dose distribution in patients after administration of ^{68}Ga-PSMA-11 are crucial for its adoption within multicenter trials. Therefore, a study on the absorbed dose received by patients and dose mapping is imperative, this being the motivation for this study.

1.2 Objectives and dissertation plan

The primary objective of this dissertation is to assess the whole-body absorbed doses of a set of patients from the NM Department of the Champalimaud Foundation, based on ^{68}Ga-PSMA-11 PET/CT imaging. With this goal in mind, statistical analysis of patient doses was computed from images acquired by a digital PET/CT – VEREOS-. Then, these values were compared with the data present in the literature.

The present dissertation has been structured to first cover (chapter 1) the current state-of-the-art concerning PET/CT equipment, the use of ^{68}Ga-PSMA-11 as a radiopharmaceutical in NM, the absorbed dose calculation using the Medical Internal Radiation Dose (MIRD) schema at the voxel level and its relevance in NM clinicals. In chapter 2, theoretical concepts of CT, PET, and hybrid PET/CT system, essential to medical image acquisition, are described. Afterward, the biological effects of radiation, internal voxel-dosimetry, and dose-volume histograms (DVHs) are described in chapter 3. In chapter 4, the materials and methods used for imaging processing and statistical analysis are presented. In the following chapter 5, the results are presented, including

the statistical analysis and evaluation of each organ absorbed doses and the respective DVHs. Lastly, the discussion and conclusions are addressed in chapter 6, including the limitations of the present study and possible directions for future works.

1.3 State-of-the-art

NM has gained more notoriety since the introduction of the first PET/CT scanner in 1998 [7]. PET/CT is now widely used in routine clinical settings for cancer diagnosis, staging and restaging, treatment planning, and treatment monitoring [8-12]. Moreover, it is used as a prognostic indicator based on standardized uptake values (SUVs) [13]. Currently, almost 95% of new PET scanners sold are hybrid PET/CT scanners [14], and 90% of clinical workloads are for oncology research [15]. Studies have shown that interpretation of co-registered and fused PET and CT images leads to a 30% to 50% improvement in the observer confidence of lesion localization and a 4% to 15% improvement in the overall accuracy of staging/restaging by comparison with PET alone, CT alone, and visually correlated PET and CT [15-19].

Vereos PET/CT was unveiled in 2013 by Philips Healthcare as the first commercially available Food and Drug Administration-approved digital PET scanner [20]. Nguyen and his colleagues showed that this digital scanner provides better image quality, diagnostic performance, and accuracy than analog PET scanners [20]. These improvements result from the implementation of high-performance digital detectors and single-photon avalanche photodiodes with low-voltage complementary metal-oxide semiconductors. Additionally, improved system corrections and reconstruction parameters increase the spatial and time-of-flight (TOF) resolution [21, 22].

^{68}Ga began to be clinically applied in the early 1960s in studies of the central nervous system [23]. However, this radioisotope only began to be clinically used in NM when coupled with PSMA inhibitors by Eder and his colleagues [24]. PSMA is a transmembrane protein expressed in several tissues, including the small intestine, proximal renal tubules, and salivary glands. Additionally, due to the neo-vascularization process, it may be found in a variety of malignancies, including intestinal, renal, lung, and breast cancers [25]. However, its expression is increased up to 10000-times in prostatic cancer cells [16, 26-30] and is a significant prognosticator for disease outcome [31]. ^{68}Ga-PSMA-11 PET/CT is the most useful diagnostic tool for prostate cancer screening worldwide, as it offers excellent contrast between the tumor and the background, also known as the target-to-background ratio, leading to an improved detection rate of prostate cancer primary disease, recurrence, or metastasis [30, 32-35]. It has also been shown to detect lymph nodes, soft tissue, and bone metastases with high sensitivity and specificity [33] and has been used to aid decision making by confirming or eliminating the need

for biopsies [36-38]. Several studies have shown that ^{68}Ga-PSMA-11 PET/CT detects with high accuracy primary prostate cancer, biochemical recurrence [39, 40], and metastases even at low prostate-specific antigen (PSA) levels [38, 41-43]. Moreover, two recent studies have shown that ^{68}Ga-PSMA-11 PET/CT performs better than bone scintigraphy in determining overall bone involvement in prostate cancer patients [44, 45]. In addition, a study by Grubmuller and his colleagues highlights the enhanced ability for ^{68}Ga-PSMA-11 PET to detect distant sites of disease compared to standard imaging with CT only [46].

Apart from natural background radiation, medical procedures are the largest source of exposure to ionizing radiation for the population [47]. Every day, more than 1000 000 NM diagnostic procedures are performed all over the world, increasing the exposure of populations to ionizing radiation and, consequently, increasing the absorbed doses by people [48]. This dramatic increase in the use of ionizing radiation in medical diagnostic practice has been the subject of several concerns, with the American College of Radiology (ACR) White Paper noting that "The rapid growth of CT and certain NM studies may result in an increased incidence of radiation-related cancer in the not-too-distant future" [49]. The radiation exposure to the patient depends on the PET component of the PET/CT scanner image acquisition and processing features and the selection of an appropriate radiopharmaceutical and its activity [50]. Radiation dosimetry studies are essential to determine the relationship between absorbed dose and toxicity, characterize the safety and efficacy of radiopharmaceuticals, and choose a personalized treatment for each patient [51]. The ultimate goal is to perform examinations with the minimum possible radiation exposure without hampering the diagnostic purpose. Currently, as exposures are not subject to regulatory equivalent dose limits in the medical imaging field, radiation protection is underpinned by the concepts of justification and optimization [47, 52]. In its 1990 and 2007 recommendations, the International Commission on Radiological Protection (ICRP) stated as a principle of justification that "Any decision that alters the radiation exposure situation should do more good than harm" [53, 54]. A stronger position on the justification of medical exposures is expressed in the International Atomic Energy Agency (IAEA) 2007 Justification Consultation report, which states that the "good" (i.e., the benefits) should substantially outweigh the risks that may be incurred, in part because of the uncertainty of the risks [55]. Hence, all individual medical exposures should be justified in advance, taking into account the specific objectives of the exposures and the characteristics of the individual involved. Furthermore, according to the safety protocol known as ALARA, the dose should be kept "as low as reasonably achievable, economic, and social factors being taken into account" [6].

Internal absorbed doses from radiopharmaceuticals are usually calculated using the international dosimetry schema of the MIRD Committee of the Society of Nuclear Medicine for both

diagnostic and therapeutic purposes. This formalism was originally published in the MIRD Pamphlet No. 1 [56] in 1968 to reach standardization of the absorbed dose to whole organs, tissue subregions, sub-organ, and cellular levels. Internal radiation dosimetry at the voxel-level has been increasingly implemented since the traditional model of activity being uniformly irradiated and distributed in the organs no longer applies. Thus, Monte Carlo simulations are used to calculate absorbed dose rates per unit cumulated activity (expressed in mGy/(MBq·s), also known as S-values. These, together with the accumulated radiopharmaceutical activities, are employed in the absorbed dose calculation. The absorbed dose in various organs after the administration of the radiopharmaceutical under study, ^{68}Ga-PSMA-11, can be consulted in several studies [57-61]. To calculate a tomographic (3D) map of the absorbed dose, the activity quantification in organs can be performed by delineating regions of interest (ROIs) in PET/CT images through segmentation. Manual segmentation of organs, such as the liver, stomach, spleen, and kidneys, is uncertain and difficult. However, Leong and his colleagues have shown that visual manual segmentation of PET/CT images is more accurate and reproducible than thresholding-based semiautomatic segmentation methods [62, 63]. Furthermore, if registration of images is required during image processing, rigid registration has shown to achieve good alignment between baseline and evaluation scans [64].

2

Hybrid PET/CT system

PET/CT is a non-invasive imaging modality that combines the possibility of obtaining detailed anatomical images, from CT, with the capability to obtain functional images from PET, all in one examination. This system has the advantage of allowing both the mapping of the distribution of radiotracers in the human body and acquiring anatomical information about the localization of the pathology on the same volume. Also, in PET/CT, CT data can be transformed into attenuation coefficients for PET through mathematical algorithms to provide quick photon attenuation correction with little noise. The hybrid PET/CT imaging system was introduced in clinical practice in 1998 and, since then, has been revolutionizing the clinical context due to the speed, convenience, and precision with which this system obtains images of the objects under study [65].

2.1 Computed Tomography

CT is a conventional radiation technique that uses sophisticated x-ray technology to generate detailed anatomical images. X-rays are high energy photons with energies ranging from 10^3 eV to 10^6 eV and are produced in an x-ray tube [66].

CT records a tissue densities pattern, based on the attenuation coefficient of the tissues crossed by the x-ray beam. This means that by detecting the x-rays that pass through the 3-dimensional patient volume (i.e., tomographically), attenuation and location are measured by the detectors and used to reconstruct a 3D image. The higher the tissue's attenuation, the brighter the tissue appears in the gray-scale image, and vice-versa. Hence, the bone appears as white on the digital detectors, while the lungs, mostly composed of air, appear dark in the image.

Since it was introduced in 1972 by the British engineer Godfrey Newbold Hounsfield, CT has revolutionized not only the diagnosis in radiology but the entire field of medicine [67]. In NM, CT has been growing with the introduction of the PET/CT systems. CT scanners currently used for clinical operations can achieve a spatial resolution of about 0.3 mm, and depending on the number of slices intended, two techniques are used to perform this exam: helical scan mode (patient bed moves continuously during the scan) and CT multislice (bed moves step-by-step during the scan) [68].

2.1.1 Photon interaction with matter

When a photon (which may be an x-ray or a gamma ray) interacts with matter, it can transfer all or part of its energy to the medium. When this happens, it can promote the ionization or excitation of the constituent atoms of the absorbent material. Depending on the energy of the electromagnetic radiation and the type of material, photons interact with matter by three dominant mechanisms: photoelectric effect, Compton scattering, and pair production. Considering the range of energies produced by CT scanners, only the first two interactions will be analyzed in detail.

The photoelectric effect involves the interaction of an incident photon with an orbital (generally inner shell) electron that has a similar but smaller binding energy than the energy of the incident photon. In this effect, the energy of the impinging photon is locally deposited, resulting in its total absorption, and the ionization of the atom occurs (Figure 2.1-A). While the photoelectron is ejected with a kinetic energy equal to the difference of the incident photon and the electron binding energy, the residual atom is left in an excited state. Thus, characteristic x-rays, with energy equal to the difference in electron binding energies for the different electron levels, can be produced since the emitted electron left a free orbital. This orbital is then filled by a less bound and more energetic electron from the external orbitals (from the L or M shell).

Compton scattering is an interaction in which an incident photon transfers part of its energy to an outer shell electron, ejecting it from the atom. A portion of the photon energy is transferred to the electron, causing a recoil and subsequent removal from the atom in a forward direction relative to the angle of the impinging photon. After the interaction, as the photon undergoes a change in direction, the remainder of the energy is transferred to this scattered photon that may travel to any direction between 0º and 180º. The scattering angle is proportional to the amount of energy lost (Figure 2.1-B) [69].

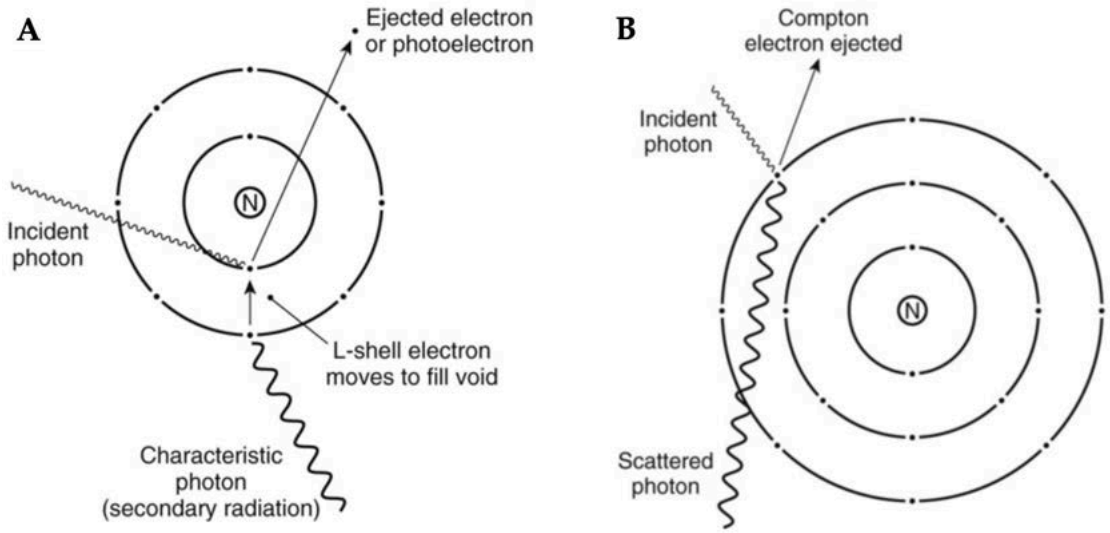

Figure 2.1: Illustration of the photoelectric effect and Compton scattering: A) The photoelectric effect, as illustrated, involves the total transfer of energy from the incident photon to an orbital electron, causing the ionization of the atom and consequently the formation of a free electron and a positive charged atom. Subsequently, characteristic x-rays are emitted. B) In the Compton scattering interaction, the incident photon transfers part of its energy to an outer shell electron. While the electron is ejected, the photon is scattered at an angle proportional to the amount of energy lost. Adapted from [70].

2.1.2 Photon attenuation in matter

As a result of the interactions between photons and matter, the number of detected photons decreases as the beam passes through this attenuator. More specifically, the intensity I of the detected photons is expressed as:

$$I = I_{\mathrm{o}} e^{-\mu x} \tag{2.1}$$

where I_{o} is the number of source photons, μ is the linear attenuation coefficient, and x is the thickness of the attenuator.

The linear attenuation coefficient depends on the energy of the incident photon and the average atomic number and thickness of the attenuator [69]. As a consequence, the images that CT scanners produce are gray-scaled maps of the spatially varying linear attenuation coefficients of the tissues since this coefficient is higher for dense tissue compared to soft tissue.

CT pixel intensities are given in the Hounsfield unit (HU) scale and are simply attenuation units measured by CT. The scale is defined so that the reference, water, has a value of 0 HU and air a value of -1000 HU [69]. The Hounsfield units are used to reduce energy dependence and are very important in medicine when it is necessary to find the type of tissue being examined. This unit is often employed in voxel-wise 3D absorbed dose calculations.

2.1.3 X-ray production

An x-ray tube is a glass or ceramic vacuum tube composed of a cathode, an anode, an electronic focusing cup, a window, a filter, and a collimator (Figure 2.2). First, an electrical current is applied to heat the negative electrical potential, the cathode, so that electrons are emitted through thermionic emission from a charged metal filament. Then, the electrons are accelerated toward the positive electrical potential, the anode, due to the high potential difference (between 25 and 150 kV_p in diagnosis [71]) maintained by these two structures. The more heated the filament (i.e., filament current), the more electrons will be emitted, and the greater will be the electrical current that flows between the cathode and the anode (i.e., tube current). When the electrons, oriented by the electronic focusing cup, reach the anode target, the majority interact with outer-shell electrons of the anode, and their kinetic energy is lost as heat. Only approximately 0.2% of these electrons generate the emission of an x-ray by either characteristic or bremsstrahlung x-rays [65].

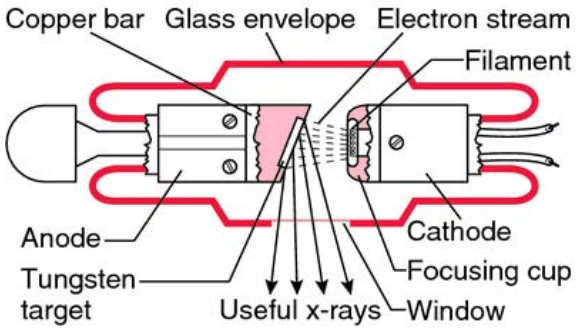

Figure 2.2: X-ray tube diagram in longitudinal section. The heated cathode emits electrons that are accelerated by the high potential difference between the cathode and anode. The electron stream is collected in the anode. The interaction of the electrons with the anode material produces characteristic and bremsstrahlung x-ray photons. This is the beam that interacts with the patient [72].

Characteristic x-rays are generated in electronic transitions in an atom. An electron, when decelerating, can collide with the electrons from the inner or outer layers shells of the anode atoms, causing ionization or excitation. If it has enough energy, the electron can even eject an electron. Consequently, a photon with an energy proportional to the difference between the initial and final energy states is released (i.e., characteristic x-ray photons with discrete energy values). On the other hand, bremsstrahlung x-rays are generated by electrons acceleration and posterior deceleration. This incidence happens when an electron interacts with the Coulomb electric field of a nucleus and is either deflected from its linear path or varies its velocity, irradiating radiative energy proportionally to its acceleration. The energy distribution of bremsstrahlung radiation is continuous and extends up to the energy of the incident electron, unlike characteristic x-rays, which exhibit a discrete energy spectrum. At the end of this process, this electromagnetic radiation

exits the tube through the window towards the patient's body. A collimator, usually made of lead, is fixed to narrow the x-ray beam and avoid radiating tissues other than those under study.

Due to the x-ray tube development, it was possible to construct the CT scanner, which emits radiation while revolving around the patient. The x-rays are later detected on the opposite side by detectors. The basic elements and operations involved will be discussed in the following section.

2.1.4 Instrumentation

The basic components of a CT scanner are an x-ray tube and a detector ring positioned around the patient's bed, contained in a gantry.

In most current scanners, data is recorded over a 360º path, and the x-ray source is moved mechanically in increments around the patient. The tube is turned on at each position, and the patient is exposed to a narrow (from 0.5 to 20 mm thickness) beam of x-rays. Consequently, multiple images, called projections, are collected and digitalized to be "back-projected" and create transaxial slices.

Within the past decade, the development of third-generation systems with multislice has changed the scope of CT technology (Figure 2.3). These "rotate-rotate" systems consist of a rotating source and a rotating ring of detectors that move simultaneously around the patient. They accommodate larger multirow detector arrays that provide multislice acquisition capability and a greater irradiation volume of the patient. With these systems, it is possible to acquire several slices simultaneously, and subsequently, the acquisition time decreases to just 5-20 seconds to obtain full body images [71]. Consequently, the number of artifacts related to the patient's movement decreases, providing a more well-defined image, and a shorter x-ray exposure is delivered to the patient, resulting in reduced absorbed dose values. Also, the field-of-view (FOV) is increased, contributing to the production of non-overlapping images. Some of the disadvantages include increased noise with decreased slide thickness, increased cost due to the increased number of detectors, and a possible increase in x-ray exposure when thin sections with high quality are intended.

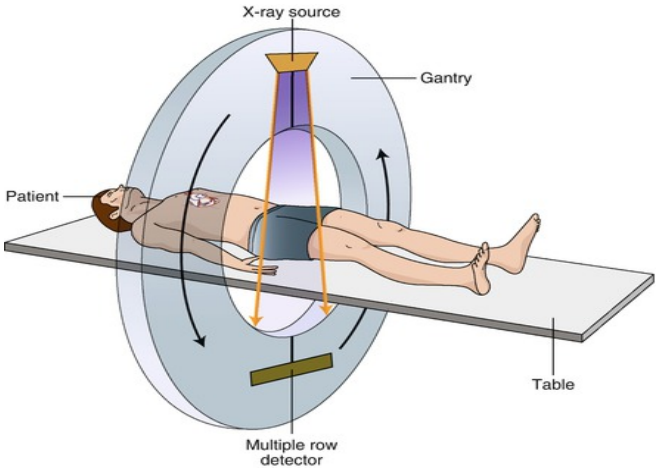

Figure 2.3: Illustration of a third-generation CT system with multislice. These scanners employ a "rotate-rotate" geometry, in which both the x-ray source and the detector rotate about the patient. In a multislice system, the attenuation of the patient is measured by each detector that integrates a narrow multi-row detector array [71].

Furthermore, newer CT scanners, introduced in the early 90s, acquire slices continuously as the bed advances uninterruptedly and are called helical scanners [65]. Consequently, new advantages, such as faster scanning times (a complete exam is performed in approximately 30 seconds) and increased flexibility during data reconstruction, emerge [71].

The detectors used in CT scanners are mainly composed of solid ceramic scintillators, characterized by emitting a light distribution in response to x-rays. In these detectors, the incident radiation causes excitation of tightly bound electrons, which become free to migrate. An electric field is then applied to generate a flow of charge through the detector. The ceramic scintillators are coupled to photodiodes. These are semiconductors responsible for converting light photon energy into current or electrical pulses. The resulting signal is processed on specific computer software and converted into a density-weighted image (i.e., grayscale image calibrated in HU).

2.2 Positron Emission Tomography

PET is a biomedical functional imaging technique used to localize metabolic processes in a fast, whole-body, and non-invasive real-time quantitative assessment. PET applies coincidence detection to display the body's biochemistry, depending upon the choice of the radiopharmaceutical administered to the patient.

This imaging modality has been widely used in diagnostic medicine and clinical pharmaceutical research. Its principal applications include oncology, cardiology, and neurology [2]. Since the early detection of metastases can have a massive impact on overall patient outcomes, peptide receptors with over-expression on tumor metastases have become promising biological

targets in nuclear oncology. In this module, the radiopharmaceutical ^{68}Ga-PSMA-11 will be analyzed in detail.

The advantages of this technique include high temporal resolution and sensitivity, and accurate detection and quantification of tracer, even in small size lesions. PET imaging also enables the quantification of radiopharmaceutical uptake kinetics, dynamic image reconstruction, and simpler dosimetry estimations. In the last decade, PET detectors and instrumentation have been developed into sophisticated clinical tools to improve diagnostic conditions, and PET scanners have been substituted for hybrid PET/CT scanners. However, the principal disadvantages are the added cost of the equipment and the short half-life of some of the most useful positron radiation emitters, whose synthesis is very costly and time-consuming [73].

Considering all these advantages and disadvantages, PET is one of the most precise imaging techniques currently in use, allowing physiology and pathology evaluations early in disease processes, individualize treatment selection, and planning and monitoring of treatment response.

2.2.1 Radioactive decay

Radioactive decay consists in the release of energy from the nucleus of an unstable atom through the emission of electromagnetic radiation or charged particles. It proceeds spontaneously at a given moment in time and is of a probabilistic nature. The radioactive decay can occur successively, generating a chain of disintegrations, until reaching a stable element, and it takes the form of an exponential decay function.

Thus, the number of atoms (N) decaying at a moment in time t is determined by the number of unstable radioactive nuclei at an initial time, N_0, and the decay (probability) constant of the radionuclide λ, as represented in Equation 2.2.

$$N(t) = N_0 e^{-\lambda t} \tag{2.2}$$

The number of atoms decaying per time unit, after a time t, is called activity (A), as defined in Equation 2.3, and is dependent on the activity presented initially A_0 and, as already mentioned, on the decay constant λ.

$$A(t) = A_0 e^{-\lambda t} \tag{2.3}$$

The SI unit of activity is the Becquerel (Bq). One becquerel equals one disintegration per second. In NM, the activity is often expressed in Megabecquerel (MBq), which corresponds to 10^6 Bq.

The decay constant λ is defined as the probability that one unstable radioactive nucleus, out of *N*, decays in a time unit. Each decay constant is dependent on its respective half-life $T_{1/2}$ and is given by:

$$\lambda = \frac{\ln 2}{T_{1/2}} = \frac{0.693}{T_{1/2}} \tag{2.4}$$

In radiation dosimetry calculations, the half-life included in the equations is the effective half-life. The effective half-life is defined as the period of time required for half of the unstable nuclei present to decay on average [74]. This half-life considers the disappearance of radioactivity from the body by two pathways: radioactive decay and biological clearance, this latter depending mainly on the patient's hepatic and renal function. These pathways are considered in the physical half-life of the radionuclide $T_{1/2,\mathrm{phys}}$ and biological half-life of the radiopharmaceutical $T_{1/2,\mathrm{biolog}}$, respectively, and are therefore incorporated in the effective half-life definition, as shown in Equation 2.5. It should be noted that although the physical half-life is known, the biological one may vary considerably, depending on the pharmacokinetics of the radiopharmaceutical and the presence of abnormal pathology [74]. The effective half-life range of commercially available radiopharmaceuticals varies from seconds to hours and should be similar in duration to the examination [74].

$$\frac{1}{T_{1/2}} = \frac{1}{T_{1/2,\mathrm{phys}}} + \frac{1}{T_{1/2,\mathrm{biolog}}} \tag{2.5}$$

Radioactive decay is divided into three categories: beta, gamma, and alpha. Considering the decay scheme of the radionuclide of interest in this study, ^{68}Ga, which will be analyzed in Chapter 2.2.3, special attention will be given to the beta-plus and gamma decay.

Beta decay is a type of nuclear decay in which an unstable nucleus transforms and ejects given particles to become more stable. Beta decay half-lives are quite variable and can be in the order of seconds or even thousands of years [75]. There are two types of beta decay: beta-minus and beta-plus. As previously stated, only the beta-plus will be studied in detail.

An unstable nucleus can undergo decay by positron (β^+) emission or electron capture to convert the excess of protons into neutrons. In the first process, a proton is converted into a neutron and a positron; the latter can also be referred to as a positive beta particle. In addition, a neutrino is emitted. On the other hand, in electron capture, a nucleus absorbs one of its inner orbital electrons (e^-), which combines with a proton, forming a neutron and a neutrino.

Beta particles have a continuous range of energies, and due to their small mass, they are more penetrating than alpha particles (i.e., helium nucleus consisting of two protons and two neutrons) but less than gamma radiation [63].

Gamma rays are electromagnetic radiation emitted from an excited nucleus after a spontaneous nuclear decay, usually an alpha or beta decay (i.e., after a beta-plus emission from ^{68}Ga). The process is as follows: after the emission of a particle in radioactive decay, the nucleus is left in an excited state. This excess energy is carried off as a gamma ray to conserve energy and leave the nucleus in a lower energy state. This emission is characteristic, and it is determined by the difference in energy between the initial and final transition levels within the nucleus. The number of protons and neutrons in the nucleus does not alter in this type of decay, therefore undergoing gamma decay does not change the structure or composition of the atom. Typical half-lives for gamma emission are very short, usually from 10^{-9} to 10^{-14} seconds [75].

2.2.2 Positron annihilation

Positrons are not stable particles in matter, and while slowing down by transferring their energy through ionizing and excitation events in the medium, they can eventually be stopped within 10^{-11} seconds [76]. Positrons combine with electrons by annihilation, originating two opposing directed gamma rays with an energy of 511 keV each (Figure 2.4). These photons, which result from the combination of the electron and positron masses, are crucial in PET imaging.

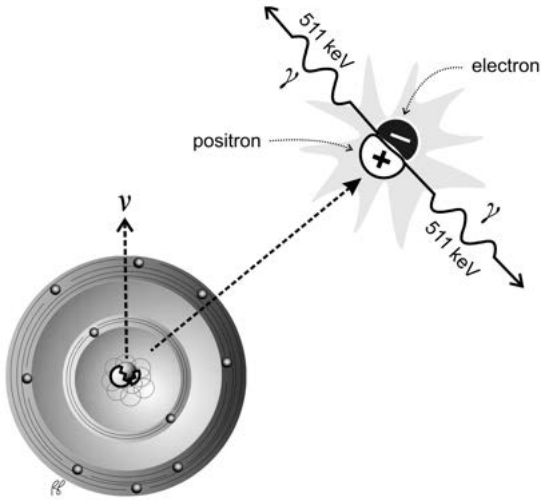

Figure 2.4: Illustration of the annihilation reaction. As a consequence of the beta-plus decay, a neutrino (**ν**) and a positron are emitted. This positron, when decelerating, combines with its antimatter: the electron. The combined mass is converted to energy in the form of two oppositely directed 511-keV gamma photons (**γ**) [77].

2.2.3 ^{68}Ga-PSMA-11

During the last decade, the employment of ^{68}Ga in NM has considerably increased since it is frequently used for effective and efficient diagnostics and personalized medicine.

This metallic radionuclide is produced from a $^{68}Ge/^{68}Ga$ generator system (Figure 2.5). Briefly, the equipment consists of a heavily shielded column constituted by a matrix (tin oxide matrix in most scientific institutions), on which the parent nuclide ^{68}Ge is absorbed [78]. The daughter nuclide ^{68}Ga is then eluted from the column with hydrochloric acid into a vacuum vial [78]. The availability, reliability, and purification steps of commercial generator systems allow the production of PET radionuclides at any time on demand without requiring a cyclotron on site. Also, and due to the long physical half-life of the parent radionuclide, ^{68}Ge, of about 270.8 days [79], the generator can be used for up to one year, providing cost-effectiveness and convenience to the user. The ^{68}Ga used to obtain the images present in this study was produced in the $^{68}Ge/^{68}Ga$ generator system available in the Nuclear Medicine-Radiopharmacology Department at the Champalimaud Foundation.

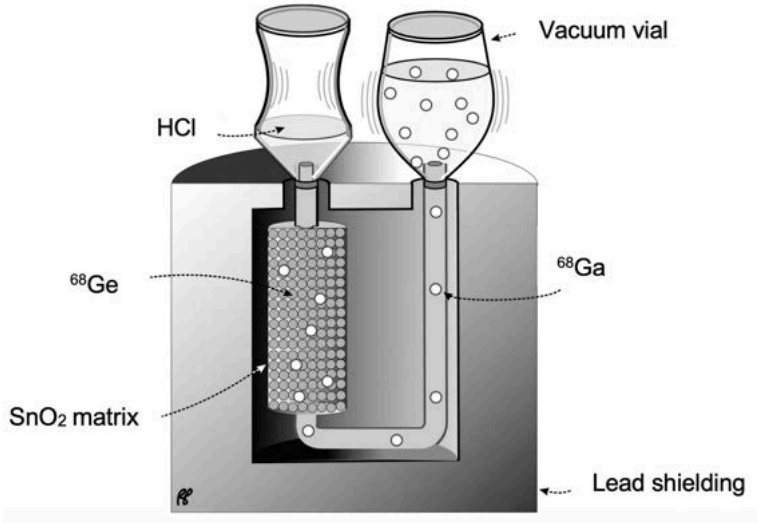

Figure 2.5: Illustration of a heavily shielded $^{68}Ge/^{68}Ga$ generator system. The ^{68}Ge is bound to the SnO_2 matrix present in the column. The ^{68}Ga is eluted by drawing HCl through the column into the vacuum vial. Adapted from [77].

^{68}Ga is not a pure positron emitter since it disintegrates 88.9% by positron emission (β^+) and 11.1% by electron capture into ^{68}Zn [78]. As represented in Figure 2.6, the main β^+ decay (87.68%) is a pure positron emission directly to the ground (stable) level of ^{68}Zn, with a maximum energy of 1.899 MeV [80]. A small fraction (1.2%) decays into an excited level of ^{68}Zn, which decays to the ground level with the emission of a gamma photon of 1.077 MeV. This photon can be scattered in the patient and generate a lower energy gamma photon that possibly (and incorrectly) coincides with an annihilation photon (of 511 keV), leading to errors in the PET image. On the other hand, in the electron capture component, 8.94% of the decay is directly to the ground level and 1.8% to the first excited level. The remaining (0.4%) decays are into short-life excited levels that emit gamma photons of various energies, ranging from 0.227 MeV to 2.821 MeV [81],

with negligible probability to be detected in coincidence. It is also important to highlight the emission of characteristic x-rays and Auger electrons as a consequence of the decay by electron capture, a process already described in detail above. The energy released in this radioactive decay is equal to 2921.5 (18) keV [81].

Even though ^{68}Ga has a relatively high positron energy, which can potentially lead to a lower resolution, the high fraction of positron emission is a significant advantage. Another advantage lies in its relatively short physical half-life of 67.77 (14) minutes, which results in improved dosimetry, repeat imaging, and short duration exams [81].

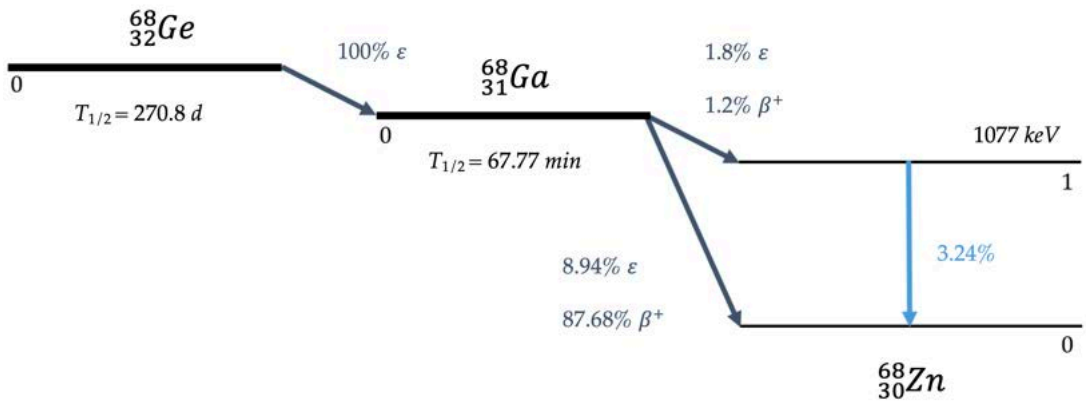

Figure 2.6: Decay scheme of ^{68}Ge and ^{68}Ga. ^{68}Ga decays 88.9% by positron emission ($\boldsymbol{\beta^+}$) and 11.1% by electron capture (**ε**), producing ^{68}Zn. Besides the emission of a 1.077 MeV gamma ray during the decay to the ground level of ^{68}Zn, there are other weak gamma transitions.

^{68}Ga-labeled imaging agents used in NM have been recognized as a new class of radiopharmaceuticals. As the relatively short half-life of ^{68}Ga is not compatible with ligands of slow pharmacokinetics, such as antibodies and glycoproteins, ^{68}Ga-based peptides constitute a powerful tool in clinical imaging studies [80]. These are valuable in diagnosis, including visualization, staging, and detection of relapse, and in planning potential molecular radiotherapy procedures.

In this study, the radiopharmaceutical employed is the Glu-NH-CO-NH-Lys-(Ahx)-[^{68}Ga-(HBED-CC)], also known as ^{68}Ga-PSMA-HBED-CC or ^{68}Ga-PSMA-11. This is a urea-based PSMA-target radioligand inhibitor that has evolved as a promising radiopharmaceutical for imaging PSMA expression in vivo since its introduction in 2012 by Eder et al [24].

PSMA is a type II transmembrane glycoprotein encoded by the Folate Hydrolase 1 (FOLH1) gene that was first detected on the human prostate cancer cell line Lymph Node

Carcinoma of the Prostate (LNCaP) [82]. This 750-amino acid surface marker with a molecular weight of 100 kD is relevant in prostate carcinogenesis and disease progression, glutamatergic neurotransmission, and folate absorption [83]. Because of its different roles, it has several names, the most common being glutamate carboxypeptidase II [84]. This folate hydrolase protein is overexpressed in 90-100% of prostate cancer cells and in other PSMA-expressing tissues such as kidneys, proximal small intestine, and salivary gland [85]. It is also expressed in tumor-associated angiogenesis as increased PSMA expression is found on the stroma adjacent to neovasculature of solid tumors and in other tumors such as glioblastoma, thyroid cancer, gastric, breast, renal, and colorectal cancer [86]. PSMA uptake has also been reported in many benign lesions such as retroperitoneal schwannoma, desmoid tumor, Paget's disease of bone, sarcoidosis, sub-acute stroke, and bone fractures [86]. The degree of PSMA expression increases according to the stage and grade of the tumor and biochemical recurrence, allowing PSMA-imaging to account for prognosis. The dual nature of PSMA to act as a receptor protein and as an enzyme triggered the synthesis of PSMA-inhibitors of low molecular weight to be employed as nuclear imaging probes.

PSMA labeling with ^{68}Ga is often performed with modular synthesis units in hot cells or shielded workspaces [87]. HBED-CC (*N,N'* -bis[2-hydroxybenzyl] ethylenediamine-*N,N'*-diacetic acid) is the chelator that binds to the purified ^{68}Ga on one end, forming a thermodynamically stable complex even at room temperature and with the target PSMA agent on the other to ensure concentration in the tissue of interest [83]. Once the ligand binds to the PSMA extracellular domain, it inhibits its enzymatic functions and is internalized into the cell by endocytosis [87]. The high accumulation of this radiopharmaceutical, even in small metastases, allows the detection of early metastatic lesions and the performance of staging, planning, and monitoring of therapeutic responses as well as evaluation of recurrence.

This molecular probe targeting PSMA is an excellent agent for target imaging. It provides high diagnostic specificity and sensibility, high tumor-to-background ratios, and a favorable biodistribution with fast target localization and fast clearance from the body.

2.2.4 Coincidence detection

PET systems employ PET radiotracers, also known as radiopharmaceuticals, which incorporate a positron emitter into biologically active compounds. These biological complexes are administered to the patient by either injection or inhalation. Diagnostic information is derived from observing the distribution of the biological molecule, while the radionuclide enables the localization of the radiopharmaceutical and the assessment of the amount of radioactivity present.

As already mentioned in this manuscript, the positron emitted by the radionuclide decay subsequently annihilates with an electron in the medium after traveling a short distance. As mentioned in Chapter 2.2.2, two gamma photons with 511 keV, departing approximately 180º apart, are produced (Figure 2.7-A). The two coincident photons will be emitted from anywhere within the scanner FOV. Coincident detection of these annihilation photons is the basic principle for acquiring PET images.

The TOF PET reconstructs the position of the annihilation events by measuring the time of arrival of each of the gamma photons at the opposing scintillation crystals within a resolving time. The time difference will be proportional to the difference in distances traveled by the two photons and can be used to calculate the position of the event along an imaginary line connecting the two detectors, called the line-of-response (LOR) (Figure 2.8-A). TOF resolution depends on the scintillator material, the photomultiplier tubes (PMTs), and the electronics [88]. A detailed description of PMT devices can be found in Chapter 2.2.5. Each time a detector pair acquires an annihilation event, the system assigns a count to the LOR (Figure 2.7-B). The storage of coincidences detected in a PET system can be done in two different formats: the list-mode format and the histogram format [77]. These data are then used for iterative computed image reconstruction, which uses tomographic mathematical algorithms to identify the location of the annihilation event with high accuracy and produce 3D images of the ROIs. Moreover, it is possible to determine the amount of radiopharmaceutical present in some specific region since the number of coincidences detected in the respective LOR, in the absence of effects such as Compton scattering or photon absorption, is proportional to the radioactivity of the PET marker throughout that LOR.

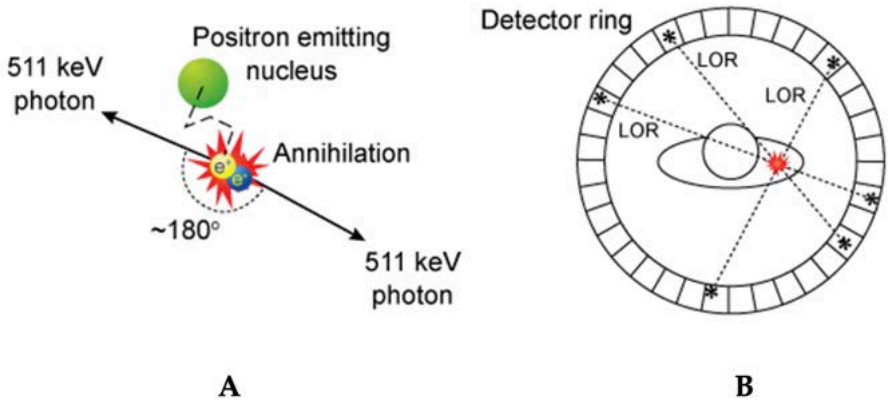

Figure 2.7: Illustration of the imaging principle of PET: A) After the annihilation of an electron-positron pair, two 511 keV gamma photons are emitted in opposite directions; B) When the two photons are simultaneously detected within a ring of detectors surrounding the patient, it is assumed that an annihilation event occurred on the so-called LOR connecting the two events (i.e., coincidence detection). The activity distribution can be tomographically reconstructed by recording many LORs. Adapted from [89].

The photons that provide correct information on the location of the decay (and electron-positron annihilation) are those that penetrate without interaction, the so-called primaries. However, artifacts that may appear in the images result from photon absorption, random coincidences, scatter coincidences, and multiple coincidences. The probability of any of these phenomena occurring is mainly governed by two parameters: the atomic composition and the tissue's total thickness along the photon trajectory. These interactions compromise the ability to accurately reproduce the radiotracers' kinetics and spatial distribution in the human body. The latest PET scanners employ algorithms during image reconstruction for correcting for these events [77].

Photon attenuation is the loss of counts due to the absorption of photons by the patient before they arrive at the detector. Attenuation is the largest source of bias in PET due to the relatively high energy of the positron-annihilation photon and the use of coincidence detection [89]. This effect causes the appearance of non-uniformities in the images, mainly in annihilations that occur in the center, compared to those that occur in the periphery [77]. In current PET scanners, the attenuation is mostly arithmetically compensated using transmission attenuation data from a CT x-ray source. X-ray photon energies are generally less than 140-keV, thus lower than the 511-keV annihilation photons [90]. Therefore, the linear attenuation coefficients measured with the x-ray must be scaled to the correct values before being used to correct the emission data for photon attenuation.

Single events are registered when an unpaired photon from a non-annihilation gamma ray, or only one of the pair of annihilation photons, impacts the detector. The annihilation will not be registered as a coincident event and will not be counted.

Scattered coincidence (Figure 2.8-B) occurs when one or both of the annihilation photons undergoes Compton scattering within the imaging FOV before reaching the PET detector, losing energy and changing direction. It is assigned a mispositioned LOR, which leads to misinterpretations in identifying the annihilation point. It is important to recognize that, as the density of tissue is approximately the same as that of water, it is assumed that the mean free path of a 511 keV photon is about 7 cm in human tissue [63]. Since the cross-section of the human body is much greater than 7 cm, the probability that many of the photons originated inside the human body are Compton scattered before they reach the detectors is high [63]. Also, as gamma photons' scattering probability depends on the path they have to traverse inside the body before interacting with the detectors, this effect is higher on abdominal images than on brain images. Scatter causes a falsely increased count rate, so it is desirable to remove such counts.

Random events (Figure 2.8-C) occur when two 511 keV uncorrelated gamma photons from two separate annihilation events interact with two opposing detectors within the system resolving time, and thus, are considered to have come from the same annihilation event. The other

two are lost. The probability of random events increases with increasing activity within the FOV and decreases as the resolving time decreases [77]. That's why most PET systems employ scintillators with faster response times.

Multiple coincidence (Figure 2.8-D) occurs when more than two photons are simultaneously detected. This event is disregarded as it does not allow the formation of a single LOR [91].

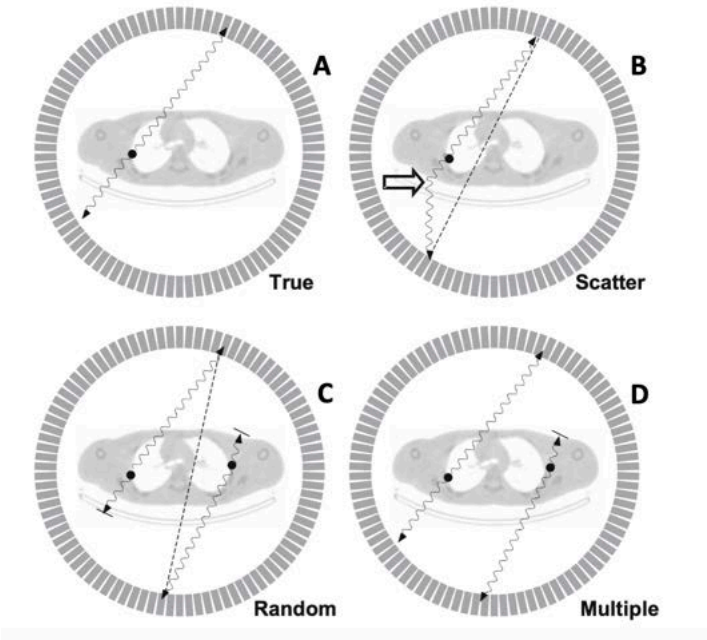

Figure 2.8: Scheme of events that may occur during PET acquisition for a complete ring of detectors. The black dots indicate the positron's annihilation position, while the dashed line corresponds to the LOR. As indicated, (A) true, (B) scatter, (C) random e (D) multiple events are illustrated. Adapted from [92].

2.2.5 Instrumentation

Current PET scanners are constituted by multiple rings of individual fast scintillator detector modules that axially surround the patient. Each block detector (Figure 2.9-A) of a PET equipment is characterized by small inorganic scintillator crystal arrays coupled to photodetectors [77]. Scintillator detectors are the most common and successful mode for detecting 511 keV photons in PET imaging due to their high stopping efficiency, sensitivity, and energy resolution [63]. Lutetium oxyorthosilicate (LSO) and bismuth germanate (BGO) are the most used scintillation crystals in PET scanners. These crystals have high densities and atomic numbers, which increase the probability of photoelectric and Compton interactions, respectively. However, the number of PET scanners with LSO crystals has been increasing because these crystals are associated with a higher light yield and a shorter decay time [63]. Consequently, the scintillation events necessary for image formation are obtained faster, and the patient's exposure time is reduced. The photodetectors used to convert the light photons into an electric signal can be divided into two categories:

semiconductor-based photodiodes and PMTs [63]. Although photodiodes possess high sensitivity for detecting low energy scintillation photons, PMTs are the most reliable technique since they lead to a very good signal-to-noise ratio (SNR) even for low light levels [63]. The photomultiplier (Figure 2.9-B) consists of a photosensitive cathode, several dynodes, and a collection anode [77]. In a more-in depth manner, the annihilation photons, by exciting the detectors' crystals, produce visible (scintillation) light photons. This scintillation stimulates the ionization of the photocathode, which emits electrons that are multiplied and accelerated (usually by a factor of 10^7) [93]. Then, at the anode, electrical pulses are generated. These outputs are amplified by preamplifiers and amplifiers and subsequently are converted into three signals, two of which give the spatial location of the scintillation, while the third represents the energy deposited in the crystal by the gamma ray. The pulse height analyzer processes the size of the third signal to determine if the energy of the photon reaching the crystal is within the range of values expected for the particular radionuclide, and the coincidence circuit determines if the signals occurred within the coincidence time window [88]. The resolving time of PET systems depends on the decay time of the selected crystal material, which is equal to 300 ns on BGO crystals and 40 ns in LSO crystals [63]. Conventionally, each detector module comprises 169 crystals for 4 PMTs and is connected to a single electrical circuit that explores the scintillation light distribution of the four PMTs to determine the interaction position and the detection time interval [77].

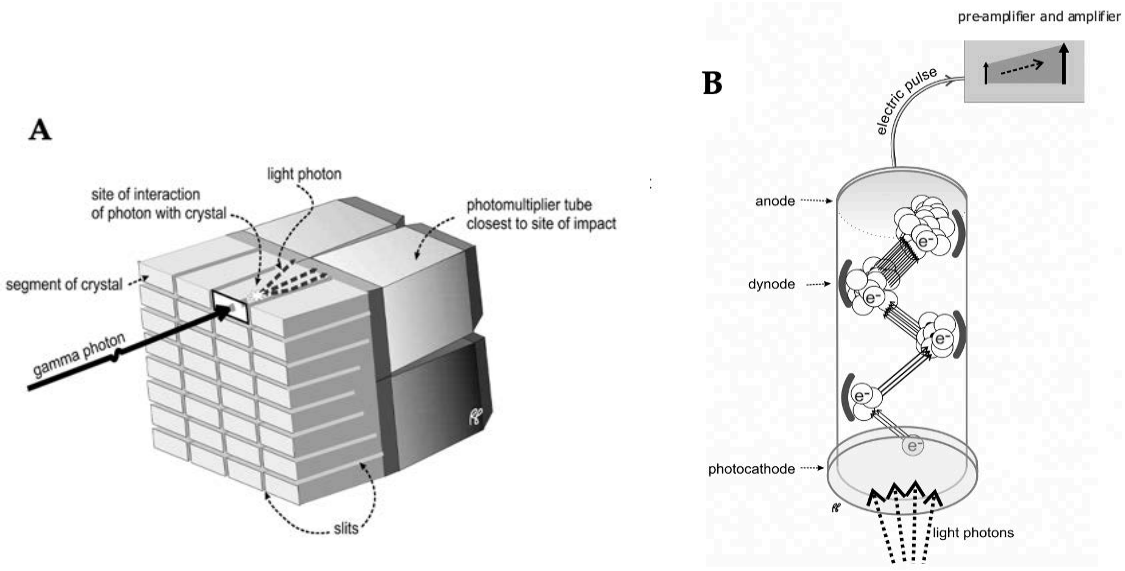

Figure 2.9: Illustration of a block detector and a photomultiplier tube and its preamplifier and amplifier: A) Each detector module is usually composed of several crystals' segments, coupled to four PMTs. The crystals act as transducers, converting the gamma photons into light photons. The PMTs then convert the scintillation light into electrical signals. The location of the site of impact is achieved by measuring the light detected in each PMT, which is stronger if it is closer to the site. Slits between crystals divisions direct the light photons towards the PMTs. B) The light photons that reach the photocathode cause it to emit electrons. These electrons cascade along the multiplier portion of the tube, successively striking each of the tube's dynodes. The electric pulses generated at the anode are later amplified by preamplifiers and amplifiers. Adapted from [77].

The spatial resolution of a PET scanner is defined as the minimum distance at which two radioactive sources can be placed so they can be individually distinguishable in the image [89]. The current technology using block detectors with crystals coupled to the PMTs achieves a spatial resolution of about 3 to 4 mm [94]. The higher the number of detectors per ring and the number of PMTs, the better the spatial resolution of the system [77]. On the other hand, the intrinsic spatial resolution of PET is dependent on the scintillation crystal dimensions, and small-sized crystals optimize the intrinsic resolution [88]. However, one of the factors that affects spatial resolution is the short distance that the positron travels before annihilating, resulting in an uncertainty of the nuclear decay localization. In the particular case of the positron emitted by ^{68}Ga, its range in matter is quite large and can vary between 2.9 mm and 10 mm [95]. Another effect that limits the spatial resolution of PET is due to the angular deviation (±0.25º at maximum) of the photons with respect to 180º [92]. This effect increases with the diameter of the detector ring [96]. Thus, by assuming that the photons are emitted simultaneously, in opposite 180º directions, the detectors miscalculate the localization of the positron emission.

2.3 ^{68}Ga-PSMA-11 PET/CT

^{68}Ga-PSMA-11 PET/CT imaging is revolutionizing cancer management since its development in 2013 [87]. This imaging modality is being incorporated into the routine clinical management of patients and has become a standard of care in the diagnosis, selective staging, and monitoring of therapeutic response of prostate cancer. Even though ^{68}Ga's positrons have a high range in tissue, the spatial resolution and diagnostic sensitivity of the state-of-the-art PET/CT are high compared to other techniques [96]. As seen, although the main focus in clinics is prostate cancer imaging, this radiopharmaceutical can be used to obtain images from other parts of the body where PSMA is expressed. In this work, the incorporation of ^{68}Ga-PSMA-11 in the dual PET/CT system was to obtain images of potential metastases in the patient's body and quantify the absorbed dose in the organs with higher uptake of this radiopharmaceutical.

2.4 Instrumentation

Commercially available whole-body fully integrated PET/CT equipment consists of a patient support system, a workstation to perform the reconstruction and visualization of the data, and a gantry where the PET and the helical CT are located separately. This type of scanner enables the patients to perform both diagnostics without their dislocation and accurately associate areas of high metabolism with their anatomical location in one examination.

As the CT scanner is placed closer to the patient, the CT image is acquired in its entirety before acquiring the PET scan (Figure 2.10). This CT image will later be used to correct gamma photon attenuation. After the patient passes through the two components, both anatomical and functional images are acquired at the same spatial referential and are co-registered to create a single fused image. This is performed on a workstation responsible for image acquisition and reconstruction that applies mathematical algorithms to analyze and view the images in three different planes: transverse, sagittal, and coronal.

Two configurations of PET/CT scanners are used nowadays. Analog PET/CT is the most used equipment type, and it uses conventional PMTs coupled with crystal scintillators [20]. On the other hand, digital PET/CT employs an array of innovative scintillation detectors called silicon PMTs. The PET/CT equipment used in this project is the Philips Vereos Digital PET/CT system. This system offers better image quality, diagnostic confidence, and accuracy than analog PET/CT. Also, its better TOF resolution improves spatial resolution [4].

PET/CT scanners hold a single patient bed, which allows the patient's consistent positioning between acquisitions and reduces the risk of misregistration of the images. The patient handling system between the two rings of detectors was developed to adapt to the patient's position in each system separately [65]. The advantages of building a PET/CT system include better cost-effectiveness of the procedures and a more comprehensive clinical report. Furthermore, it is not necessary to move the patient to perform both scanners.

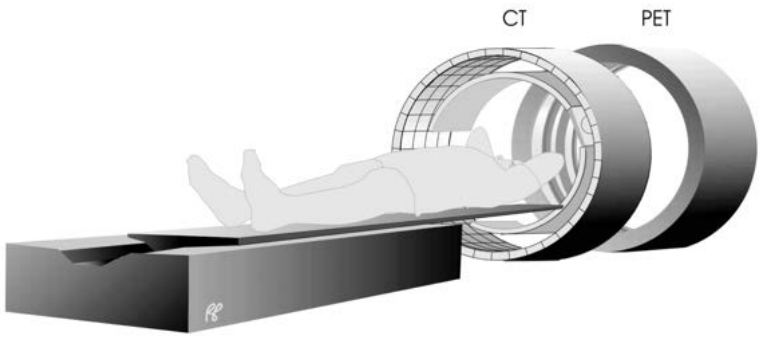

Figure 2.10: Scheme of the PET/CT scanner. The entire CT is acquired first, followed by the PET scan. The images are co-registered to create a single image with both anatomical and functional information of the human body [65].

3

Internal Dosimetry

The purpose of internal dosimetry, also known as dosimetry in NM, is to estimate the absorbed dose of ionizing radiation due to the administration of diagnostic or therapeutic radiopharmaceuticals in the human body.

Ionizing radiation is characterized by having a wavelength equal to or less than 10 nm or a frequency equal to or greater than 3 x 10^{15} Hz [97]. In most cases, energy deposition by ionizing radiation is a stochastic phenomenon. Therefore, at very low doses, an amount of energy sufficient to lead to cell mutation or death may be deposited in a target. Different types of radiation cause different amounts of damage even for the same quantity of energy deposited, with photons causing the least and heavy charged particles the most. Photons possess high penetration power and thus have few interactions with matter, which results in low energy absorption and a low absorbed dose to the tissues. On the other hand, heavy charged particles have a higher number of interactions with tissue in a short distance, resulting in increased energy absorption. Consequently, the absorbed dose and tissue damage are higher.

The paramount goal for the good use of the imaging techniques is to understand the level of toxicity from radionuclide administration and, thereby, deliver the most efficient diagnosis with a minimal level of adverse effects for the patient. Absorbed dose is the relevant quantity for evaluating the biologic effects of ionizing radiation emitted by administered radiopharmaceuticals [98]. The standardization of the absorbed dose estimates for diagnostic purposes ultimately increases success in identifying correlations between calculated absorbed dose and the clinically observed effects, which must be established separately for each radiopharmaceutical and each patient subgroup. Since the absorbed doses in tissues are low for diagnostic NM procedures, the resulting stochastic risk of hereditary carcinogenic disease is correspondingly low or absent.

Nevertheless, further information is required to establish an accurate correlation between absorbed dose and toxicity, such as energy and particle type, linear energy transfer, and, more specifically, track structure [65].

There has been a growing interest in small-scale dosimetry at the voxel level, as well as in patient-specific dosimetry. In this project, internal dosimetry was conducted using the latest dosimetry MIRD schema [99] at the voxel level. The voxel S-values approach enables fast and accurate conduction of dosimetry calculations, in addition to the risk-benefit assessment of radiopharmaceuticals in clinical applications. Patient-specific radiopharmaceutical dosimetry requires two sets of information: patient-specific biokinetic data for the radiopharmaceutical of interest, obtained by administering a tracer dose to the patient and by using imaging techniques to develop an individual biokinetic model, and a 3D voxel phantom to perform simulations of radiation transport in anthropomorphic models to derive S-factors, employing the usual Monte Carlo approach.

3.1 Absorbed dose

Absorbed dose is the energy absorbed from ionizing radiation per unit mass of the tissue and is applicable to indirectly and directly ionizing radiations [98]. Indirectly ionizing radiation (typically photons) transfers its energy to secondary charged particles (electrons) that, consequently, transfer some of their kinetic energy to the tissues. On the other hand, if directly ionizing radiation (corpuscular radiation, typically electrons and beta particles) interacts with a material, ionization and excitation phenomena occur, and energy is deposited within that material. These two forms of energy deposition result in absorbed dose in tissues.

Absorbed dose is a non-stochastic quantity defined by the International Commission on Radiation Units and Measurements (ICRU) Report 51 [100] as:

$$D = \frac{d\bar{\varepsilon}}{dm} \tag{3.1}$$

where $d\bar{\varepsilon}$ is the mean energy imparted by ionizing radiation to the matter of mass dm. The stochastic quantity imparted energy is the sum of all energy entering a volume of interest minus all the energy leaving the volume, taking into account any mass-energy conversion within the volume [98]. The absorbed dose unit is joule per kilogram (J/kg), also known as gray (Gy). In NM, the most common unit of absorbed dose is the miligray (mGy), which corresponds to 10^{-3} Gy.

In NM, absorbed doses are usually calculated to single target organs. The individual organ absorbed doses can range over several orders of magnitude, depending on the administered radiopharmaceutical's biokinetics.

3.2 Biological effects of radiation

Biological systems are extremely sensitive to radiation, and the main target is the deoxyribonucleic acid (DNA) chain. Ionizing radiation causes damage to tissues through ionization, either directly with the cell or indirectly with water, leading to free radicals [97]. Once damaged, the DNA will repair correctly or incorrectly or be so damaged that it will become non-functioning or die. Incorrect repair causes cancer and heritable genetic mutations, known as stochastic effects, whereas cell death leads to deterministic effects such as skin injuries and cataract formation [101].

Deterministic effects result from exposure to ionizing radiation, which, when in sufficient dose, causes cell damage or cell death, impairing the function of the irradiated organ or tissue. There is a threshold radiation dose below which deterministic effects are not seen, and as the absorbed dose value increases past this threshold value, the number of cells that die, and so the severity of the effect, increases [97]. Absorbed dose addresses deterministic effects [102].

Stochastic effects involve the non-lethal modification of the exposed individual's cell genetic material and have no threshold value. They are characterized by a probabilistic nature; that is, the probability for the effect to occur depends on the dose of ionizing radiation. This modification is conventionally considered to be DNA mutations in the cell nucleus when it is not properly repaired, which can lead to cancer in the individual if it occurs in a somatic cell. If it is in a germ cell, hereditary genetic abnormalities are another possible stochastic effect. As absorbed dose increases, the risk of observing these effects increases. However, the severity of the stochastic effect is not related to the absorbed dose [97]. The dosimetric quantities equivalent dose and effective dose are used in comparative evaluations of potential risks of radiation-induced stochastic effects to patients after NM procedures [97]. Equivalent dose is a dose quantity calculated for individual organs, adjusted to account for the effectiveness of the type of radiation. In contrast, effective dose considers the varying sensitivity of different organs and tissues to radiation [103]. Nevertheless, further analysis of these quantities is beyond the scope of this study.

While unjustified and unnecessary exposures lead to risks due to stochastic effects, unintended exposure of patients, which can arise from unsafe design or use of medical technology, can lead to deterministic effects [104]. The potential damage to health due to exposure to ionizing radiation causes a reduction in life expectancy and quality of life. The biological effects of radiation are influenced by many factors, including the amount and rate of energy imparted to the tissue, the type of radiation emitted by the radionuclide, the cell and tissue type involved, and the age, gender, and sensitivity to radiation of each individual.

3.3 Voxel-based dosimetry

The assessment of the absorbed dose at the voxel level, that is, at each voxel constituting an organ or tissue with dimensions ranging from hundreds of micrometers to a few centimeters [105], is becoming increasingly important when performing dosimetry in NM.

The voxel approach considers the possible non-uniform activity distribution of the internally deposited radiopharmaceutical within the target organs, assuming that the distribution within each voxel is uniform. This constitutes an improvement over conventional organ-based dosimetry estimates. It enables a more accurate dosimetry performance, and it is extremely helpful in personalized medicine. Three computational methods are available to perform dosimetry at the voxel level: convolution with a Dose-Point Kernel (DPK), Monte Carlo simulations, and the voxel S-value approach based on the MIRD schema. Since the latter techniques are the ones used in this study, a special focus will be given in the following section (Chapter 3.3.1 and 3.3.2).

The DPK method is an analytical convolution technique that describes the radial energy deposition around an isotropic point, characterized by being the site of emission of the radiation [106]. It involves the convolution of a dose point kernel and the activity distribution to consider the contributions from the surrounding point sources to the target voxel [107]. Since it is an analytical tool, it is computationally fast and is the most widely used voxel-based dosimetry approach. However, it does not consider the heterogeneity of the medium [106].

3.3.1 MIRD S-values approach

According to the MIRD approach at the voxel level, the estimation of the absorbed dose is dependent upon two types of information: time-dependent or biokinetic factors, incorporated in the physical quantity cumulated activity, and time-independent or physical factors, incorporated in the S-values definition.

The cumulated activity $\tilde{A}_{\mathrm{h}}$ is equal to the number of decays that take place in a certain source voxel of a 3D activity distribution during the relevant time period [108]. The MIRD schema uses this term to represent the integral of activity over time, expressed as follows:

$$\tilde{A}_{\mathrm{h}} = \int A(t)dt \tag{3.2}$$

The time-integration period is commonly chosen from the time of administration of the radiopharmaceutical until infinite time for long lived isotopes or until at least 10 times the isotope half-life for short-lived isotopes [99]. However, for a more accurate calculation, the integration period should be matched to the biological endpoint studied in combination with the time period in which the relevant absorbed dose is delivered [102]. Since the integral of any continuous curve

is equal to the area under the curve, the cumulated activity can be obtained directly by physically measuring the area under the time-activity curve that plots the effective disappearance of activity in each tissue or organ.

A voxel S-value is defined as the mean absorbed dose to a target voxel per radioactive disintegration (i.e., absorbed dose rate per cumulated activity) in a source voxel (Figure 3.1) [109]. This quantity depends on the type and energy of the radiations emitted, size, shape, and distance between the target voxel and the source voxel, and on the medium's composition. In this approach, it is assumed that both the target and source voxels are contained in an infinite homogeneous tissue medium [102]. Since the S-values depend on the type of radionuclide, voxel size, and medium, it is necessary to recognize the decay scheme of the radionuclide in question, so all the radiations of interest and the electron and photon absorbed fractions, which are calculated according to the voxel size of interest, are considered. Equation 3.3 demonstrates how the absorbed dose to the target voxel k per disintegration in the source voxel h can be calculated. This definition includes a summation over all the transitions i per decay:

$$S_{\mathrm{k}\leftarrow\mathrm{h}} = \frac{\sum_i n_{\mathrm{i}} E_{\mathrm{i}} \varphi_{\mathrm{i}}(v_{\mathrm{k}} \leftarrow v_{\mathrm{h}})}{m_{\mathrm{k}}} \tag{3.3}$$

where n_{i} is the number of nuclear transitions per nuclear transformation, E_{i} is the mean emitted energy per disintegration, $\varphi_{\mathrm{i}}(v_{\mathrm{k}} \leftarrow v_{\mathrm{h}})$ is the absorbed fraction of the energy emitted from the source voxel h that is absorbed in the target voxel k and m_{k} is the mass of the target voxel. The SI unit of the S-value is Gy/(Bq·s).

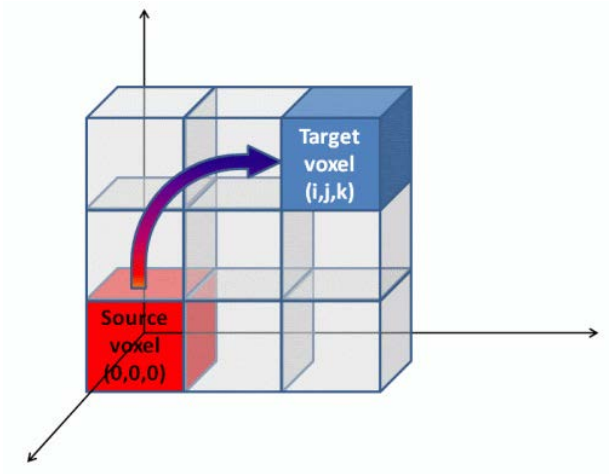

Figure 3.1: Illustration of a source voxel and a target voxel. S-values are scored in grids of uniformly dispersed cubic voxels (target voxels), with the source voxel irradiating the surrounding ones isotropically. The centroid of the source voxel was assumed as the origin of the Cartesian system [110].

For a more concise nomenclature, the MIRD schema also includes the specific absorbed fraction concept, which is defined as the absorbed fraction per unit mass of the target voxel. The

specific absorbed fraction for a target being irradiated by a source is the ratio of the absorbed fraction to the target voxel mass: $\Phi_{\mathrm{i}}(v_{\mathrm{k}} \leftarrow v_{\mathrm{h}}) = {\varphi_{\mathrm{i}}(v_{\mathrm{k}} \leftarrow v_{\mathrm{h}})}/{m_{\mathrm{k}}}$. The quantities E_{i} and n_{i} are usually expressed as: $n_{\mathrm{i}}E_{\mathrm{i}} = \Delta_{\mathrm{i}}$, which is the mean energy of the nuclear transition *i*.

Using these definitions, the final equation for the S-value is given by:

$$S_{\mathrm{k}\leftarrow\mathrm{h}} = \sum_i \Delta_{\mathrm{i}}\, \Phi_{\mathrm{i}}(v_{\mathrm{k}} \leftarrow v_{\mathrm{h}}) \tag{3.4}$$

The S-values are calculated from absorbed fractions using Monte Carlo techniques that employ voxel-based phantoms. These techniques describe the geometric and spatial effects of the dose distribution from the source to the target voxel.

The absorbed dose-rate is the amount of energy absorbed per unit time per unit mass of the material [111]. It varies depending on the activity and the S-values [112]. The activity varies with the 3D biodistribution of the radiopharmaceutical, the metabolism of the patient, and the radioactive decay of the radionuclide. Therefore, the activity in each organ varies with time. On the contrary, the time dependency of the S-values is neglected since the source and target masses remain constant throughout irradiation [102]. Considering that the amount of activity does not remain constant in the source voxel, the mean absorbed dose equals to the integral of the dose rate over the period of interest. Therefore, the mean absorbed dose in a given target voxel *k* includes the contribution not only of the *n* surrounding source voxels *h* but also of the target voxel *k* itself and can be calculated from the following equation:

$$\bar{D}_{\mathrm{k}} = \int \dot{D}_{\mathrm{k}}(t)\, dt = \int A_{\mathrm{h}}(t)\, S_{\mathrm{k}\leftarrow\mathrm{h}}\, dt = \sum_{h=0}^{n} \tilde{A}_{\mathrm{h}} \cdot S_{\mathrm{k}\leftarrow\mathrm{h}} \tag{3.5}$$

where $\tilde{A}_{\mathrm{h}}$ is the time-integrated activity in the *h*th-voxel during the time interval of interest and $S_{\mathrm{k}\leftarrow\mathrm{h}}$ is the S-value corresponding to a given combination of voxel target *k* and voxel source *h*.

The voxel S-value approach offers a convenient and simple method for voxel-based dosimetry calculations. It can be implemented without the need for time-consuming efforts, unlike Monte Carlo simulations, and has advantages over DPK in that there is no need to convert spherical coordinates to cartesian coordinates over the target volumes or perform intensive volume integrations [106]. However, the MIRD Pamphlet No. 17 [105] contains a limited number of radionuclides and voxel sizes. Since this approach requires knowledge of the S-values for each radionuclide used and for each specific voxel size, this constitutes a considerable limitation when using the S-values. Also, heterogeneities in the medium are not considered in this approach, and applicable cases are limited to lesions in homogeneous tissues such as liver cancer [106].

3.3.2 The MCNP6.1 dosimetry code

The stochastic Monte Carlo approach tracks particles generated by Monte Carlo engines and calculates deposited energies at the voxel level. Electron Gamma Shower (EGS), Monte Carlo N-Particle transport code (MCNP), Geant, and Penelope are commonly used Monte Carlo codes [113, 114]. This method is different from the other two voxel approaches already mentioned because it considers the inhomogeneities of the medium. Nevertheless, it requires extensive time and computational resources and is thus not the preferred technique in the clinical context.

MCNP6.1® is a general-purpose Monte Carlo radiation transport code. Los Alamos National Laboratory developed this versatile and straightforward code by merging the MCNP5® and MCNPX® codes [115]. MCNP6.1 uses the ICRU Report 44 [116] and the National Institute of Standards and Technology (NIST) database [116] to define the density and elemental composition of the materials requested by the user.

MCNP6.1 accounts for neutron, photon, electron, or coupled neutron/photon/electron transport within the energies involved in imaging techniques, resulting in a good option to perform dosimetry estimations for most radionuclides used in NM context [115]. In this study, only the photon and electron/positron transport processes were considered. For photons, the code accounts for, but not only, incoherent and coherent scattering, absorption in pair production with local emission of annihilation radiation, and bremsstrahlung [115]. On the other hand, electron/positron transport processes account for angular deflection through multiple Coulomb scattering and the production of secondary particles, including K x-rays, knock-on, Auger electrons, bremsstrahlung, and annihilation gamma-rays. A continuous-slowing-down model is used for electron transport that includes positrons, K x-rays, and bremsstrahlung radiation [115]. In MCNP6.1, a new single-event treatment coupled with the ENDF/B VI.8 database was developed for electron transport. This new method allows direct sampling of microscopic data distributions and, consequently, an accurate low-energy transport from 1 keV down to 10 eV [117].

Specific areas of application of this code include radiation protection and dosimetry, radiography, and medical physics [115]. For internal dosimetry purposes, the decay schemes of the radionuclides are selected from ICRP Publication 107 [118], and considering the cross-section data for the respective range of energies, the emitted particles are monitored. These particles suffer interactions and lose energy until they are finally completely absorbed or escape the material (phantom or patient). Their average behavior, which depends on the output chosen by the user, is then examined. The most frequently requested outputs are particle current, particle flux, and energy deposition. In this study, Salvatore di Maria (PhD Researcher at C2TN, IST, Universidade de Lisboa) [119] performed the voxel S-values calculations with the MCNP6.1 Monte Carlo code.

3.3.3 Dose-volume histogram

The mean absorbed dose in internal dosimetry may be a poor representation of the voxel-wise dose distribution in tissues due to the non-uniform activity distribution of the administered radiopharmaceuticals. Hence, DVHs have gained greater prominence in radionuclide dosimetry studies. These provide a mathematical framework for dose organ profile summarization and analysis on a per-patient basis [112].

DVHs describe the absorbed dose values in all voxels throughout the entire segmented ROI. No anatomically relevant location information is considered, as all voxels comprising a structure are considered to be of equal dosimetric and biological importance [112]. In a DVH, the *x*-axis corresponds to the level of the absorbed dose received by a voxel, and the *y*-axis corresponds to the volume (absolute in ml or cc, or relative in percentage) receiving a specific absorbed dose value [120]. There are two categories of histograms: differential DVH (dDVH) and cumulative DVH (cDVH). While the dDVH displays the volume (in the *y*-axis) of a structure that has received a specific absorbed dose (in the *x*-axis), the cDVH shows (in the *y*-axis) the percentage of volume that has received at least that value of absorbed dose (in the *x*-axis) [121].

Overall statistical information provided by the DVHs includes maximum dose, minimum dose, median dose, and mean dose. The cDVH is the most employed histogram when evaluation of key dosimetry issues are performed [121]. For instance, the mean dose is determined as the area under the cDVH normalized to the range [0,1] along the volume axis. Additionally, the median dose in the cDVH is the dose corresponding to the percentage of volume equal to 50%.

DVHs are extremely used to describe the non-uniformity of the voxel-wise absorbed dose distributions. A truly uniform absorbed dose distribution would produce a dDVH that shows a single sharp peak and a step function on a cumulative DVH. In the latter, and according to the theoretical concepts applied in dose distributions in external radiotherapy and brachytherapy, the greater the extent of the curve plateau, the smaller the difference between the minimum and maximum dose values, the greater the slope of the cDVH curve and the more uniform the uptake in the structure. On the other hand, if the plateau extent is close to zero, the minimum dose and the cDVH slope are also close to zero, which results in a highly non-uniform dose distribution in the organ, and the standard deviation (SD) is often higher than the mean.

4

Materials and Methods

4.1 Patient dataset

The dataset used in this study is composed of 6 male patients who underwent whole-body ^{68}Ga-PSMA-11 PET/CT between December 2015 and October 2020. The patients were referred for imaging for restaging of prostate cancer. Patients' characteristics are registered in table 4.1.

The exams were conducted at the NM Department of the Champalimaud Clinical Centre (CCC) in a Philips Vereos Digital PET/CT scanner. The data were collected after the patients' written informed consent and subsequently de-identified to ensure their confidentiality. During their first consultation, all patients signed an informed written consent form allowing the use of their data, specifically imaging data for research and educational purposes. This consent form was approved by the Ethics Committee of the CCC.

Table 4.1: Characteristics of the patients included in the dataset.

Characteristics	Patient 1	Patient 2	Patient 3	Patient 4	Patient 5	Patient 6
Age (years)	70	79	67	74	64	88
Height (cm)	165	167	172	177	178	168
Weight (kg)	86	76	62	88	84	82
Body mass index (kg/m^2)	31.6	27.3	21.0	28.1	26.5	29.1

4.2 Radiolabeling and purification of ^{68}Ga-PSMA-11

^{68}Ga was obtained from a Good Manufacturing Practice (GMP)-compliant ^{68}Ge/^{68}Ga generator from iThemba Labs in use at the NM Department of the CCC. Cationic ^{68}Ga (^{68}Ga (III)) was

eluted with 3.8 mL of 0.6 M HCl and with a b-SnO_2 inorganic separation resin matrix. It was then postprocessed with ethanol/HCl solution according to a method described in the literature [122, 123].

^{68}Ga-PSMA-11 was synthesized as previously published [24]. Radiochemical purity was tested by instant thin-layer chromatography (ITLC) (catalog ID SGI0001, Agilent Technologies) using 77.7 g/L of ammonium acetate in a 50:50 solution of H_2O and methanol as a mobile phase.

Labeling reactions were executed using the iQS® ^{68}Ga Fluid Labeling Module (ITG) and the ^{68}Ga Peptide Radiolabeling Kit (ITG, Germany) at 95ºC for five minutes as previously published [124]. Elution with ethanol was performed after purification of the radiopharmaceutical with 30-mg ^{18}C cartridges. The final product was dissolved in NaCl 0.9% with subsequent sterile filtration in a sterile flask.

4.3 Image acquisition and reconstruction

Each patient received on average 1.8 MBq/kg of ^{68}Ga-PSMA-11 intravenously while on the scanner, as recommended in the European Association of Nuclear Medicine (EANM) and the Society of Nuclear Medicine and Molecular Imaging (SNMMI) procedure guideline [125]. The administered activities to the six patients in MBq are summarized in table 4.2.

Table 4.2: Administered activities to the patients included in the dataset.

Administered activity	**Patient 1**	**Patient 2**	**Patient 3**	**Patient 4**	**Patient 5**	**Patient 6**
A_0 (MBq)	87.69	109.15	120.99	181.30	172.05	162.80

Thereafter, for patients 1, 2, and 3, two-time sets of whole-body PET/CT images were obtained in supine position, while for patients 4, 5, and 6, three-time sets were acquired under the same conditions. Considering the first subset of patients, the first image acquisition started approximately 60 ± 10 min post-injection, according to the EANM/SNMMI procedure guideline and current standard practice [125, 126], and the second scan started approximately 90 ± 15 min post-injection. The acquisition time was 25 min for the first scan and 10 min for the second. On the other hand, for the second subset of patients, the first acquisition started approximately 30 ± 10 min post-injection, whereas the second and third scan started approximately 60 ± 5 min post-injection and 90 ± 10 min post-injection, respectively. The acquisition time was 20 min for the first scan, 25 min for the second, and 10 min for the third. All patients voided after each scan, as recommended in the EANM/SNMMI procedure guideline [125].

As mentioned above, all image acquisitions were performed on a Philips Vereos PET/CT scanner. This system is TOF capable and has full 3D PET capabilities together with a CT for attenuation correction, image fusion, and anatomic correlation. For each bed position, an acquisition time of 70 seconds with a 16.4-cm FOV was applied. Emission data were corrected for decay, random events, attenuation, and scatter. As image reconstruction was applied with default clinical parameters, the scanner was not used at its maximum capability. Iterative image reconstruction was based on the ordered subsets expectation maximization (OSEM) algorithm with 3 iterations and 15 subsets to reconstruct 441 transaxial slices of 144×144 voxels with 4×4×4 mm^3. These transaxial images were reformatted into coronal and sagittal images to facilitate image interpretation.

4.4 Image processing

After reconstruction, all CT and PET images of each patient were de-identified, and the respective Digital Imaging and Communications in Medicine (DICOM) files were converted to the Neuroimaging Informatics Technology Initiative (NIfTI) format for simpler and more efficient processing. This conversion was performed, and the images were prepared for 3D visualization and further processing on the 3D Slicer 4.10.2 open-source software platform *(https://www.slicer.org)* [127], as shown in figure 4.1.

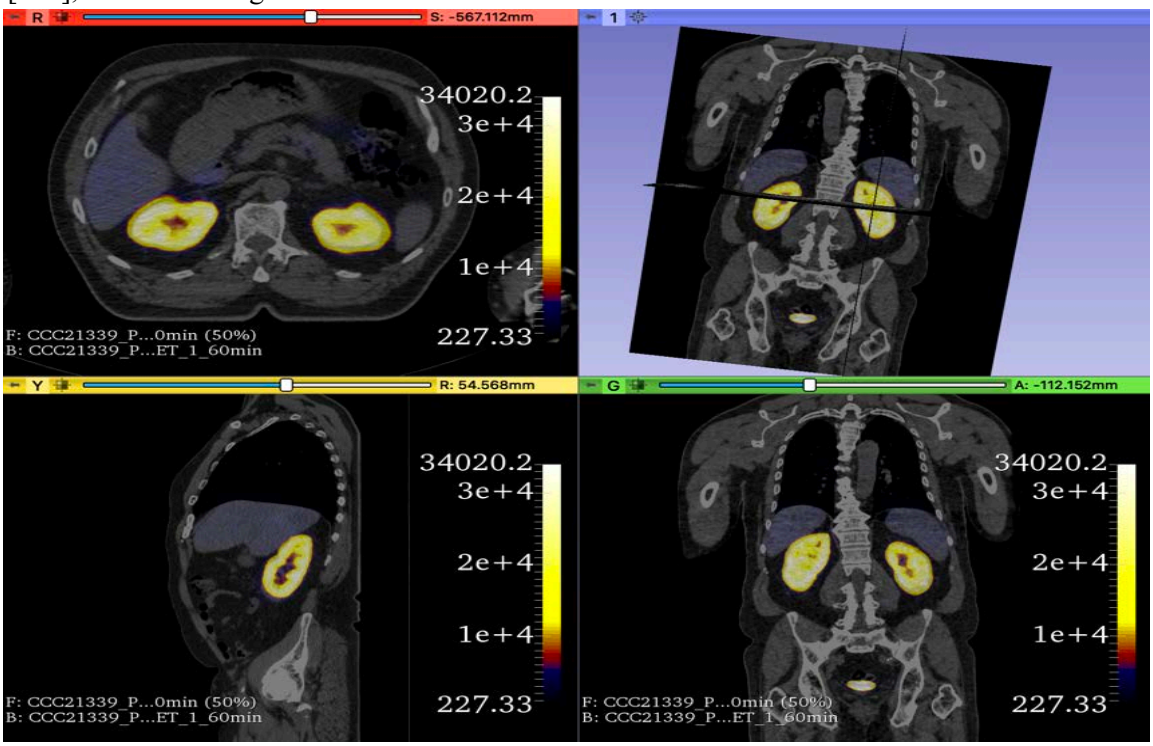

Figure 4.1: Representative axial (R), coronal (G), and sagittal (Y) orthogonal slices as well as the 3D view (1) of a patient's PET/CT image in the 3D Slicer software. The colormap shown is the 'PET-Rainbow' in the 3D Slicer. The color scale was adjusted to vary between black (areas with no intensity/tracer uptake) at 227.33 and white (areas with maximum intensity) at 34020.2.

4.4.1 Image co-registration

PET and CT images from the same session were hardware co-registered. However, misalignments between PET and CT images of different acquisitions were observed due to patient and bed motion.

Image registration was performed for all patient images using the 3D Slicer software. The aim was to align each evaluation PET/CT ("moving image" in Slicer) with the image coordinate system of the baseline PET/CT ("fixed image" in Slicer) from the first acquisition. Rigid transformations were performed since only rotations and translations were applied. Image registration was based on the CT images due to the exquisite anatomic details and image resolution. First, the evaluation CTs were registered to the baseline CT, with the help of landmarks and different color schemes. Then, the resulting transformation matrices were applied to transform the evaluation PETs to be baseline imaging PET/CT space (Figure 4.2).

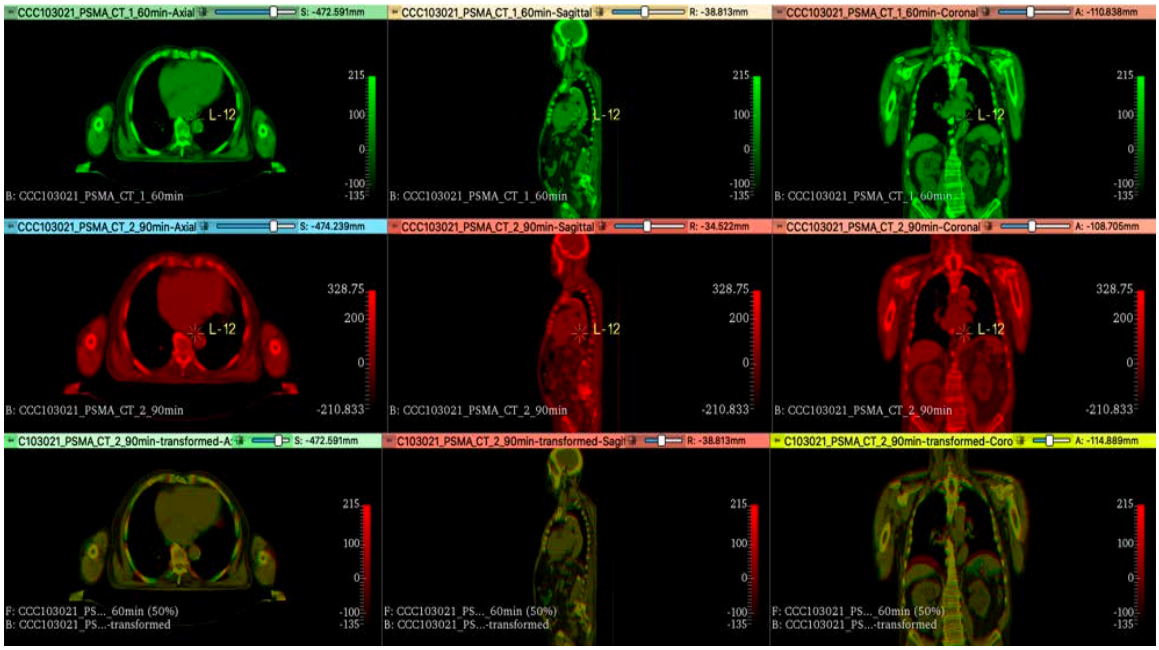

Figure 4.2: Landmark Registration in the 3D Slicer software. In this example, the fixed image corresponds to the first acquisition CT (green color), while the moving image corresponds to the second acquisition CT (red color). The colormap shown comes from the application of the color module 'Grey' in the 3D Slicer, followed by a green and red coloring to facilitate visualization of the final superimposed image. The visible landmark (L-12) in the two CT images corresponds to one of the 12 landmarks used in the image registration illustrated in this example.

4.4.2 Image segmentation

The organs of interest were segmented based on the CT component of the PET/CT images using the 3D Slicer software, with the support of a human anatomy obtained from the literature [128]. 3D ROIs were manually separately delineated, slice by slice, to create the masks for each organ.

Manual segmentation was performed on CT images due to their better spatial resolution, allowing an easier distinction between tissues with different linear coefficients.

As already mentioned in this study, the ^{68}Ga-PSMA-11 radiopharmaceutical has a heterogeneous biodistribution in organs. Of all its target regions, those considered for the absorbed dose calculation were the liver, spleen, kidneys, and red bone marrow. These structures were chosen due to their biology, function, and presence in the radiation dosimetry literature. While the liver and spleen present a relatively intense radiopharmaceutical uptake and are sensitive to irradiation, the kidneys have an intense uptake due to the radiopharmaceutical biological elimination process. The red bone marrow was also considered, despite its segmentation being time-consuming and demanding because it encompasses many cell multiplication processes and comprises stem cells that are very sensitive to the effects of irradiation [129]. In the elderly, the red bone marrow is found mainly in flat bones, such as the cranial diploë, sternum, ribs, body of cervical, thoracic, lumbar and sacral-coccygeal vertebrae, ilium, and in the cancellous bone material at the epiphyseal ends of the long bones [130]. All these structures were included in this study. However, as the upper limbs were not fully included in the image acquisitions, only the lower limbs' long bones (femur and tibia) were segmented. As an example, the following figures 4.3 and 4.4 show the results of the manual segmentation of the kidneys and red bone marrow.

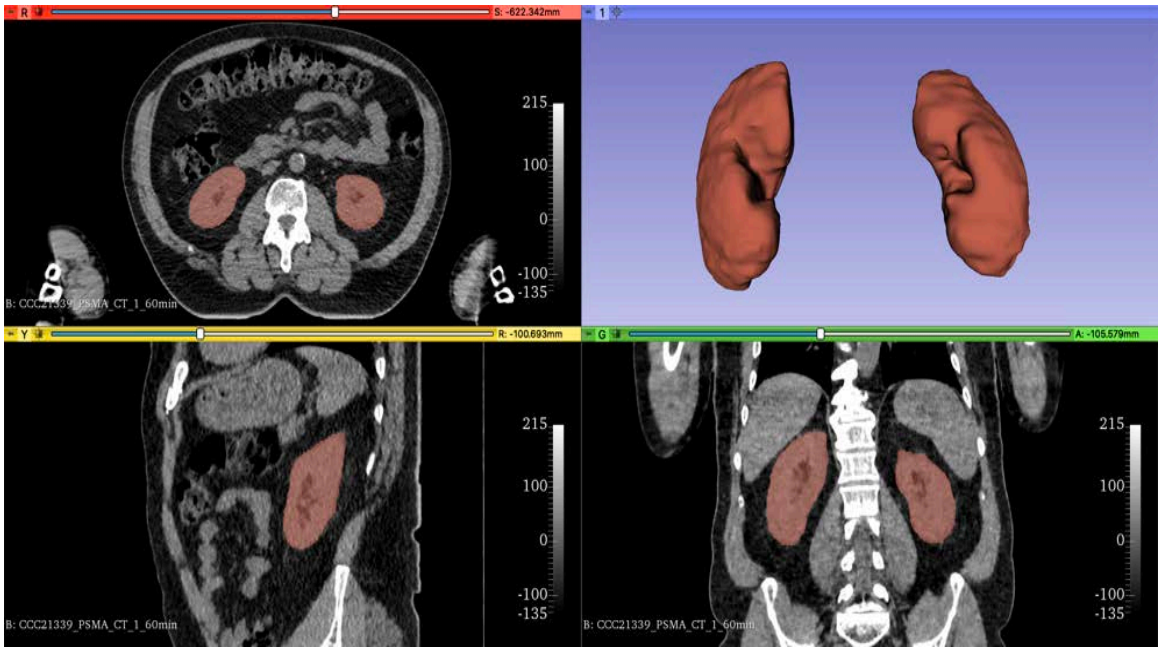

Figure 4.3: Mask created from manual segmentation of the kidneys in the axial (R), coronal (G), and sagittal (Y) slices of a patient CT image. A 3D view (1) of the obtained segmentation is also represented. The 'Grey' colormap was selected in Slicer. The color scale was adjusted to vary between black (low-density tissues) at -135 and white (high-density tissues) at 215.

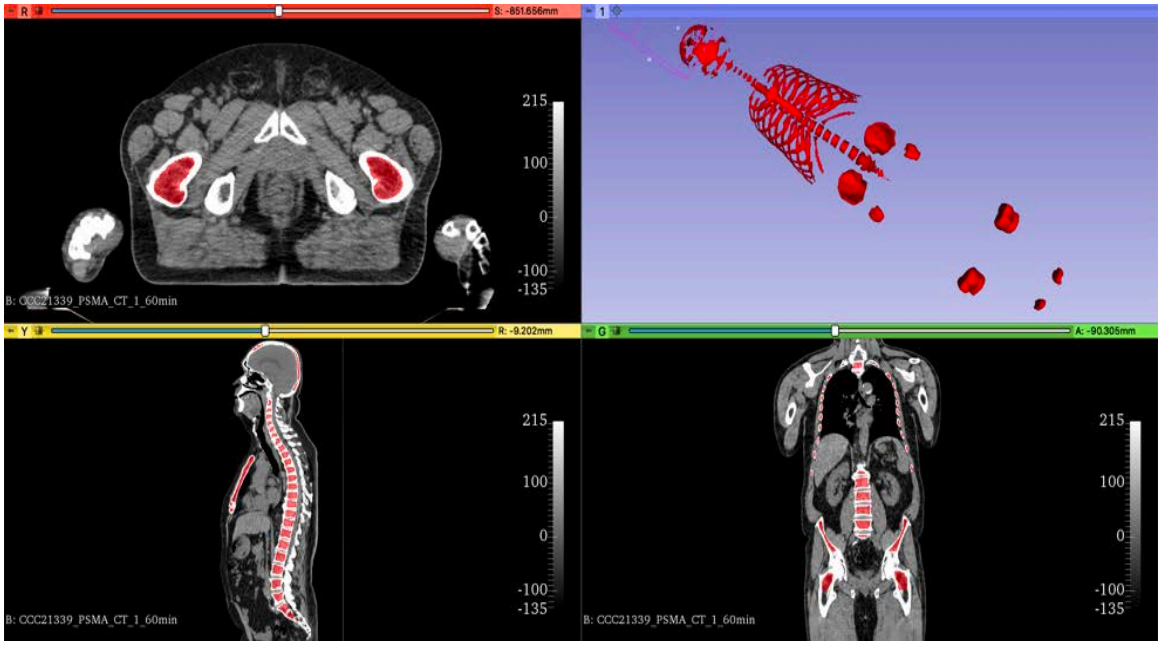

Figure 4.4: Mask created from manual segmentation of the red bone marrow in the axial (R), coronal (G), and sagittal (Y) slices of a patient CT image. A 3D view (1) of the obtained segmentation is also represented. The 'Grey' colormap was selected in Slicer. The color scale was adjusted to vary between black (low-density tissues) at -135 and white (high-density tissues) at 215.

4.4.3 Image resampling

A resampling operation was performed to transpose the masks obtained in the CT-based segmentation to the voxel size of the PET images.

The following specifications were selected in Slicer: nearest neighbor interpolation and pixel type binary. The nearest neighbor interpolation replicates the pixel value of the pixel located at the shortest distance. It is the simplest, fastest, and most efficient interpolation method applicable to masks [131]. The binary pixel type was also selected since for the calculation of the absorbed dose, the voxel values inside the mask needed to be equal to 1 and outside equal to 0.

4.4.4 Image calibration

The PET images and the masks were loaded into the MATLAB R2020a *(https://www.matlab.com)* [132] software from MathWorks®. The functions of the "Tools for NifTI and ANALYZE image" MATLAB package were used to manipulate these images.

During the reconstruction of the PET/CT images, the radiopharmaceutical concentration is corrected for radioisotope decay. Consequently, as the radioisotope decays over time, the resulting activity concentration is less than that indicated by PET images. Equation 4.1 shows the correction formula applied to the PET images (see Chapter 2.2.1). For the first subset of patients,

this formula was employed for t=30 min (using the PET image from the first scan) and t=75 min (using the PET image from the second scan), while for the second subset of patients, the times implemented were t=15 min (using the PET image from the first scan), t=45 min (using the PET image from the second scan) and t=75 min (using the PET image from the third scan). These times were chosen since they correspond to the intermediate moments between the beginning of each of the three image acquisitions. The 68 min half-life for ^{68}Ga was used in expression 4.1 (see Chapter 2.2.3).

$$A_{\text{PET\_correct}} = A_{\text{PET\_initial}} \times e^{-\frac{\ln 2}{T_{1/2}}t} = A_{\text{PET\_initial}} \times 2^{-\frac{t}{68\,\text{min}}} \quad (4.1)$$

Then, the calibrated activity concentration images (in Bq/ml) were multiplied by the voxels' volume (and by the factor 10^{-6}) to obtain the voxel-wise images calibrated in activity (MBq). This was needed because the S-values were expressed in mGy/MBq·s.

4.5 S-values kernel

To obtain the S-values, simulations were performed by Salvatore di Maria (PhD Researcher at C2TN, IST, Universidade de Lisboa) [119] using the MCNP6.1® *(https://www.mcnp.lanl.gov*) [115] Monte Carlo radiation transport code through an Intel Core i770 CPU @ 3.6 GHz (16 GB RAM) device.

The S-values for the ^{68}Ga radionuclide and cubical voxels of 4×4×4 mm^3 were computed for the following tissue materials: soft tissue and red bone marrow. The density and elemental composition of the materials were collected from the ICRU Report 44 [116] for the red bone marrow and from the NIST database [116] for the soft tissue.

The S-values were derived for an octant with dimension equal to 25×10×10 and isotropic 4 mm voxels for the materials mentioned above. For each simulated radiation spectrum, the emitting source was placed at the central cubic voxel. A spherical irradiation distribution (diameter equal to 4 mm) was chosen for this radioactive source.

To have a compromise between the accuracy of results and computational time, the cutoff energies were set to 250 eV and 1 keV for electrons/beta-plus radiation and photons, respectively. This means that particles outside their respective ranges of energy were terminated so that the computation time was not spent following them. A total number of 10^8 interactions and a maximum uncertainty of 5% were selected, resulting in a computational time spanning from some hours to some days, depending on the simulated radiation spectrum (e.g., high energy beta radiation was more time-consuming than low energy Auger electrons). The decay scheme of the ^{68}Ga was chosen [118], and the total energy deposited in the target voxel was tallied, the absorbed

fraction was calculated, and the S-values, indexed to the integer 3D coordinates of the target voxel (*i,j,k*), were obtained (see Chapter 3.3.1). The most peripheral voxels with the lowest S-values (e.g., the ones coming from low energy Auger electrons) were discarded since their influence on the results would be minimal, and the final S-values were acquired for an octant composed of 64 voxels and dimension equal to 4×4×4.

To validate the results obtained with MCNP6.1, simulations were performed for the ^{90}Y radionuclide and soft tissue. ^{90}Y was chosen since it is widely used in NM, and therefore, there are several S-values studies for this radioisotope. The simulation results were then compared with validated data present in the literature, obtained with the EGSnrc Monte Carlo program [110]. A radial comparison was made, only for the indexes *k*=0,1,2,3,4 and 5, and for voxels of 2.21 mm and 4.42 mm. Considering the decay scheme of ^{90}Y, beta radiation, X-rays, Auger electrons, and internal conversion electrons were simulated. However, since the beta radiation had a significantly higher yield (i.e., number of ejected particles per type of decay), it was the only form of decay considered in this validation. The results can be consulted in Appendix A (Table A.1 and Table A.2). The agreement seemed reasonable for the first four voxels in the two voxel sizes, and then the difference increased, as expected. However, up to the voxel *k*=3, the deviations were reasonable, in the order of 3%, and therefore still acceptable in the 2 cases: 9% (*k*=3 with 2.21 mm) and 17% (*k*=2 with 4.42 mm). It was important to notice that the contribution of this third voxel (*k*=3) to the central voxel (*k*=0) was already minimal, of about 0.3% (with 2.21 mm) and 0.0005% (with 4.42 mm). Thus, it was assumed that the simulation results were correct, and the S-values obtained for the ^{68}Ga were later used.

In addition to beta-plus decay, ^{68}Ga has other decay forms with other radiation emissions: Auger electrons, X-rays, and gamma photons. To obtain a realistic S-value for each voxel, a weighted sum was performed with the contribution of all yield decays. The following conversion factor was used to convert the units of the outputs of the MCNP6.1 code from MeV/g/particles to mGy/MBq/s:

$$CF = yield \times 1.6 \times 10^{-7} \times 10^{6} \quad (4.2)$$

where the *yield* component differs depending on the type of decay (Annex I), 1.6×10^{-7} is the conversion factor from MeV/g to mGy, and 10^6 is the MBq unit (1 Bq=decay/s).

The following Equations 4.3 and 4.4 describe the formulas applied to calculate the S-values and the respective uncertainties. It is important to note that the dimension *dim* is equal to 4 in this particular case since the indexes ranged from 0 to 3.

$$S_{i,j,k} = \sum_{i,j,k=0}^{dim-1} \left(0.889 S_{\mathrm{beta_{i,j,k}}} + 0.411 S_{\mathrm{auger_{i,j,k}}} + 0.569 S_{\mathrm{xrays_{i,j,k}}} + 0.0359 S_{\mathrm{gamma_{i,j,k}}}\right) \quad (4.3)$$

$$\sigma^2{}_{i,j,k} = \sum_{i,j,k=0}^{dim-1} \left[(0.889\sigma_{\mathrm{beta_{i,j,k}}})^2 + (0.441\sigma_{\mathrm{auger_{i,j,k}}})^2 + (0.569\sigma_{\mathrm{xrays_{i,j,k}}})^2 + (0.0359\sigma_{\mathrm{gamma_{i,j,k}}})^2\right] \quad (4.4)$$

Since the irradiation geometry was spherical, the S-values in voxels positioned at an equal distance from the central voxel were expected to be equal. However, due to the uncertainties of the simulated values, the S-values were not exactly symmetric. Thus, for each set of voxels positioned an equal distance to the center, the mean value of the respective S-values was calculated and assigned to all symmetric voxels. This smoothing operation was performed to obtain a better accuracy of the absorbed dose values. All the S-values used in this work can be consulted in Appendix A (Table A.3 and Table A.4).

The S-values for the two tissue materials (soft tissue and red bone marrow) were recorded in a text file and then imported into the developed MATLAB code and used in this study. This data was rearranged into one octant with 4×4×4 voxels, and then a 7×7×7 kernel was generated for each of the two tissues by symmetrically filling in the remaining seven octants.

4.6 Absorbed dose

4.6.1 3D absorbed dose distribution

The convolution of the voxel S-kernels (mGy/MBq·s) and the PET activity maps (MBq) resulted in voxel-wise absorbed dose rate distributions (mGy/s), as already mentioned in Chapter 3.3.1. This convolution operation was performed in the MATLAB software. Conceptually, the convolution operation can be described as follows: the kernel slid through the PET image, and the absorbed dose rate was calculated for each central target voxel through the activity contribution of the surrounding source voxels and the target voxel itself. After calculating the absorbed dose rate in the first target voxel, the kernel continued the scanning process to another voxel, and so on for all the voxels in the PET image (Figure 4.5).

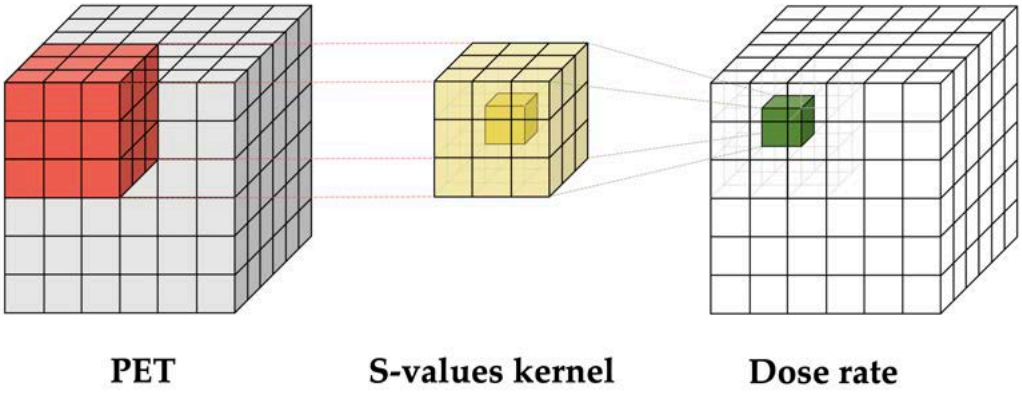

Figure 4.5: Convolution operation of the voxel S-kernel with the PET image. The output of this operation is the voxel-wise absorbed dose rate distribution. The voxels of the kernel and the PET image's voxels must have the same size, which was 4 mm cubic voxels in this study. Adapted from [133].

Equation 4.5 shows how the dose rates for each target voxel were calculated. While the S-kernel coordinate system was (*ii,jj,kk*), (*i,j,k*) was PET's coordinate system. *dim1, dim2*, and *dim3* were the PET dimensions in the *i,j*, and *k* directions, respectively. For each target voxel, *dim-1* voxels in each of the three directions are required for its dose calculation. Consequently, the application of this methodology for the dose rate calculation creates a voxel frame composed of zeros. In this study, a frame with a thickness of 3 voxels in each direction was produced, but it did not alter the precision in quantifying the absorbed dose in the ROIs.

$$\dot{D}_{i,j,k} = \sum_{i=dim}^{dim1-(dim-1)} \sum_{j=dim}^{dim2-(dim-1)} \sum_{k=dim}^{dim3-(dim-1)} \sum_{ii,jj,kk=-(dim-1)}^{dim-1} \left(S_{\mathrm{ii+dim,jj+dim,kk+dim}} \cdot A_{\mathrm{i+ii,j+jj,k+kk}} \right) \quad (4.5)$$

The absorbed dose was obtained by the temporal integration of the absorbed dose rate, as explained in Equation 3.5 of Chapter 3.3.1. To calculate the integral over time, a function was created in MATLAB. Equations 4.6 and 4.7 show how the total absorbed dose distributions, dependent on the type of tissue under study, were calculated for the first and second subsets of patients, respectively. The integration limits were defined as 0 min, 45 min, and 75 min (in accordance with Chapter 4.4.4) and infinity, as recommended in MIRD Pamphlet No. 21 [102]. Considering the first subset of patients, with two acquisitions, $\dot{D}_1$ is the dose rate calculated using the PET image from the first scan corrected for 30 min and $\dot{D}_2$ is the dose rate calculated using the PET image from the second scan corrected for 75 min (see Chapter 4.4.4). On the other hand, since patients from the second subset have three acquisitions, $\dot{D'}_1$ is the dose rate calculated using the PET image from the first scan corrected for 15 min, $\dot{D'}_2$ is the dose rate calculated using the

PET image from the second scan corrected for 45 min and $\dot{D}'_3$ is the dose rate calculated using the PET image from the third scan corrected for 75 min (see Chapter 4.4.4).

$$D_{\mathrm{i,j,k}} = \int_0^{75} \dot{D}_{1_{\mathrm{i,j,k}}} + \int_{75}^{\infty} \dot{D}_{2_{\mathrm{i,j,k}}} \tag{4.6}$$

$$D_{\mathrm{i,j,k}} = \int_0^{45} \dot{D}'_{1_{\mathrm{i,j,k}}} + \int_{45}^{75} \dot{D}'_{2_{\mathrm{i,j,k}}} + \int_{75}^{\infty} \dot{D}'_{3_{\mathrm{i,j,k}}} \tag{4.7}$$

After estimating the voxel-wise absorbed dose distributions, the absorbed dose values in the ROIs were calculated. The binary masks and the absorbed dose distributions were simultaneously traversed. If the voxel value of the mask was equal to 1, the correspondent dose value was stored in that voxel position and also in a column vector. Otherwise, the voxel value was assigned to 0. It is important to reinforce that the estimation of each absorbed dose distribution differed depending on the segment considered. For the liver, spleen, and kidneys, only the dose distributions calculated for the soft tissue material were employed. The same notion was applied for the red bone marrow and red bone marrow kernel.

4.6.2 Dose-volume histogram

The SlicerRT open-source radiotherapy extension in the 3D Slicer software was used to obtain the cDVHs in each organ [134].

The mean, median, and SD were the statistics analyzed in these graphics. The first two statistics were assessed as described in Chapter 3.3.3, whereas the SD was obtained directly from the 3D Slicer platform.

No comparison was made with DVHs present in the literature since each histogram is unique for a specific combination of patient and organ. Thus, these cDVHs were obtained only to visually corroborate the statistical results acquired through the methodology described in the previous section.

4.6.3 Dosimetry analysis

The column vectors filled with the voxel dose values were used for the statistical analysis in the MATLAB software. The mean, median, minimum, maximum, and SD were calculated for each segment. Table 4.3 shows the expressions of the statistics employed, considering *D* the absorbed dose values in the segments' voxels and *N* the number of voxels in the vector.

Table 4.3 – Implementation of the statistics used in this study.

Statistics	**Methods***
Mean	$\bar{D} = \frac{1}{N}\sum_{i}^{N} D(i)$
Median	The 50th percentile of D.
Minimum	The minimum intensity value of D.
SD	$\sigma_{\mathrm{D}} = \left(\frac{1}{N-1}\sum_{i=1}^{N}(D(i)-\bar{D})^2\right)^{\frac{1}{2}}$
Maximum	The maximum intensity value of D.

**D* is the set of absorbed dose values in the segments' voxels and *N* is the number of voxels in the vector.

The dose statistics in mGy were then divided by the administered activity (which differed from patient to patient) to obtain dose values in the mGy/MBq unit as in the literature.

4.6.4 Statistical analysis

Data were compared to values reported in the literature. Detailed dosimetry data were available for liver, spleen, kidneys, and red bone marrow from the studies by Asfhar-Oromieh et al. [57] and Pfob et al. [58]. In the studies conducted by Green et al. [59] and Demirci et al [60], only the mean absorbed dose values are presented. Furthermore, a study by Sandgren et al. [61] disclosed median, minimum, and maximum dose values.

Graphical data comparisons, based on the mean, median, and SD, were used in this study for an overall comparison of the results for all segments.

The range was calculated so that the variability of the mean and median dose values was measured for each organ, while the deviation was computed to compare the values obtained in this work with the values present in the literature. The following equation shows the formula employed in the calculation of the deviation:

$$E_{\mathrm{R}}(\%) = \frac{D_{\mathrm{P}} - D_{\mathrm{L}}}{D_{\mathrm{L}}} \times 100 \tag{4.8}$$

where D_{P} is the dose value estimated in the present study, and D_{L} is the dose in the literature. The latter was chosen as reference since the objective was to compare the obtained values with the values already published and, therefore, these were considered as the reference for the present work.

5

Results

5.1 3D absorbed dose distributions

As a result of the convolution of the activity images with the S-values, absorbed dose distributions were obtained for each selected organ of each patient (Figure 5.1–Figure 5.6). To facilitate the visualization of anatomical structures, CT images were overlaid with an opacity of 40%. Only the axial slices are shown in these figures. The coronal and sagittal slices and the 3D perspectives can be consulted in Appendix B (Figure B.1–Figure B.24). Since the purpose of obtaining these images was to visually study the absorbed dose distribution in the patients' organs, there is a color scale subtitled with the respective dose values in mGy. As a consequence of the variability of the absorbed dose distributions in the four organs and in the six patients, the color scales were adapted on a case-by-case basis. Consequently, it is easy to identify regions with higher and lower absorbed doses through the contrast of colors associated with higher values (white) and lower values (black).

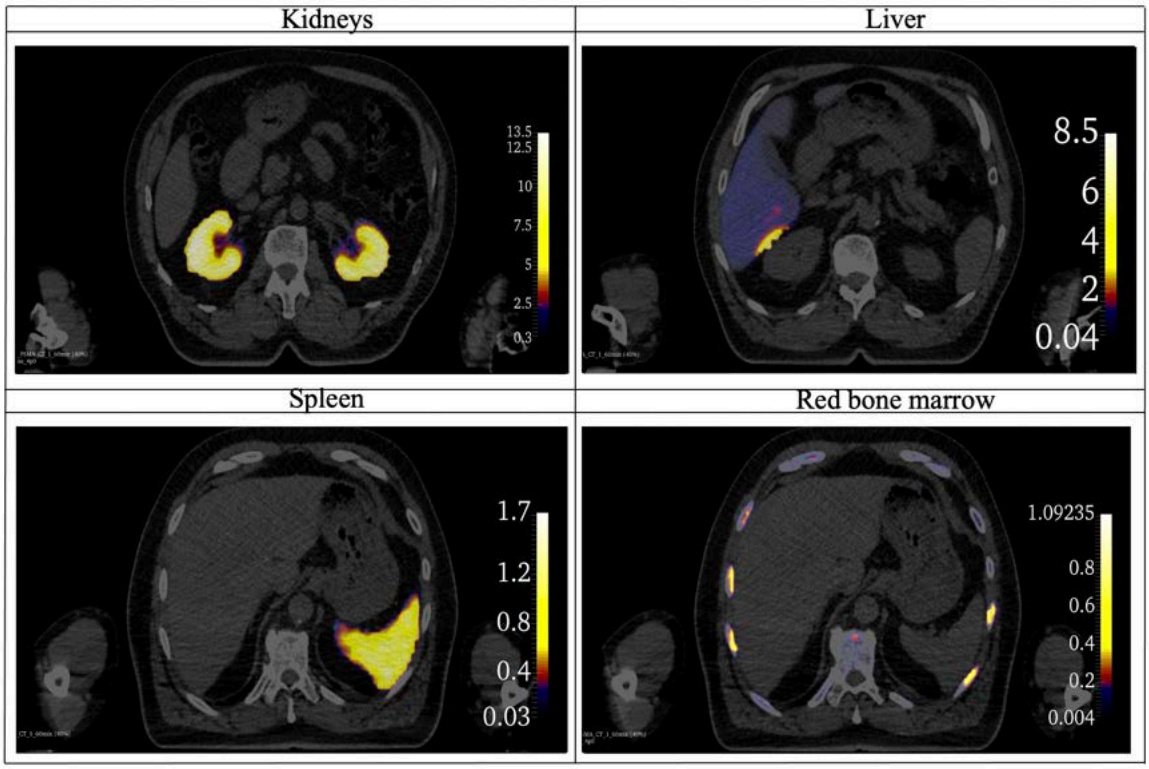

Figure 5.1: Four axial slices of the absorbed dose distributions in the kidneys, liver, spleen, and red bone marrow of patient 1. The scalar bar located on the right in the four images is expressed in mGy.

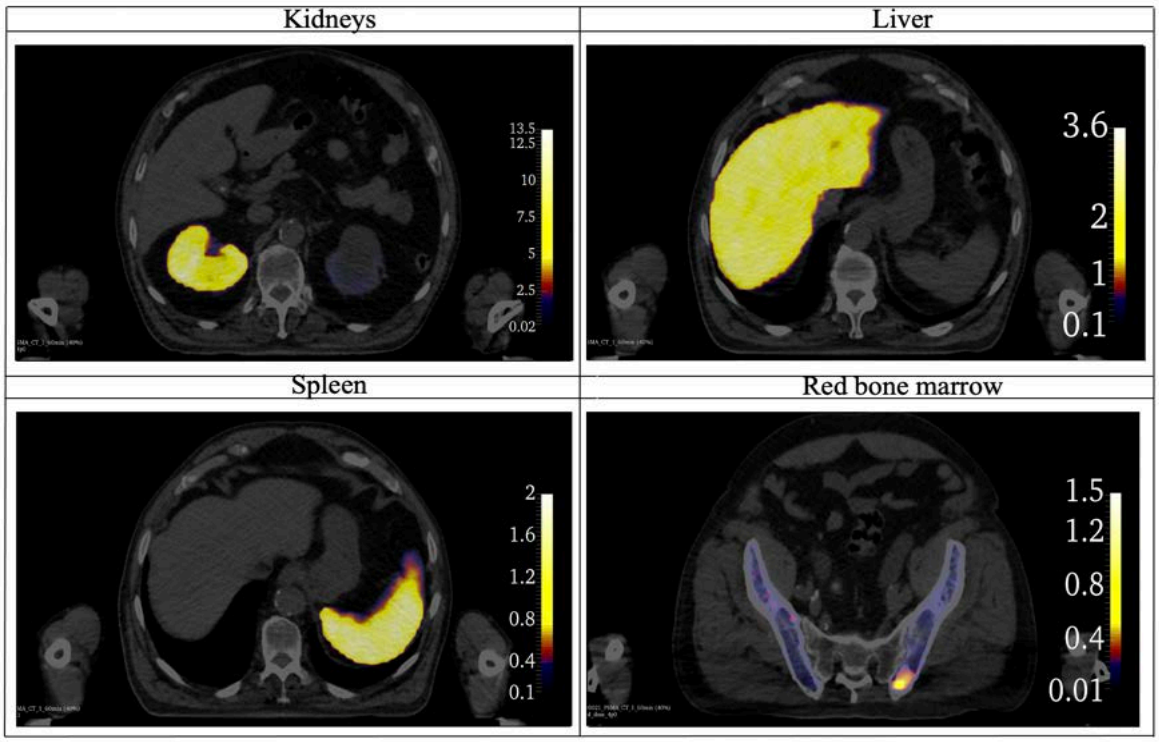

Figure 5.2: Four axial slices of the absorbed dose distributions in the kidneys, liver, spleen, and red bone marrow of patient 2. The scalar bar located on the right in the four images is expressed in mGy.

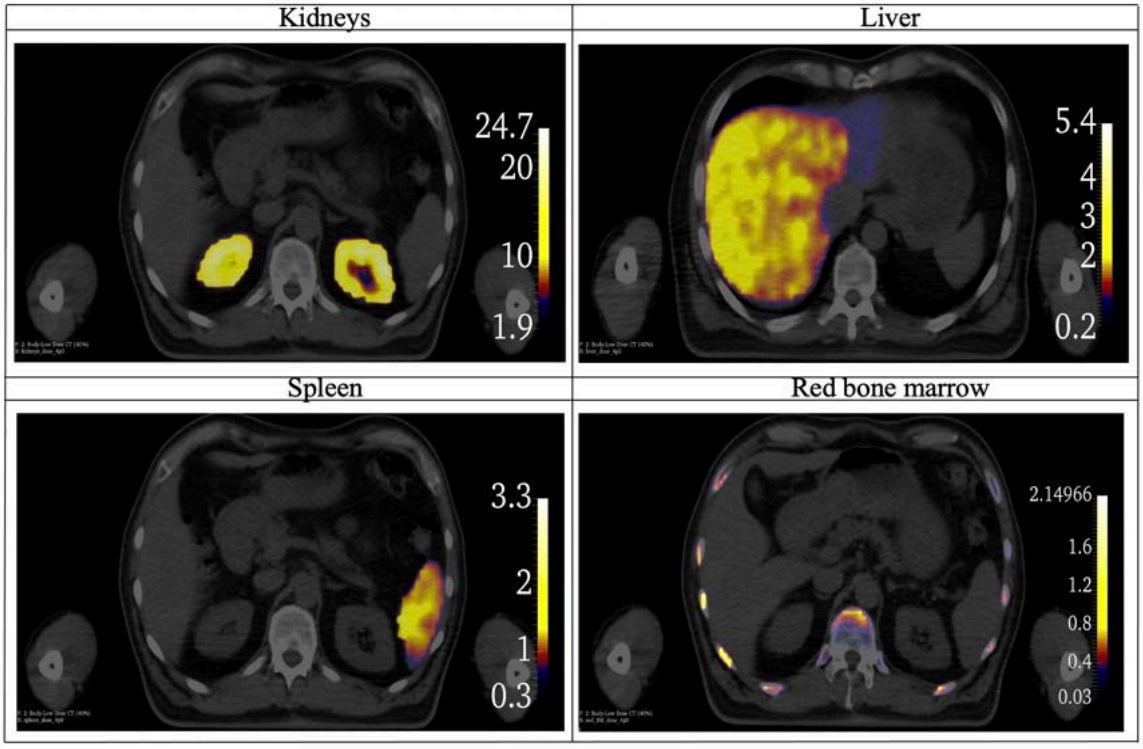

Figure 5.3: Four axial slices of the absorbed dose distributions in the kidneys, liver, spleen, and red bone marrow of patient 3. The scalar bar located on the right in the four images is expressed in mGy.

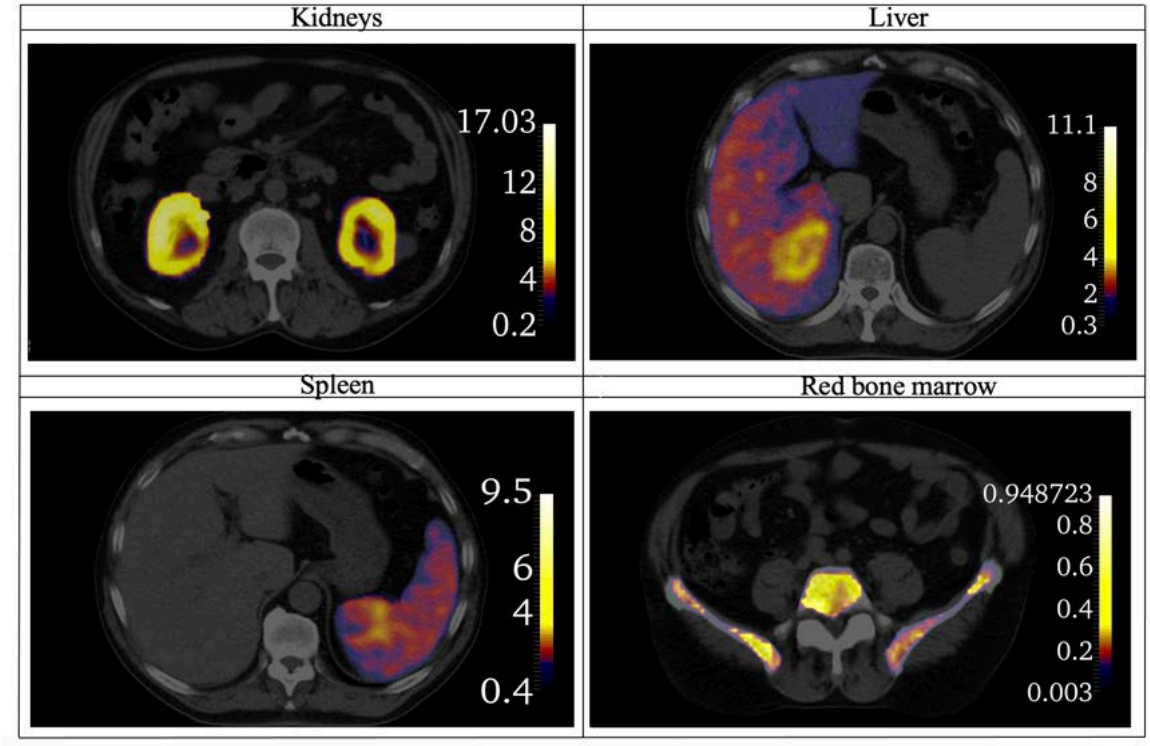

Figure 5.4: Four axial slices of the absorbed dose distributions in the kidneys, liver, spleen, and red bone marrow of patient 4. The scalar bar located on the right in the four images is expressed in mGy.

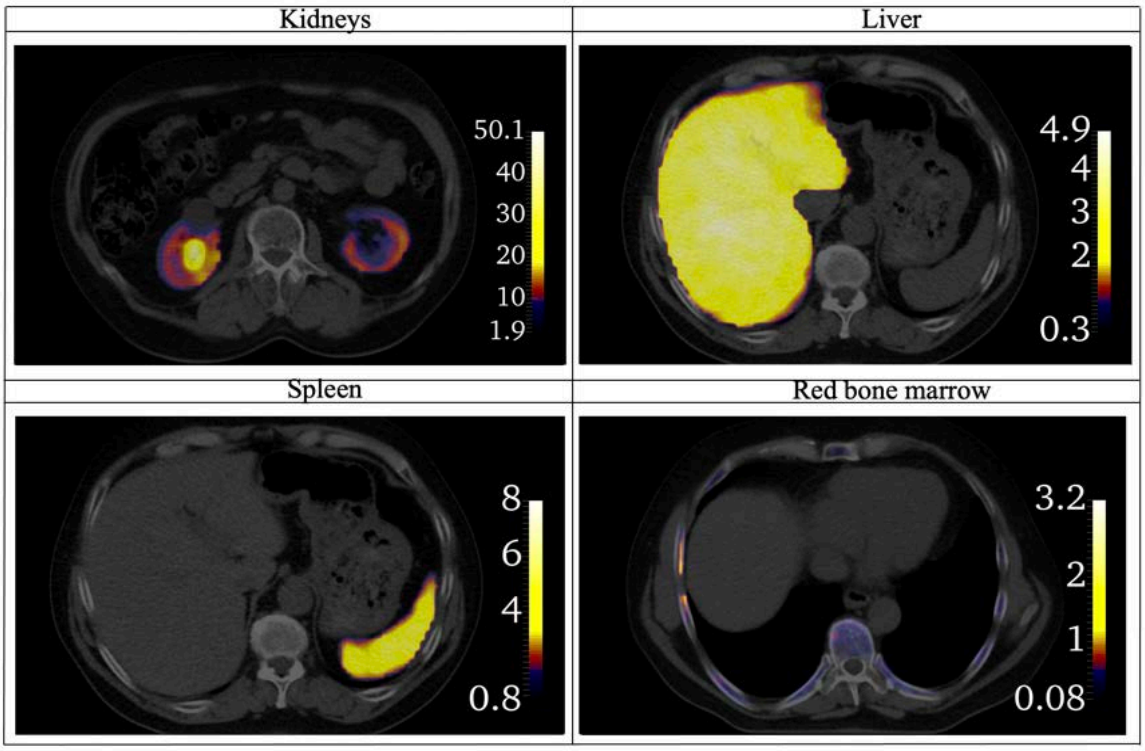

Figure 5.5: Four axial slices of the absorbed dose distributions in the kidneys, liver, spleen, and red bone marrow of patient 5. The scalar bar located on the right in the four images is expressed in mGy.

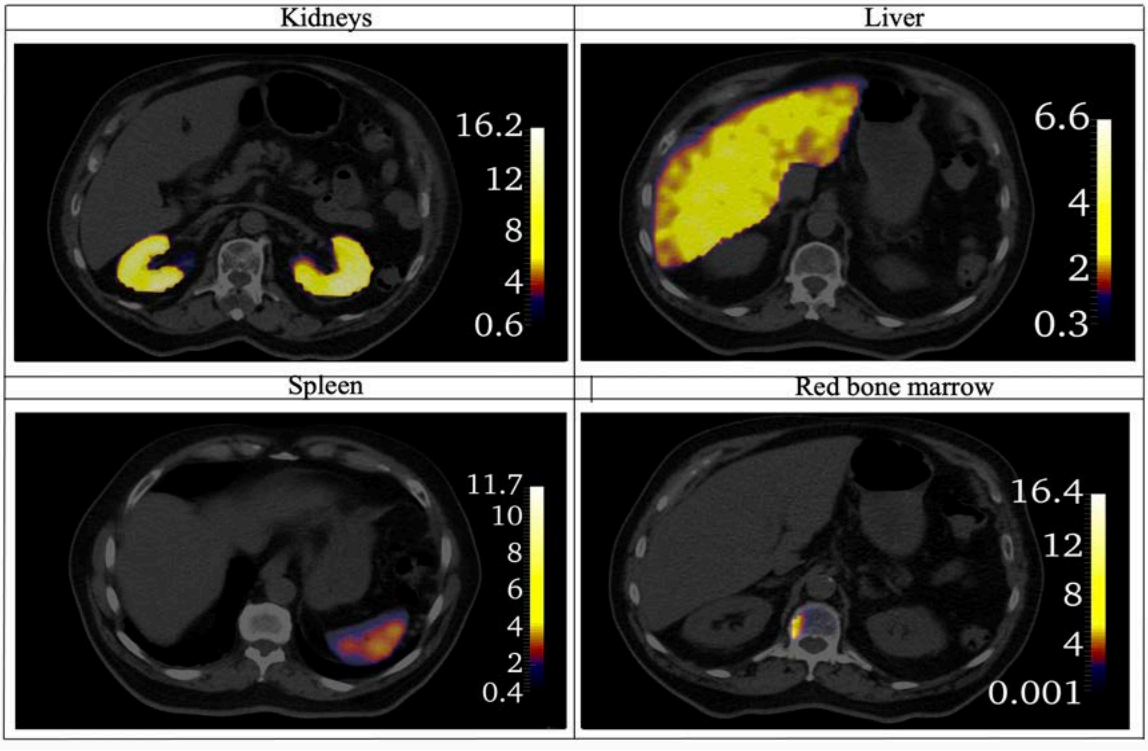

Figure 5.6: Four axial slices of the absorbed dose distributions in the kidneys, liver, spleen, and red bone marrow of patient 6. The scalar bar located on the right in the four images is expressed in mGy.

5.2 Dose-volume histograms

The following figures show the results of the step explained in Chapter 4.6.2. Considering all the patients included in this study, the cDVHs of the selected organs can be found in Figures 5.7 to 5.12.

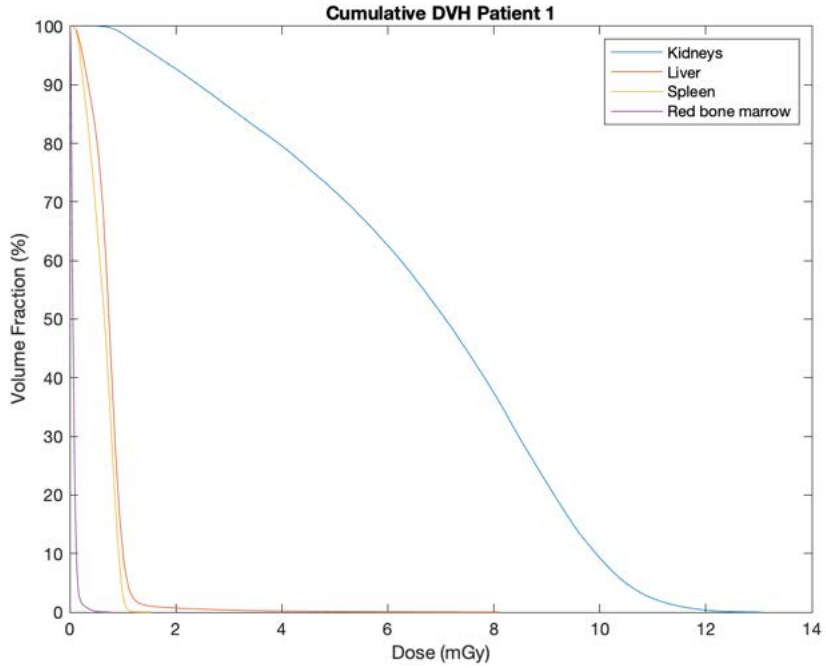

Figure 5.7: Cumulative dose-volume histogram of patient 1, including the kidneys, liver, spleen, and red bone marrow.

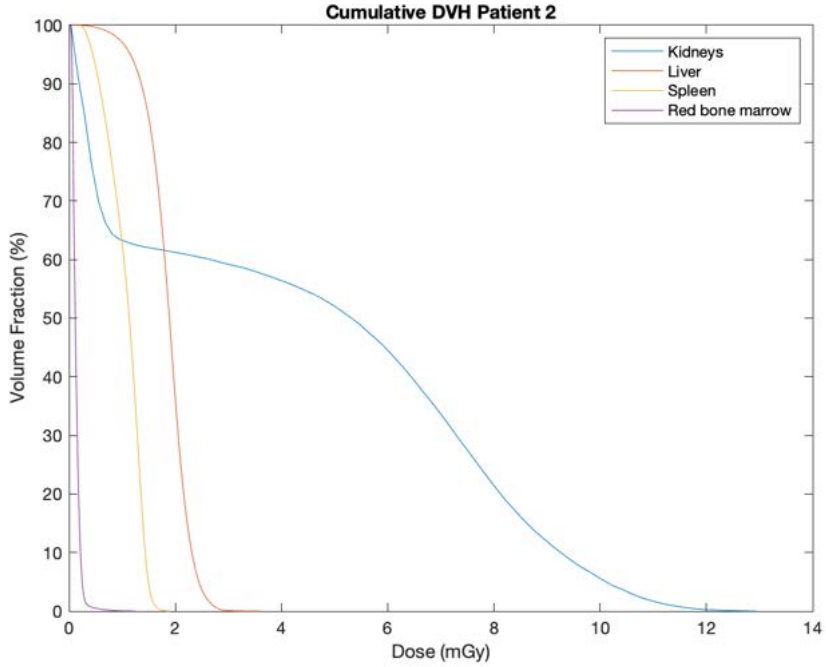

Figure 5.8: Cumulative dose-volume histogram of patient 2, including the kidneys, liver, spleen, and red bone marrow.

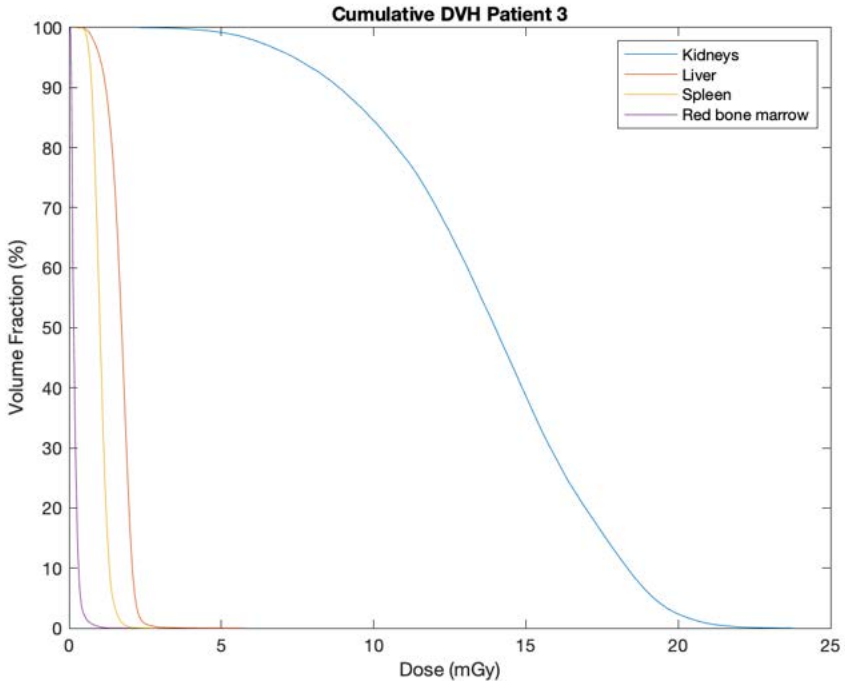

Figure 5.9: Cumulative dose-volume histogram of patient 3, including the kidneys, liver, spleen, and red bone marrow.

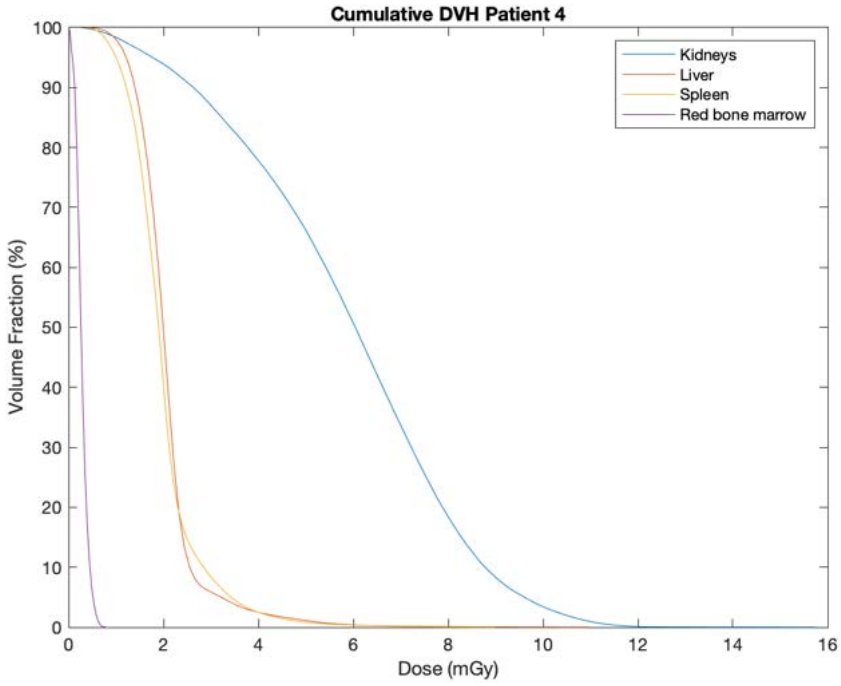

Figure 5.10: Cumulative dose-volume histogram of patient 4, including the kidneys, liver, spleen, and red bone marrow.

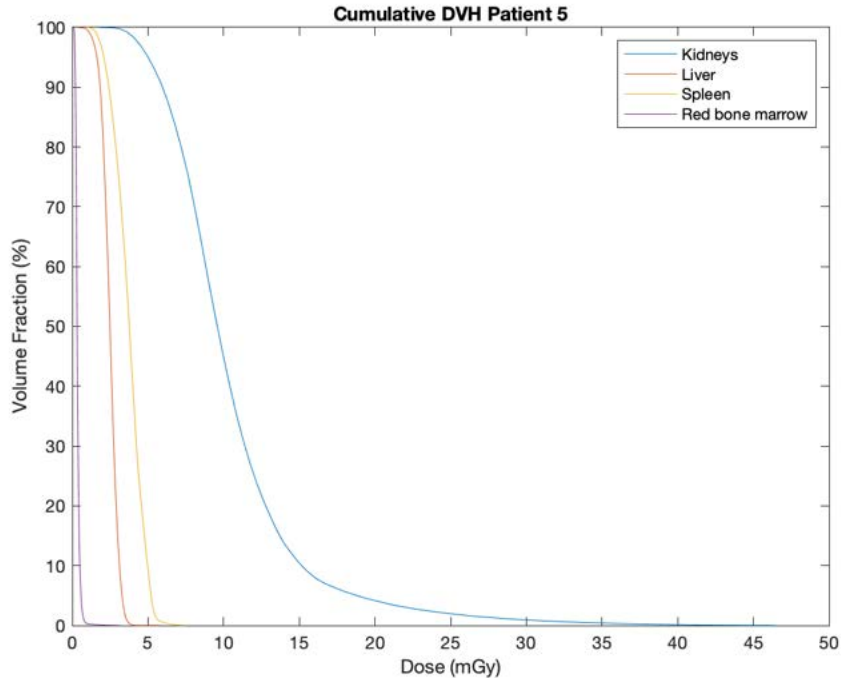

Figure 5.11: Cumulative dose-volume histogram of patient 5, including the kidneys, liver, spleen, and red bone marrow.

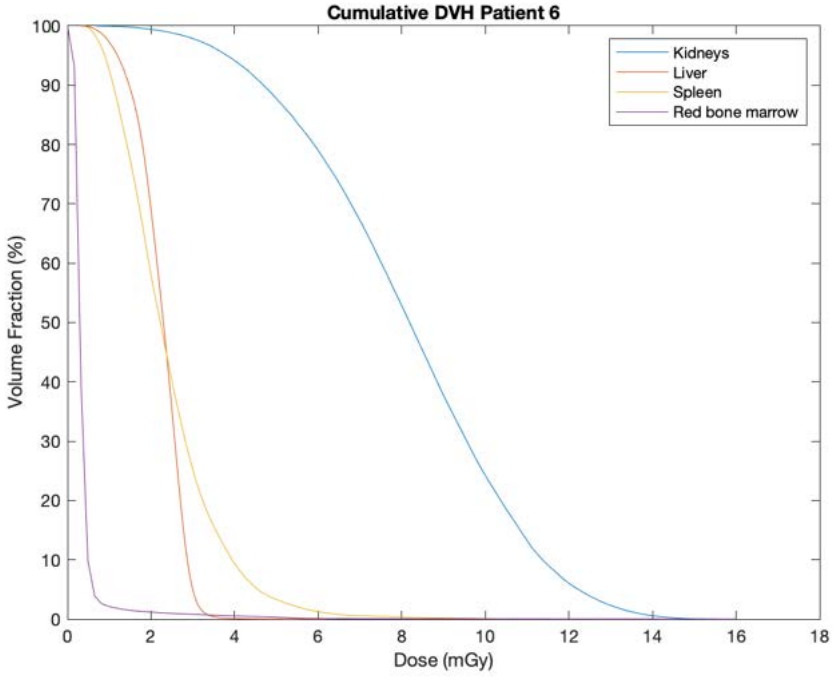

Figure 5.12: Cumulative dose-volume histogram of patient 6, including the kidneys, liver, spleen, and red bone marrow.

As explained in Chapter 4.6.2, the mean, median and SD dose values in the kidneys, liver, spleen, and red bone marrow of the six patients enrolled in this study were determined from the analysis of the cDVHs presented above and are exhibited in the following table (Table 5.1).

Table 5.1: Mean, median and SD dose values in mGy obtained from the analysis of the cDVHs of the six patients.

Organ	**Statistics**	**Patient 1 (mGy)**	**Patient 2 (mGy)**	**Patient 3 (mGy)**	**Patient 4 (mGy)**	**Patient 5 (mGy)**	**Patient 6 (mGy)**
Kidneys	Mean	6.114	4.519	11.495	5.632	8.642	7.421
	Median	7.143	4.891	13.889	5.945	9.932	8.051
	SD	2.886	3.770	3.828	2.458	4.899	2.677
Liver	Mean	0.679	1.703	1.408	1.785	2.154	1.921
	Median	0.912	1.870	1.924	2.167	2.462	2.367
	SD	0.307	0.408	0.372	0.712	0.510	0.556
Spleen	Mean	0.577	0.875	0.660	1.610	2.777	2.022
	Median	0.899	1.083	1.246	1.875	3.910	2.283
	SD	0.250	0.328	0.243	0.780	0.960	1.343
Red bone marrow	Mean	0.065	0.115	0.143	0.271	0.259	0.365
	Median	0.063	0.100	0.200	0.191	0.353	0.348
	SD	0.054	0.079	0.119	0.132	0.147	0.490

Furthermore, by analyzing the cDVHs presented, it is possible to verify that the theoretical concept that relates the extent of the curve plateau with the standard deviation and irradiation uniformity/non-uniformity cannot be applied. In this work, using diagnostic studies with radioisotopes, the objective is to analyze the absorbed dose distributions in the total volume of the organs and not in specific lesions. These dose distributions possess a more non-uniform nature, and therefore, the shape of the cDVH curve has a greater impact than the extent of the plateau in the study of the uniformity/non-uniformity of radiopharmaceutical uptake in the organs of interest.

With these cumulative dose-volume histograms, it was possible to analyze the dose distribution in the patient's organs simultaneously. In the following chapter, the absorbed dose values used for comparison with the dose values present in the literature are shown.

5.3 Dosimetry Results

The dosimetry results for the patient cohort are reported in Table 5.2 and Figures 5.13 to 5.16.

Table 5.2: Results of the dosimetry study expressed in mGy/MBq. The mean, median, minimum, maximum, and SD were calculated for the organs under study, considering each patient individually and the six patients simultaneously (last column on the right).

Organ	Statistics*	Patient 1 (mGy/MBq)	Patient 2 (mGy/MBq)	Patient 3 (mGy/MBq)	Patient 4 (mGy/MBq)	Patient 5 (mGy/MBq)	Patient 6 (mGy/MBq)	Overall Absorbed Dose (mGy/MBq) **
Kidneys	Mean	0.0737	0.0393	0.1121	0.0316	0.0590	0.0490	0.0561
	Median	0.0779	0.0406	0.1140	0.0322	0.0545	0.0495	0.0499
	Minimum	0.0037	<0.0010	0.0160	0.0014	0.0115	0.0042	<0.0010
	Maximum	0.1529	0.1229	0.2039	0.0939	0.2908	0.0992	0.2879
	SD	0.0338	0.0338	0.0331	0.0138	0.0286	0.0172	0.0367
Liver	Mean	0.0082	0.0165	0.0137	0.0112	0.0142	0.0135	0.0132
	Median	0.0082	0.0169	0.0141	0.0109	0.0144	0.0139	0.0126
	Minimum	<0.0010	0.0012	0.0019	0.0015	0.0020	0.0019	<0.0010
	Maximum	0.0960	0.0322	0.0446	0.0609	0.0281	0.0404	0.0962
	SD	0.0044	0.0041	0.0034	0.0041	0.0031	0.0037	0.0046
Spleen	Mean	0.0069	0.0093	0.0084	0.0107	0.0212	0.0149	0.0114
	Median	0.0071	0.0099	0.0082	0.0103	0.0216	0.0134	0.0102
	Minimum	<0.0010	0.0016	0.0030	0.0020	0.0051	0.0026	<0.0010
	Maximum	0.0183	0.0188	0.0265	0.0521	0.0462	0.0715	0.0718
	SD	0.0029	0.0033	0.0023	0.0045	0.0061	0.0085	0.0064
Red bone marrow	Mean	<0.0010	0.0014	0.0017	0.0015	0.0021	0.0022	0.0015
	Median	<0.0010	0.0012	0.0014	0.0014	0.0019	0.0018	0.0013
	Minimum	<0.0010	<0.0010	<0.0010	<0.0010	<0.0010	<0.0010	<0.0010
	Maximum	0.0113	0.0130	0.0162	0.0048	0.0184	0.1003	0.1009
	SD	<0.0010	<0.0010	<0.0010	<0.0010	<0.0010	0.0016	0.0013

* According to the specifications of the Philips Vereos Digital PET/CT, the maximum quantitative uncertainty of activity is 5% and the maximum uncertainty of the S-values is, as already mentioned, 5%. Thus, the uncertainty of these dosimetry statistical values will never be less than 5%.

** These absorbed dose values were calculated for each organ considering the voxel-wise absorbed dose distributions of the six patients.

Figures 5.13 to 5.16 show the dosimetric variability of the six patients, which is well characterized by the statistical mean, median, and SD values in each of the four organs under study.

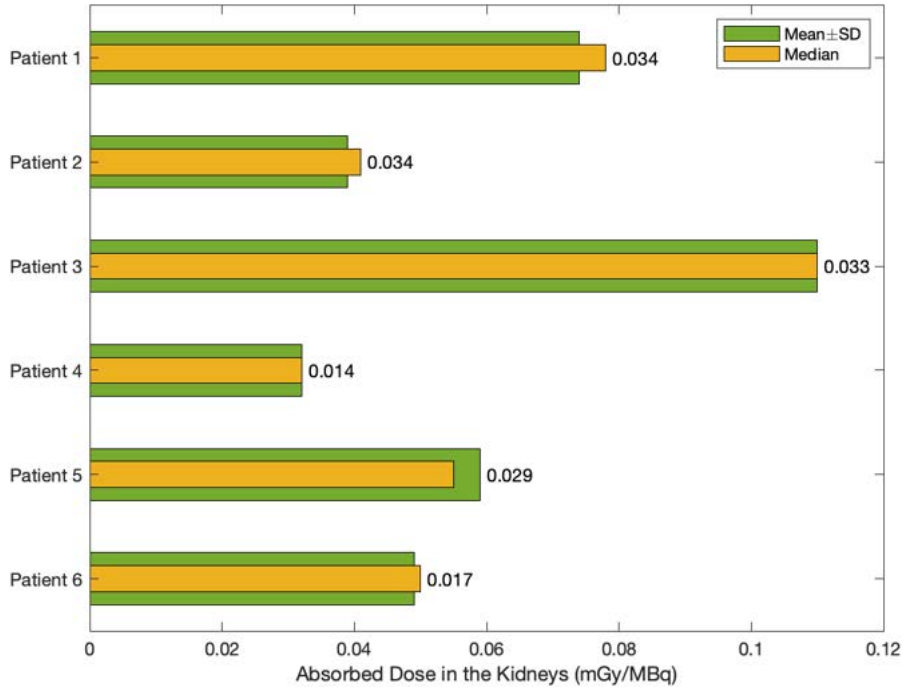

Figure 5.13: Mean±SD and median absorbed dose values in the kidneys of the six patients. The SD dose value of each patient corresponds to the value positioned in front of the respective bar.

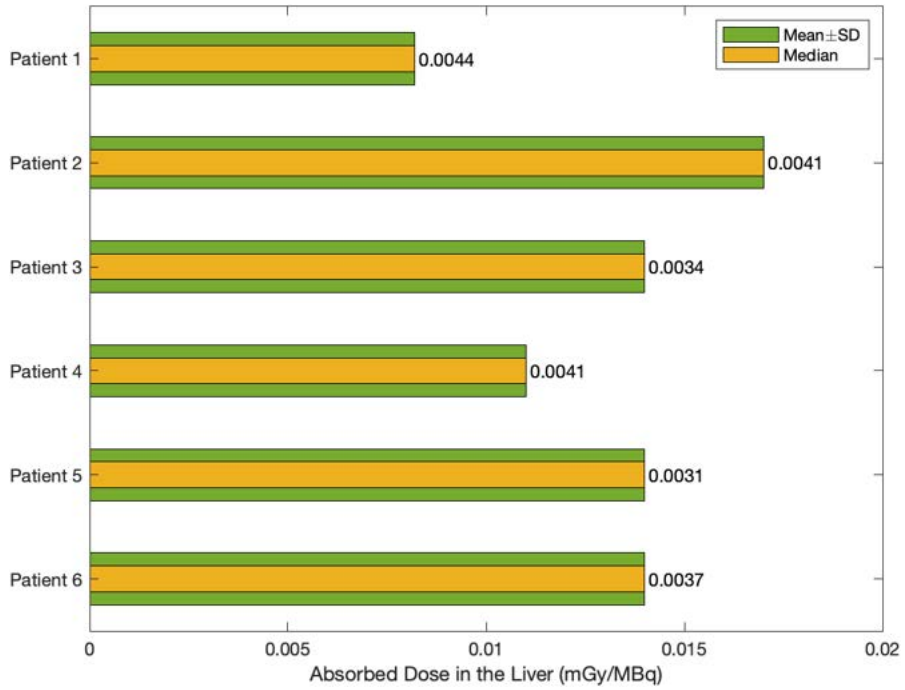

Figure 5.14: Mean±SD and median absorbed dose values in the liver of the six patients. The SD dose value of each patient corresponds to the value positioned in front of the respective bar.

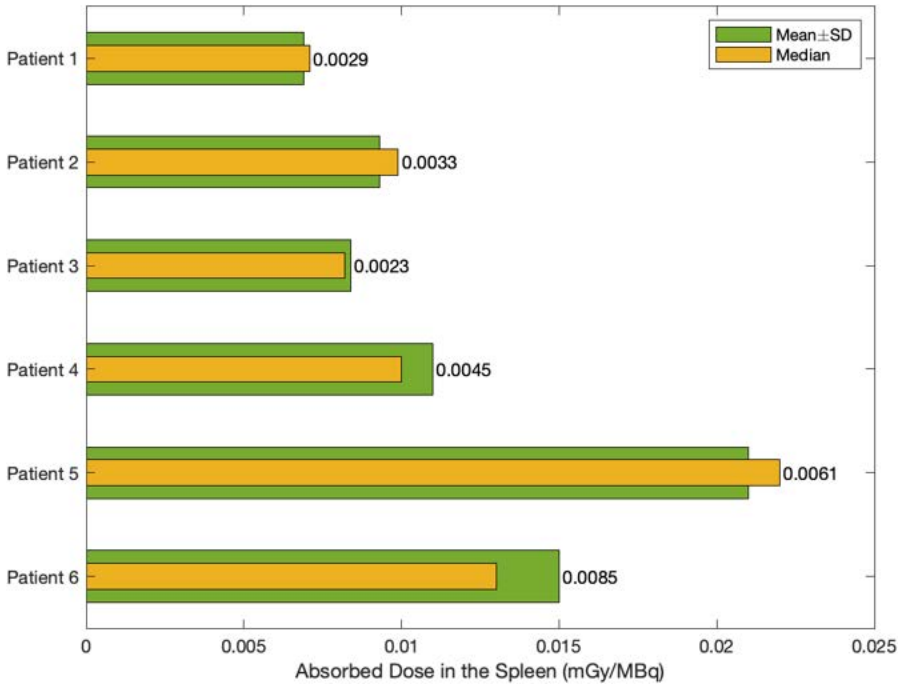

Figure 5.15: Mean±SD and median absorbed dose values in the spleen of the six patients. The SD dose value of each patient corresponds to the value positioned in front of the respective bar.

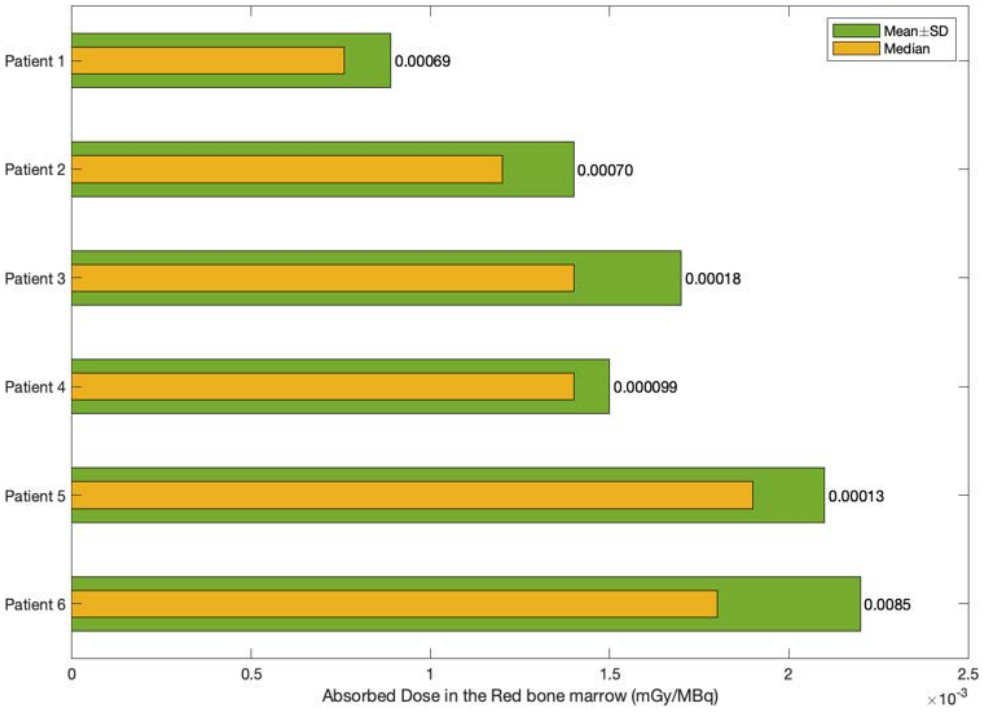

Figure 5.16: Mean±SD and median absorbed dose values in the red bone marrow of the six patients. The SD dose value of each patient corresponds to the value positioned in front of the respective bar.

The kidneys were the organs with the highest mean and median dose values in all patients, while the red bone marrow was the structure with these lowest values. Of the four organs, the

spleen and the liver were the organs with intermediate dose values, both of which showed a significant dose difference in the first and second subsets of patients. In the second subset, the mean dose values in the spleen were equal (patient 4) or higher (patients 5 and 6) than the liver values, a tendency that was not seen in patients 1, 2, and 3. The red bone marrow presented the lowest SD value, so it can be concluded that the dose distribution in this organ is more uniform than the dose distributions in the other organs. On the other hand, the kidneys presented the most non-uniform dose distribution since the SD is higher than that observed in the liver, spleen, and red bone marrow.

5.4 Comparison with previous studies

Table 5.3 shows the mean and median absorbed dose values and the SD per administered activity computed in this work and in previously published literature considering the same organs under study. It is important to note that the data published by Afshar-Oromieh et al. [57] and Pfob et al. [58] include the mean, median, and SD dose values, while Green et al. [59] and Demirci et al. [60] only report mean dose values and Sandgren et al. [61] only median dose values.

Table 5.3: Comparison between this study and previously published data regarding the mean, median, and SD dose values.

Organ	**Statistics**	**This work (mGy/MBq)**	**Afshar-Oromieh et al. [57] (mGy/MBq)**	**Pfob et al. [58] (mGy/MBq)**	**Green et al. [59] (mGy/MBq)**	**Demirci et al. [60] (mGy/MBq)**	**Sandgren et al. [61] (mGy/MBq)**
Kidneys	Mean	0.0561	0.2620	0.1220	0.4130	0.2460	
	Median	0.0499	0.2925	0.1210			0.2400
	SD	0.0367	0.0984	0.0444			
Liver	Mean	0.0132	0.0309	0.0214	0.0395	0.0294	
	Median	0.0126	0.0305	0.0207			0.0530
	SD	0.0046	0.0042	0.0032			
Spleen	Mean	0.0114	0.0446	0.0428	0.0581	0.0388	
	Median	0.0102	0.0423	0.0413			0.0460
	SD	0.0064	0.0209	0.0185			

Red bone marrow	Mean	0.0015	0.0092	0.0139	0.0103	0.0120	
	Median	0.0013	0.0092	0.0081			0.0150
	SD	0.0013	0.0003	0.0136			

Figures 5.17 to 5.20 show the mean, median, and SD absorbed dose values in the kidneys, liver, spleen, and red bone marrow, computed in the present work and in other literature studies. The variability of the absorbed dose values in the organs under study is shown in these figures. Considering the SDs of the first three studies, the present work presented less variability of the dose values in the spleen and similar variability in the kidneys and liver. On the other hand, in this study, less variability in the red bone marrow was obtained when compared to the work by Pfob et al. [58], but higher variability was found when compared to the data published by Afshar et al [57].

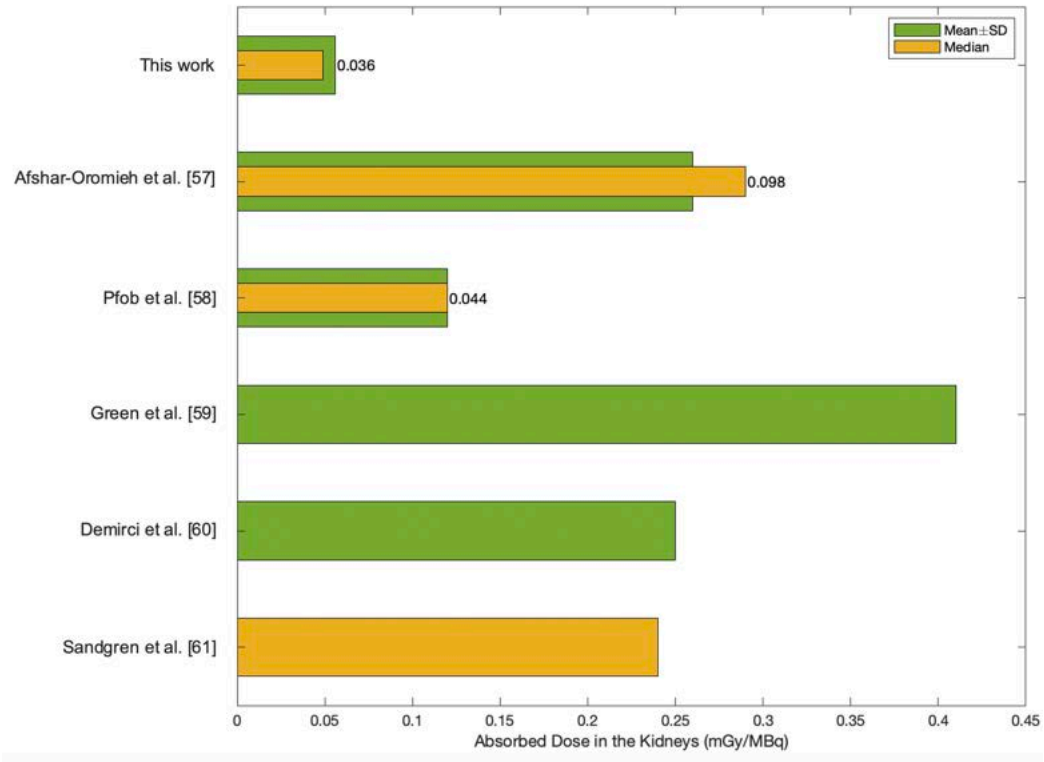

Figure 5.17: Comparison between this study and the previously published data regarding the mean, median, and SD dose values in the kidneys. The SD dose value of each study corresponds to the value positioned in front of the respective bar.

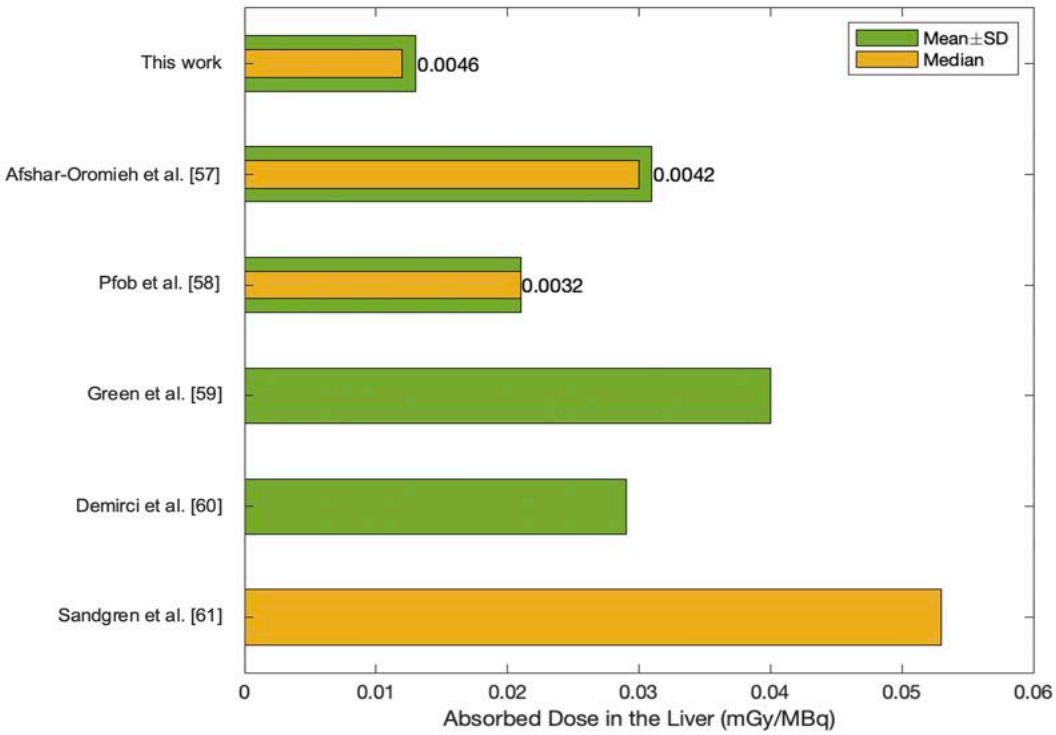

Figure 5.18: Comparison between this study and the previously published data regarding the mean, median, and SD dose values in the liver. The SD dose value of each study corresponds to the value positioned in front of the respective bar.

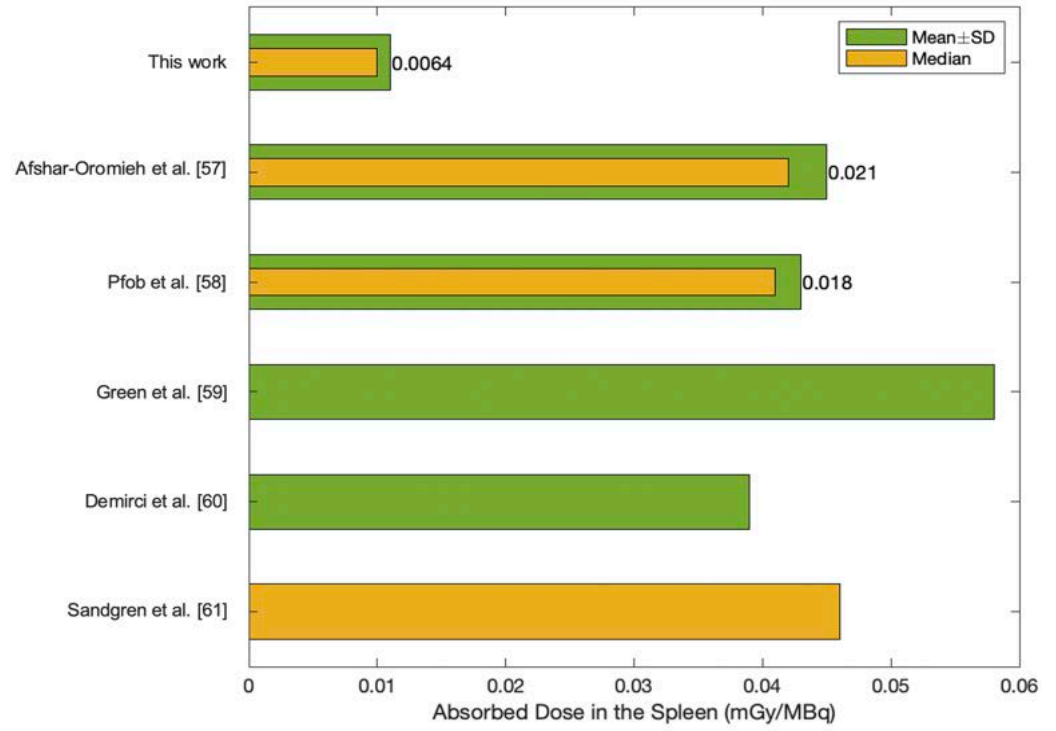

Figure 5.19: Comparison between this study and the previously published data regarding the mean, median, and SD dose values in the spleen. The SD dose value of each study corresponds to the value positioned in front of the respective bar.

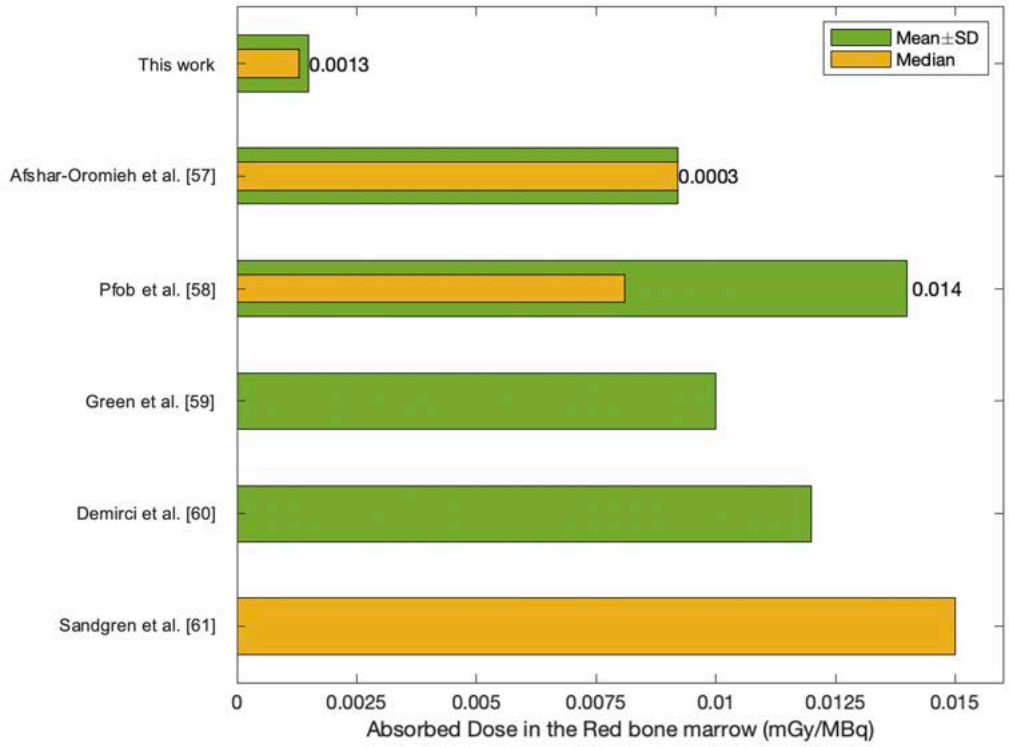

Figure 5.20: Comparison between this study and the previously published data regarding the mean, median, and SD dose values in the red bone marrow. The SD dose value of each study corresponds to the value positioned in front of the respective bar.

The following tables (Table 5.4, 5.5, and 5.6) show the range and deviation in terms of the mean and median dose values. The range was computed to measure the variability of the mean and median values in this study and in the literature for each organ. The deviation between the dose values calculated in this study and in previous studies was also computed.

Table 5.4: Range in terms of the mean and median dose values in the kidneys, liver, spleen, and red bone marrow.

Organ	**Range$_{Mean}$ (mGy/MBq)**	**Range$_{Median}$ (mGy/MBq)**
Kidneys	0.0561–0.4130	0.0499–0.2925
Liver	0.0132–0.0395	0.0126–0.0530
Spleen	0.0114–0.0581	0.0102–0.0460
Red bone marrow	0.0015–0.0139	0.0013–0.0150

Table 5.5: Deviation in terms of the mean dose values in the kidneys, liver, spleen, and red bone marrow, considering the studies by Afshar-Oroemieh et al. [57], Pfob et al. [58], Green et al. [59] and Demirci et al. [60] as references.

	E_{RMean} (%)			
Organ	**Afshar-Oromieh et al. [57]**	**Pfob et al. [58]**	**Green et al. [59]**	**Demirci et al. [60]**
Kidneys	-78.5	-53.3	-86.3	-77.6
Liver	-58.1	-38.1	-67.5	-55.2
Spleen	-75.6	-74.4	-81.0	-71.8
Red bone marrow	-83.7	-89.3	-85.0	-87.5

Table 5.6: Deviation in terms of the median dose values in the kidneys, liver, spleen, and red bone marrow, considering the studies by Afshar-Oroemieh et al. [57], Pfob et al. [58], and Sandgren et al. [61] as references.

	$E_{RMedian}$ (%)		
Organ	**Afshar-Oromieh et al. [57]**	**Pfob et al. [58]**	**Sandgren et al. [61]**
Kidneys	-83.1	-59.2	-79.6
Liver	-60.0	-42.9	-77.4
Spleen	-76.2	-75.6	-78.3
Red bone marrow	-85.9	-83.9	-91.3

In all studies, the kidneys received the highest absorbed doses, in contrast to the red bone marrow, which received the lowest absorbed dose values, compared to the other organs. The five literature studies exhibited similar mean and median dose results, particularly in the red bone marrow and liver, whereas the kidneys were the organs with the highest variability in terms of mean and median dose values. However, compared to previous studies, the dosimetry results in the present work for the four organs were lower, which can be observed in Figures 5.17 to 5.20 and Tables 5.5 and 5.6. A plausible explanation for these deviations is that the authors performed the dosimetry calculations at the compartment level and not at the voxel level, as in the present study. Consequently, a uniform distribution of the radiopharmaceutical in the organs was considered, resulting in an overestimation of the absorbed dose values.

6

Discussion and Conclusions

6.1 Discussion

Since the introduction of ^{68}Ga-PSMA-11 for PET imaging, PSMA-PET/CT has spread rapidly to many institutions. The aim of the present study was to perform internal radiation dosimetry estimates of six prostate cancer patients who underwent ^{68}Ga-PSMA-11 PET/CT in the Nuclear Medicine-Radiopharmacology Department at the Champalimaud Foundation. Subsequently, the results were compared with the available data in previous studies. The target organs included in this study were the kidneys, liver, spleen, and red bone marrow.

Since the innovation of this work is the dose calculation at the voxel level, the MIRD S-values approach at the voxel level was employed. For patients 1, 2, and 3, two sets of PET/CT images were acquired per patient, while for patients 4, 5, and 6, three sets were obtained per patient. PET/CT acquisitions were performed on a Philips Vereos PET/CT scanner. All PET images of each patient were registered in the same coordinate space and calibrated for radioisotope concentration at the time of image acquisition. The organs of interest of each patient were manually segmented based on CT images, and the masks were resampled to the PET voxel size. Afterward, the convolution of the S-kernels, obtained using the MCNP6.1 Monte Carlo Code, with the PET activity maps, resulted in absorbed dose rate distributions, which were subsequently time-integrated to take into account all radioisotope decays. The voxel-wise absorbed dose distributions in the organs of each patient (Figures 5.1–5.6) and the cDVHs (Figures 5.7–5.12) were successfully obtained. In addition, the mean, median, minimum, maximum, and SD of the absorbed dose values were also calculated (Table 5.2 and Figures 5.13–5.16). Afshar-Oromieh et al. [57], Pfob et al. [58], Green et al. [59], Demirci et al. [60] and Sandgren et al. [61] were the studies found in the literature and used here for comparison with the obtained results (Table 5.3 and Figures 5.17–

5.20). For this purpose, the range and deviation in terms of mean and median dose values were calculated for the four organs (Tables 5.4–5.6).

The voxel-wise absorbed dose distribution in the kidneys of patient 2 (Figure 5.2) shows that the dose values in the voxels of the left kidney were much lower compared to the values in the right kidney. In addition, the blue curve of the cDVH of patient 2 (Figure 5.8), referring to the kidneys, presents an irregular shape. After the study of the PET images, it was found that this patient had practically no radiopharmaceutical uptake in the left kidney since this is a non-functioning kidney. This loss of function was due to a progressive obstruction of urine flow at the junction of the left ureter with the bladder, which can lead to a functional recovery reaction by the contralateral kidney. For this reason, the absorbed dose values in the kidneys of patient 2 were not lower than the absorbed dose values in the kidneys of the remaining patients.

Regarding the six patients of this study, the kidneys received the highest absorbed doses, with a mean overall absorbed dose of 0.0561 mGy/MBq and a median overall absorbed dose of 0.0499 mGy/MBq. Thus, the kidneys were the critical organs in this study, which was expected due to the biological process of elimination of the radiopharmaceutical. The tracer uptake in the liver resulted in a significant mean absorbed dose from ^{68}Ga of approximately 0.0132 mGy/MBq and a median absorbed dose of 0.0126 mGy/MBq. This is less than the kidneys, but the second highest organ dose. The third organ with the highest dose was the spleen, receiving an estimated mean dose of 0.0114 mGy/MBq and a median dose of 0.0102 mGy/MBq. Of all organs, the red bone marrow received the lowest absorbed dose values (mean dose: 0.0015 mGy/MBq, median dose: 0.0013 mGy/MBq). This means that none of the patients included in this study had metastasis with intense foci of PSMA or hyperactivity in the red bone marrow, the latter possibly induced by medication. Considering all the patients and organs, the SDs at the voxel level were: red bone marrow (SD=0.0013 mGy/MBq), liver (SD=0.0046 mGy/MBq), spleen (SD=0.0064 mGy/MBq), and kidneys (SD=0.0367 mGy/MBq). Thus, it is possible to infer that the dose distribution in the red bone marrow was more uniform, followed by the distribution in the liver, spleen, and kidneys.

The spleen was the organ that showed the highest variability of results obtained after two acquisitions at 60 and 90 min p.i. (mean dose: 0.0069–0.0093 mGy/MBq, median dose: 0.0071–0.0099 mGy/MBq) and three acquisitions at 30, 60, and 90 min p.i. (mean dose: 0.0107–0.0212 mGy/MBq, median dose: 0.0103–0.0216 mGy/MBq). This was expected since the spleen is a fundamentally vascular organ and, consequently, does not show a permanent accumulation of the radiopharmaceutical over time as the remaining organs. There are two possible explanations for the fact that the radiopharmaceutical uptake was higher at 30 min p.i., compared to 60 and 90 min p.i. Either the radiopharmaceutical counts in the spleen peaked during the vascular phase at 30

minutes and then decreased, or the counts accumulated up to 30 minutes, and then an organic retention plateau was reached.

The mean absorbed doses in the liver and red bone marrow were lower in patient 1, compared to the other five patients. Since this patient has no clinical history to justify these results, such dissimilarity may be due to the fact that the administered radiation activity to this patient (87.69 MBq) was lower than the activities administered to the remaining subjects, which varied within the range of 109.15 MBq to 181.30 MBq. Other explanations for the low absorbed dose values in the liver are related to liver failure and deficiencies in the liver blood flow (whether provided by the hepatic artery or portal venous blood), which decrease the uptake of the radiopharmaceutical by the liver and the percentage of radioactive activity reaching this organ, respectively.

As already mentioned, patient 3 had two image acquisitions at different times, separated by an interval of 37 minutes. His high absorbed dose in the kidneys, compared to the dose in the same organ in the remaining patients, may be due to differences in the urine excretory pattern during those 37 minutes.

Earlier studies [57-61] have also observed that the kidneys are the organs obtaining the highest mean and median absorbed doses. However, the absorbed dose values in the kidneys found in this study (mean: 0.0561 mGy/MBq, median: 0.0499 mGy/MBq) are not in line with the estimations by Afshar-Oromieh et al. [57] (mean: 0.2620 mGy/MBq, median: 0.2925 mGy/MBq), Pfob et al. [58] (mean: 0.1220 mGy/MBq, median: 0.1210 mGy/MBq), Green et al. [59] (mean: 0.4130 mGy/MBq), Demirci et al. [60] (mean: 0.2460 mGy/MBq) and Sandgren et al. [61] (median: 0.2400 mGy/MBq). In fact, the mean and median dose values in the kidneys presented the highest variability ($Range_{Mean}$=0.0561–0.4130 mGy/MBq, $Range_{Median}$=0.0499–0.2925 mGy/MBq), demonstrating the discrepancy of results that exist in the literature and in the present study for this organ. Comparing the results of this study with the literature, the deviations were high and ranged from -53.3% (E_{RMean}, Pfob et al. [58]) to -86.3% (E_{RMean}, Green et al. [59]). No correlation between the obtained results and the renal function of each patient was attempted. It is known that renal function can vary significantly from patient to patient and even more when dealing with primary prostatic disease. The length of disease duration may also play an important role.

The liver dose values were the closest to those in the literature. The absorbed doses in the liver obtained in this study (mean: 0.0132 mGy/MBq, median: 0.0126 mGy/MBq) are in agreement with the results by Afshar-Oromieh et al. [57] (mean: 0.0309 mGy/MBq, median: 0.0305 mGy/MBq), Pfob et al. [58] (mean: 0.0214 mGy/MBq, median: 0.0207 mGy/MBq), Green et al. [59] (mean: 0.0395 mGy/MBq), Demirci et al. [60] (mean: 0.0294 mGy/MBq) and Sandgren et al. [61] (median: 0.0530 mGy/MBq). The ranges of mean and median absorbed dose values were 0.0132–0.0395 mGy/MBq and 0.0126–0.0530 mGy/MBq, respectively, and the maximum and

minimum deviation values were -77.4% ($E_{RMedian}$, Sandgren et al. [61]) and -38.1% (E_{RMean}, Pfob et al. [58]), respectively.

The spleen results were similar to the liver results already discussed. However, there was an increase in the variability of the absorbed dose values ($Range_{Mean}$=0.0114–0.0581 mGy/MBq, $Range_{Median}$=0.0102–0.0460 mGy/MBq) and in the maximum and minimum deviations (-81.0% (E_{RMean}, Green et al. [59]) and -71.8% (E_{RMean}, Demirci et al. [60]).

As in this study, the literature also reports the red bone marrow as the organ with the lowest mean and median absorbed doses. The dosimetry results in the red bone marrow present the lowest variability, compared to the values in the other three organs ($Range_{Mean}$=0.0015–0.0139 mGy/MBq, $Range_{Median}$=0.0013–0.0150 mGy/MBq). However, in this organ, there is a higher deviation of results between those obtained in this study and those in the literature, reaching a deviation of -91.3% ($E_{RMedian}$, Sandgren et al. [61]) in one of the cases.

There is a tremendous variability of the absorbed dose per organ, per patient, and per author. This variability can be explained by several factors. First, previous studies employed compartment or organ dosimetry methods, which consider a uniform biodistribution of the radiopharmaceutical. Afshar-Oromieh et al. [57], Pfob et al. [58], Green et al. [59], and Demirci et al. [60] used the software OLINDA/EXM for the calculations, whereas Sandgren et al. [61] utilized the software IDAC-Dose 2.1. In another way, the present study employed a voxel-based approach, which leads to dosimetry estimations closer to the real ones since it considers a non-uniform biodistribution. In addition, Pfob et al. [58] employed the PET/MRI imaging technique in their study. These differences resulting from the varied applied methodologies lead to uncertainties of a systematic nature. Second, this study was based on two or three image acquisitions per patient, while Green et al. [59] studied three acquisitions per patient, Pfob et al. [58] and Sandgren et al. [61] four acquisitions, and Demirci et al. [60] five acquisitions per patient. Knowing that multiple acquisitions better mimic the biopharmaceuticals and pharmacokinetics of radiopharmaceuticals, the variability in the number of images per patient also leads to differences in the obtained results. Third, other explanations will most likely be related to multiple variables, such as the patient's intrinsic radiopharmaceutical pharmacokinetics, malfunction of the organs, administered activity, and excretion pathways. The pharmacokinetics of the radiopharmaceutical is dependent on the pharmacokinetics of the tracer and on the half-life of the radionuclide (physical, biological, and effective) and differs with the radiopharmaceutical, from patient to patient and from organ to organ. Variability of the absorbed doses may also be related to the existence of organs that did not perform their expected function at the time of image acquisition. Furthermore, the administered activity differs from patient to patient, and it may not be the same as the activity measured in the syringe before the procedure. In this regard, it is usually assumed that all the activity

measured in the syringe is injected into the vein and not outside. Additionally, it is also assumed that the residue in the syringe is similar at all times. However, this may not happen and consequently can affect the dosimetry calculations. Finally, there are different excretion pathways of the radiopharmaceutical, such as renal and hepatobiliary, which can influence the dose results, especially in the kidneys. Fourth, it is also important to realize that unavoidable inter-scanner variability may also lead to differences in the absorbed dose calculation studies since it makes comparing, exchanging, and combining results more challenging.

6.2 Conclusions

^{68}Ga-PSMA-11 is currently the most commonly used PSMA-targeting agent under investigation due to its high expression in prostate cancer cell lines as well as its potential prognostic value in patients with prostate cancer [28]. However, knowledge of the clinical safety and whole-body radiation dosimetry of this agent is crucial for its adoption in clinical institutions. In this study, it was found that ^{68}Ga-PSMA-11 was safe and well tolerated and that no pharmacological side effects were observed in a limited number of patients after its intravenous injection. The absorbed dose values obtained in the present study yield less radiation exposure compared to other studies (although comparisons between different works that employed different methodologies are limited), which is an additional argument in favor of the use of ^{68}Ga-PSMA-11 for human imaging in clinical practice.

6.3 Limitations

This study faced some limitations that could lead to differences between the absorbed dose obtained in the present work and in the literature. First, since a time-consuming imaging protocol is needed for dosimetry calculations, only a limited number of six patients could be included, and the patient population was rather heterogeneous. Second, only two or three image acquisitions were performed, respectively, for the first and second subsets of patients. Consequently, the patients' kinetics were not fully captured, resulting in a less accurate dosimetry. Third, the S-values used in dose calculation in this study were neither organ- nor patient-specific. Fourth, the data present in this retrospective study, obtained with a PET scanner combined with a low-dose CT, were compared with previous studies that employed other imaging modalities, such as PET/MRI and other dosimetry calculation approaches.

6.4 Future work

For future perspectives, there are several projects that can be conducted. A good starting point would be to obtain patient- and organ-specific S-values, taking into account Monte Carlo simulations based on CT images of each patient, instead of merely considering the standard tissue composition. Furthermore, regarding the paired organs, it is also important to highlight the need to quantify the absorbed dose in each organ individually. For example, for the kidneys, it would be interesting to calculate the absorbed dose in the two independent kidneys and in their junctions with the excretory system. Then, the incorporation of a technology in the image reconstruction equipment, which would calculate the patients' absorbed dose distributions, would be an advantage in NM clinics.

The study of the cumulative absorbed dose of patients submitted to multiple exposures during their lifetime is one of the main projects to consider in the future. In fact, cumulative radiation exposure from multiple radiological procedures may put some individuals at significantly higher risk of stochastic and deterministic effects. Thus it is very important to follow the history of radiological exposure of individuals, including the dose per examination and the number of examinations. However, no country currently has a radiation dose tracking program at the national level to track medical radiation procedures, although efforts have been made by several organizations [135]. In fact, IAEA is working to include dose information in Electronic Health Records (EHRs) [104].

Patient dose information is found in the form of structured dose reports as standardized by the Integrated Health Enterprise (IHE) [136]. These data are typically found on the DICOM header of the patient's image files that are usually available on Picture Archiving and Communication System (PACS) servers [137]. Interoperability of several health information systems is the goal, and in some imaging modalities, dose tracking is currently possible. However, it is lacking for NM procedures. While in CT, standard reference quantities such as dose length product (DLP) or volume computed tomography dose index **(**CTDIvol) are sufficient to estimate organ absorbed dose, in NM, the reference dose quantity (activity) alone is of lesser value [138]. Doses are dependent on the type of the radiopharmaceutical used, the quantity of administered activity, and the patient-specific biokinetics of uptake and clearance from each organ. Moreover, patient radiation exposure begins prior to and continues beyond the imaging time.

Model-derived dose coefficients can be used to estimate radiation doses from NM procedures. Such dose coefficients, which can be found in ICRP Publication 17 [139] and ICRP Publication 53 [140] for a variety of radiopharmaceuticals, can be multiplied by the administered

activity in order to provide estimates of organ doses. However, while activity- and radiopharmaceutical-specific, these estimates cannot reflect the biokinetics and habitus of patients.

As future work, a possible solution is to build a dosimetry model that incorporates not only activity and radiopharmaceutical information but also measures of patient-specific biokinetics and functional parameters of different organs. It would be a personalized medicine model in which the specific biodistribution of radiopharmaceuticals, the anatomical constitution of patients, and the functioning of organs would be called into question. The main objective would be to model the biokinetic behavior of radiopharmaceuticals in multiple subjects and extrapolate the absorbed dose distribution from the administered activity in each patient. Additionally, and if there is a relation in the way different organs react to radiation, a secondary model for obtaining dose in an organ from the dose information of another organ would be another important point in these futuristic dosimetry studies. First, the same quantity of radiopharmaceutical would have to be injected in several patients. The sample of patients would have to differ in age and index body mass in order to study the influence of body habitus in dose calculation. Also, extensive scanning for each patient would be required, from the moment of injection of the radiopharmaceutical until the moment the radiopharmaceutical is completely excreted, which depends on its effective half-life. Further, and since the volume of some organs, such as the bladder, changes over time, CT images would only be acquired in the first and last acquisitions, and virtual CTs would be reconstructed for all other PET image acquisition moments. After the construction of the model, tests using images of new patients would have to be performed to analyze its effectiveness in personalized medicine studies. This model has not yet been created since it is quite challenging to find patients who are willing to undergo several exams spaced in time, in addition to the fact that this whole process would be expensive for research institutions.

Bibliography

[1] J. F. Eary, "Nuclear medicine in cancer diagnosis," (in eng), *Lancet,* vol. 354, no. 9181, pp. 853-7, Sep 4 1999, doi: 10.1016/s0140-6736(99)80041-5.

[2] S. S. Anand, H. Singh, and A. K. Dash, "Clinical Applications of PET and PET-CT," (in eng), *Med J Armed Forces India,* vol. 65, no. 4, pp. 353-8, Oct 2009, doi: 10.1016/s0377-1237(09)80099-3.

[3] S. Zang *et al.*, "68Ga-PSMA-11 PET/CT for prostate cancer staging and risk stratification in Chinese patients," (in eng), *Oncotarget,* vol. 8, no. 7, pp. 12247-12258, Feb 14 2017, doi: 10.18632/oncotarget.14691.

[4] I. Rausch, A. Ruiz, I. Valverde-Pascual, J. Cal-Gonzalez, T. Beyer, and I. Carrio, "Performance Evaluation of the Vereos PET/CT System According to the NEMA NU2-2012 Standard," *J Nucl Med,* vol. 60, no. 4, pp. 561-567, Apr 2019, doi: 10.2967/jnumed.118.215541.

[5] W. B. Li, W. Hofmann, and W. Friedland, "Microdosimetry and nanodosimetry for internal emitters," *Radiation Measurements,* vol. 115, pp. 29-29-42, 2018-08-01 2018, doi: 10.1016/j.radmeas.2018.05.013.

[6] W. R. Hendee and F. M. Edwards, "ALARA and an integrated approach to radiation protection," *Semin Nucl Med,* vol. 16, no. 2, pp. 142-50, Apr 1986, doi: 10.1016/s0001-2998(86)80027-7.

[7] C. C. O. Silva *et al.*, "Preclinical radiation internal dosimetry in the development of new radiopharmaceuticals using GATE Monte Carlo simulation," *Radiation Physics and Chemistry,* vol. 173, 2020, doi: 10.1016/j.radphyschem.2020.108879.

[8] T. Beyer, G. Antoch, A. Bockisch, and J. Stattaus, "Optimized intravenous contrast administration for diagnostic whole-body 18F-FDG PET/CT," (in eng), *J Nucl Med,* vol. 46, no. 3, pp. 429-35, Mar 2005.

[9] T. Beyer *et al.*, "Acquisition protocol considerations for combined PET/CT imaging," (in eng), *J Nucl Med,* vol. 45 Suppl 1, pp. 25s-35s, Jan 2004.

[10] G. J. Kelloff *et al.*, "Progress and promise of FDG-PET imaging for cancer patient management and oncologic drug development," (in eng), *Clin Cancer Res,* vol. 11, no. 8, pp. 2785-808, Apr 15 2005, doi: 10.1158/1078-0432.Ccr-04-2626.

[11] E. M. Rohren, T. G. Turkington, and R. E. Coleman, "Clinical applications of PET in oncology," (in eng), *Radiology,* vol. 231, no. 2, pp. 305-32, May 2004, doi: 10.1148/radiol.2312021185.

[12] H. Tan *et al.*, "Total-Body PET/CT: Current Applications and Future Perspectives," (in eng), *AJR Am J Roentgenol,* vol. 215, no. 2, pp. 325-337, Aug 2020, doi: 10.2214/ajr.19.22705.

[13] L. F. de Geus-Oei, H. F. van der Heijden, F. H. Corstens, and W. J. Oyen, "Predictive and prognostic value of FDG-PET in nonsmall-cell lung cancer: a systematic review," *Cancer,* vol. 110, no. 8, pp. 1654-64, Oct 15 2007, doi: 10.1002/cncr.22979.

[14] B. A. Siegel and F. Dehdashti, "Oncologic PET/CT: current status and controversies," *Eur Radiol,* vol. 15 Suppl 4, pp. D127-32, Nov 2005, doi: 10.1007/s10406-005-0116-7.

[15] H. Schöder, Y. E. Erdi, S. M. Larson, and H. W. Yeung, "PET/CT: a new imaging technology in nuclear medicine," (in eng), *Eur J Nucl Med Mol Imaging,* vol. 30, no. 10, pp. 1419-37, Oct 2003, doi: 10.1007/s00259-003-1299-6.

[16] D. A. Silver, I. Pellicer, W. R. Fair, W. D. Heston, and C. Cordon-Cardo, "Prostate-specific membrane antigen expression in normal and malignant human tissues," (in eng), *Clin Cancer Res,* vol. 3, no. 1, pp. 81-5, Jan 1997.

[17] R. Bar-Shalom *et al.*, "Clinical performance of PET/CT in evaluation of cancer: additional value for diagnostic imaging and patient management," (in eng), *J Nucl Med,* vol. 44, no. 8, pp. 1200-9, Aug 2003.

[18] L. K. Griffeth, "Use of PET/CT scanning in cancer patients: technical and practical considerations," (in eng), *Proc (Bayl Univ Med Cent),* vol. 18, no. 4, pp. 321-30, Oct 2005, doi: 10.1080/08998280.2005.11928089.

[19] C. Degenhardt *et al.*, "The digital Silicon Photomultiplier — A novel sensor for the detection of scintillation light," in *2009 IEEE Nuclear Science Symposium Conference Record (NSS/MIC)*, 24 Oct.-1 Nov. 2009 2009, pp. 2383-2386, doi: 10.1109/NSSMIC.2009.5402190.

[20] N. C. Nguyen *et al.*, "Image Quality and Diagnostic Performance of a Digital PET Prototype in Patients with Oncologic Diseases: Initial Experience and Comparison with Analog PET," *J Nucl Med*, vol. 56, no. 9, pp. 1378-85, Sep 2015, doi: 10.2967/jnumed.114.148338.

[21] T. Frach, G. Prescher, C. Degenhardt, R. d. Gruyter, A. Schmitz, and R. Ballizany, "The digital silicon photomultiplier — Principle of operation and intrinsic detector performance," in *2009 IEEE Nuclear Science Symposium Conference Record (NSS/MIC)*, 24 Oct.-1 Nov. 2009 2009, pp. 1959-1965, doi: 10.1109/NSSMIC.2009.5402143.

[22] C. Degenhardt *et al.*, "Performance evaluation of a prototype Positron Emission Tomography scanner using Digital Photon Counters (DPC)," in *2012 IEEE Nuclear Science Symposium and Medical Imaging Conference Record (NSS/MIC)*, 27 Oct.-3 Nov. 2012 2012, pp. 2820-2824, doi: 10.1109/NSSMIC.2012.6551643.

[23] I. Velikyan, "Prospective of (68)Ga Radionuclide Contribution to the Development of Imaging Agents for Infection and Inflammation," *Contrast Media Mol Imaging*, vol. 2018, p. 9713691, 2018, doi: 10.1155/2018/9713691.

[24] M. Eder *et al.*, "68Ga-complex lipophilicity and the targeting property of a urea-based PSMA inhibitor for PET imaging," *Bioconjug Chem,* vol. 23, no. 4, pp. 688-97, Apr 18 2012, doi: 10.1021/bc200279b.

[25] A. Joshi, C. Nicholson, H. Rhee, S. Gustafson, K. Miles, and I. Vela, "Incidental Malignancies Identified During Staging for Prostate Cancer With (68)Ga Prostate-specific Membrane Antigen HBED-CC Positron Emission Tomography Imaging," *Urology,* vol. 104, pp. e3-e4, Jun 2017, doi: 10.1016/j.urology.2017.03.018.

[26] D. G. Bostwick, A. Pacelli, M. Blute, P. Roche, and G. P. Murphy, "Prostate specific membrane antigen expression in prostatic intraepithelial neoplasia and adenocarcinoma: a study of 184 cases," (in eng), *Cancer,* vol. 82, no. 11, pp. 2256-61, Jun 1 1998, doi: 10.1002/(sici)1097-0142(19980601)82:11<2256::aid-cncr22>3.0.co;2-s.

[27] S. Mannweiler, P. Amersdorfer, S. Trajanoski, J. A. Terrett, D. King, and G. Mehes, "Heterogeneity of prostate-specific membrane antigen (PSMA) expression in prostate carcinoma with distant metastasis," (in eng), *Pathol Oncol Res,* vol. 15, no. 2, pp. 167-72, Jun 2009, doi: 10.1007/s12253-008-9104-2.

[28] S. R. Banerjee *et al.*, "68Ga-labeled inhibitors of prostate-specific membrane antigen (PSMA) for imaging prostate cancer," (in eng), *J Med Chem,* vol. 53, no. 14, pp. 5333-41, Jul 22 2010, doi: 10.1021/jm100623e.

[29] A. X. Zhang *et al.*, "A remote arene-binding site on prostate specific membrane antigen revealed by antibody-recruiting small molecules," (in eng), *J Am Chem Soc,* vol. 132, no. 36, pp. 12711-6, Sep 15 2010, doi: 10.1021/ja104591m.

[30] T. Maurer, M. Eiber, M. Schwaiger, and J. E. Gschwend, "Current use of PSMA-PET in prostate cancer management," (in eng), *Nat Rev Urol,* vol. 13, no. 4, pp. 226-35, Apr 2016, doi: 10.1038/nrurol.2016.26.

[31] J. S. Ross *et al.*, "Correlation of primary tumor prostate-specific membrane antigen expression with disease recurrence in prostate cancer," (in eng), *Clin Cancer Res,* vol. 9, no. 17, pp. 6357-62, Dec 15 2003.

[32] A. Afshar-Oromieh *et al.*, "PET imaging with a [68Ga]gallium-labelled PSMA ligand for the diagnosis of prostate cancer: biodistribution in humans and first evaluation of tumour lesions," (in eng), *Eur J Nucl Med Mol Imaging,* vol. 40, no. 4, pp. 486-95, Apr 2013, doi: 10.1007/s00259-012-2298-2.

[33] A. Barakat, B. Yacoub, M. E. Homsi, A. Saad Aldine, A. El Hajj, and M. B. Haidar, "Role of Early PET/CT Imaging with 68Ga-PSMA in Staging and Restaging of Prostate Cancer," (in eng), *Sci Rep,* vol. 10, no. 1, p. 2705, Feb 17 2020, doi: 10.1038/s41598-020-59296-6.

[34] T. A. Hope, J. Z. Goodman, I. E. Allen, J. Calais, W. P. Fendler, and P. R. Carroll, "Metaanalysis of (68)Ga-PSMA-11 PET Accuracy for the Detection of Prostate Cancer Validated by Histopathology," (in eng), *J Nucl Med,* vol. 60, no. 6, pp. 786-793, Jun 2019, doi: 10.2967/jnumed.118.219501.

[35] C. Sachpekidis *et al.*, "(68)Ga-PSMA PET/CT in the evaluation of bone metastases in prostate cancer," (in eng), *Eur J Nucl Med Mol Imaging,* vol. 45, no. 6, pp. 904-912, Jun 2018, doi: 10.1007/s00259-018-3936-0.

[36] M. Eiber *et al.*, "Simultaneous (68)Ga-PSMA HBED-CC PET/MRI Improves the Localization of Primary Prostate Cancer," (in eng), *Eur Urol,* vol. 70, no. 5, pp. 829-836, Nov 2016, doi: 10.1016/j.eururo.2015.12.053.

[37] F. L. Giesel *et al.*, "Intra-individual comparison of (68)Ga-PSMA-11-PET/CT and multi-parametric MR for imaging of primary prostate cancer," (in eng), *Eur J Nucl Med Mol Imaging,* vol. 43, no. 8, pp. 1400-6, Jul 2016, doi: 10.1007/s00259-016-3346-0.

[38] P. J. Roach *et al.*, "The Impact of (68)Ga-PSMA PET/CT on Management Intent in Prostate Cancer: Results of an Australian Prospective Multicenter Study," (in eng), *J Nucl Med,* vol. 59, no. 1, pp. 82-88, Jan 2018, doi: 10.2967/jnumed.117.197160.

[39] A. Herlemann *et al.*, "(68)Ga-PSMA Positron Emission Tomography/Computed Tomography Provides Accurate Staging of Lymph Node Regions Prior to Lymph Node Dissection in Patients with Prostate Cancer," (in eng), *Eur Urol,* vol. 70, no. 4, pp. 553-557, Oct 2016, doi: 10.1016/j.eururo.2015.12.051.

[40] I. Virgolini, C. Decristoforo, A. Haug, S. Fanti, and C. Uprimny, "Current status of theranostics in prostate cancer," (in eng), *Eur J Nucl Med Mol Imaging,* vol. 45, no. 3, pp. 471-495, Mar 2018, doi: 10.1007/s00259-017-3882-2.

[41] M. Perera *et al.*, "Sensitivity, Specificity, and Predictors of Positive (68)Ga-Prostate-specific Membrane Antigen Positron Emission Tomography in Advanced Prostate Cancer: A Systematic Review and Meta-analysis," (in eng), *Eur Urol,* vol. 70, no. 6, pp. 926-937, Dec 2016, doi: 10.1016/j.eururo.2016.06.021.

[42] N. S. Schmidt-Hegemann *et al.*, "Impact of (68)Ga-PSMA PET/CT on the Radiotherapeutic Approach to Prostate Cancer in Comparison to CT: A Retrospective Analysis," (in eng), *J Nucl Med,* vol. 60, no. 7, pp. 963-970, Jul 2019, doi: 10.2967/jnumed.118.220855.

[43] P. J. van Leeuwen *et al.*, "(68) Ga-PSMA has a high detection rate of prostate cancer recurrence outside the prostatic fossa in patients being considered for salvage radiation treatment," (in eng), *BJU Int,* vol. 117, no. 5, pp. 732-9, May 2016, doi: 10.1111/bju.13397.

[44] T. Pyka *et al.*, "Comparison of bone scintigraphy and (68)Ga-PSMA PET for skeletal staging in prostate cancer," (in eng), *Eur J Nucl Med Mol Imaging,* vol. 43, no. 12, pp. 2114-2121, Nov 2016, doi: 10.1007/s00259-016-3435-0.

[45] L. Thomas, C. Balmus, H. Ahmadzadehfar, M. Essler, H. Strunk, and R. Bundschuh, "Assessment of Bone Metastases in Patients with Prostate Cancer—A Comparison between 99mTc-Bone-Scintigraphy and [68Ga]Ga-PSMA PET/CT," *Pharmaceuticals,* vol. 10, p. 68, 07/31 2017, doi: 10.3390/ph10030068.

[46] B. Grubmuller *et al.*, "(68)Ga-PSMA 11 ligand PET imaging in patients with biochemical recurrence after radical prostatectomy - diagnostic performance and impact on therapeutic decision-making," *Eur J Nucl Med Mol Imaging,* vol. 45, no. 2, pp. 235-242, Feb 2018, doi: 10.1007/s00259-017-3858-2.

[47] A. Ribeiro *et al.*, "Ionising radiation exposure from medical imaging - A review of Patient's (un) awareness," (in eng), *Radiography (Lond),* vol. 26, no. 2, pp. e25-e30, May 2020, doi: 10.1016/j.radi.2019.10.002.

[48] S. G. Cho, J. Kim, and H. C. Song, "Radiation Safety in Nuclear Medicine Procedures," (in eng), *Nucl Med Mol Imaging,* vol. 51, no. 1, pp. 11-16, Mar 2017, doi: 10.1007/s13139-016-0406-0.

[49] E. S. Amis, Jr. *et al.*, "American College of Radiology white paper on radiation dose in medicine," (in eng), *J Am Coll Radiol,* vol. 4, no. 5, pp. 272-84, May 2007, doi: 10.1016/j.jacr.2007.03.002.

[50] E. E. Kim, "Radiology for PET/CT Reporting," *J Nucl Med,* vol. 56, no. 1, p. 162, Jan 2015, doi: 10.2967/jnumed.114.148692.

[51] M. A. Hoffmann, H. J. Wieler, C. Baues, N. J. Kuntz, I. Richardsen, and M. Schreckenberger, "The Impact of 68Ga-PSMA PET/CT and PET/MRI on the Management of Prostate Cancer," *Urology,* vol. 130, pp. 1-12, Aug 2019, doi: 10.1016/j.urology.2019.04.004.

[52] R. Clarke, F. Fry, J. Stather, and G. Webb, "1990 recommendations of the International Commission on Radiological Protection," *Documents of the NRPB,* vol. 4, no. 1, pp. 1-5, 1993.

[53] J. Vennart, "The 1990 recommendations of the International Commission on Radiological Protection," *Journal of Radiological Protection,* vol. 11, p. 199, 07/20 2000, doi: 10.1088/0952-4746/11/3/006.

[54] M. Charles, "ICRP Publication 103: Recommendations of the ICRP," *Ann ICRP,* vol. 37, 10/19 2007, doi: 10.1093/rpd/ncn187.

[55] W. Hendee *et al.*, "Report of a consultation on justification of patient exposures in medical imaging," *Radiation protection dosimetry,* vol. 135, pp. 137-44, 02/01 2009, doi: 10.1093/rpd/ncp107.

[56] R. Loevinger and M. Berman, "A formalism for calculation of absorbed dose from radionuclides," *Phys Med Biol,* vol. 13, no. 2, pp. 205-17, Apr 1968, doi: 10.1088/0031-9155/13/2/306.

[57] A. Afshar-Oromieh *et al.*, "Radiation dosimetry of (68)Ga-PSMA-11 (HBED-CC) and preliminary evaluation of optimal imaging timing," (in eng), *Eur J Nucl Med Mol Imaging,* vol. 43, no. 9, pp. 1611-20, Aug 2016, doi: 10.1007/s00259-016-3419-0.

[58] C. H. Pfob *et al.*, "Biodistribution and radiation dosimetry of (68)Ga-PSMA HBED CC-a PSMA specific probe for PET imaging of prostate cancer," (in eng), *Eur J Nucl Med Mol Imaging,* vol. 43, no. 11, pp. 1962-70, Oct 2016, doi: 10.1007/s00259-016-3424-3.

[59] M. A. Green *et al.*, "Estimation of radiation dosimetry for (68)Ga-HBED-CC (PSMA-11) in patients with suspected recurrence of prostate cancer,"

(in eng), *Nucl Med Biol,* vol. 46, pp. 32-35, Mar 2017, doi: 10.1016/j.nucmedbio.2016.11.002.

[60] E. Demirci *et al.*, "ESTIMATION OF THE ORGAN ABSORBED DOSES AND EFFECTIVE DOSE FROM 68Ga-PSMA-11 PET SCAN," (in eng), *Radiat Prot Dosimetry,* vol. 182, no. 4, pp. 518-524, Dec 1 2018, doi: 10.1093/rpd/ncy111.

[61] K. Sandgren *et al.*, "Radiation dosimetry of [(68)Ga]PSMA-11 in low-risk prostate cancer patients," (in eng), *EJNMMI Phys,* vol. 6, no. 1, p. 2, Jan 11 2019, doi: 10.1186/s40658-018-0239-2.

[62] T. Leong *et al.*, "A prospective study to evaluate the impact of FDG-PET on CT-based radiotherapy treatment planning for oesophageal cancer," (in eng), *Radiother Oncol,* vol. 78, no. 3, pp. 254-61, Mar 2006, doi: 10.1016/j.radonc.2006.02.014.

[63] M. MacManus, R. Hicks, M. Bayne, T. Leong, L. Peters, and D. Ball, "In regard to Paulino and Johnstone: Use of PET and CT imaging data in radiation therapy planning. Int J Radit Oncol Biol Phys 2004;59:4-5," (in eng), *Int J Radiat Oncol Biol Phys,* vol. 60, no. 3, pp. 1005-6; author reply 1006, Nov 1 2004, doi: 10.1016/j.ijrobp.2004.07.667.

[64] H. Necib *et al.*, "Detection and characterization of tumor changes in 18F-FDG PET patient monitoring using parametric imaging," *J Nucl Med,* vol. 52, no. 3, pp. 354-61, Mar 2011, doi: 10.2967/jnumed.110.080150.

[65] R. Fonti, M. Conson, and S. Del Vecchio, "PET/CT in radiation oncology," (in eng), *Semin Oncol,* vol. 46, no. 3, pp. 202-209, Jun 2019, doi: 10.1053/j.seminoncol.2019.07.001.

[66] J. A. Seibert, "X-ray imaging physics for nuclear medicine technologists. Part 1: Basic principles of x-ray production," *Journal of nuclear medicine technology,* vol. 32, no. 3, pp. 139-147, 2004.

[67] M. M. Lell, J. E. Wildberger, H. Alkadhi, J. Damilakis, and M. Kachelriess, "Evolution in Computed Tomography: The Battle for Speed and Dose," *Invest Radiol,* vol. 50, no. 9, pp. 629-44, Sep 2015, doi: 10.1097/RLI.0000000000000172.

[68] J. A. Seibert and J. M. Boone, "X-ray imaging physics for nuclear medicine technologists. Part 2: X-ray interactions and image formation," (in eng), *J Nucl Med Technol,* vol. 33, no. 1, pp. 3-18, Mar 2005.

[69] J. E. Turner, "Interaction of ionizing radiation with matter," (in eng), *Health Phys,* vol. 88, no. 6, pp. 520-44, Jun 2005, doi: 10.1097/00004032-200506000-00002.

[70] E. Berg and S. R. Cherry, "Innovations in Instrumentation for Positron Emission Tomography," (in eng), *Semin Nucl Med,* vol. 48, no. 4, pp. 311-331, Jul 2018, doi: 10.1053/j.semnuclmed.2018.02.006.

[71] E. Seeram, "Computed Tomography: Physical Principles and Recent Technical Advances," (in eng), *J Med Imaging Radiat Sci,* vol. 41, no. 2, pp. 87-109, Jun 2010, doi: 10.1016/j.jmir.2010.04.001.

[72] R. E. Kravetz, "X-ray tube," (in eng), *Am J Gastroenterol,* vol. 96, no. 4, p. 1273, Apr 2001, doi: 10.1111/j.1572-0241.2001.03762.x.

[73] K. Lameka, M. D. Farwell, and M. Ichise, "Positron Emission Tomography," (in eng), *Handb Clin Neurol,* vol. 135, pp. 209-227, 2016, doi: 10.1016/b978-0-444-53485-9.00011-8.

[74] C.-H. Yeong, M. Cheng, and N. Kh, "Therapeutic radionuclides in nuclear medicine: Current and future prospects," *Journal of Zhejiang University. Science. B,* vol. 15, pp. 845-63, 10/01 2014, doi: 10.1631/jzus.B1400131.

[75] M. W. Groch, "Radioactive decay," (in eng), *Radiographics,* vol. 18, no. 5, pp. 1247-56; quiz 1245-6, Sep-Oct 1998, doi: 10.1148/radiographics.18.5.9747617.

[76] B. N. Ganguly, N. N. Mondal, M. Nandy, and F. Roesch, "Some physical aspects of positron annihilation tomography: A critical review," *Journal of Radioanalytical and Nuclear Chemistry,* vol. 279, no. 2, pp. 685-698, 2009, doi: 10.1007/s10967-007-7256-2.

[77] T. Pan and O. Mawlawi, "PET/CT in radiation oncology," (in eng), *Med Phys,* vol. 35, no. 11, pp. 4955-66, Nov 2008, doi: 10.1118/1.2986145.

[78] E. Garcia-Torano, V. Peyres Medina, E. Romero, and M. Roteta, "Measurement of the half-life of (6)(8)Ga," *Appl Radiat Isot,* vol. 87, pp. 122-5, May 2014, doi: 10.1016/j.apradiso.2013.11.082.

[79] S. R. Banerjee and M. G. Pomper, "Clinical applications of Gallium-68," *Appl Radiat Isot,* vol. 76, pp. 2-13, Jun 2013, doi: 10.1016/j.apradiso.2013.01.039.

[80] R. A. Werner *et al.*, "(18)F-Labeled, PSMA-Targeted Radiotracers: Leveraging the Advantages of Radiofluorination for Prostate Cancer Molecular Imaging," *Theranostics,* vol. 10, no. 1, pp. 1-16, 2020, doi: 10.7150/thno.37894.

[81] N. K. Kuzmenko, "Updated decay data evaluation for (68)Ga," *Appl Radiat Isot,* vol. 152, pp. 188-192, Oct 2019, doi: 10.1016/j.apradiso.2019.07.008.

[82] D. S. O'Keefe, D. J. Bacich, S. S. Huang, and W. D. W. Heston, "A Perspective on the Evolving Story of PSMA Biology, PSMA-Based Imaging, and Endoradiotherapeutic Strategies," *J Nucl Med,* vol. 59, no. 7, pp. 1007-1013, Jul 2018, doi: 10.2967/jnumed.117.203877.

[83] E. Gourni and G. Henriksen, "Metal-Based PSMA Radioligands," *Molecules,* vol. 22, no. 4, Mar 24 2017, doi: 10.3390/molecules22040523.

[84] D. G. Bostwick, J. Ma, J. Qian, D. Josefson, and L. Liu, "Immunohistology of the Prostate, Bladder, Testis and Kidney," *Diagnostic Immunohistochemistry: Second Edition,* pp. 509-610, 01/01 2006, doi: 10.1016/B978-0-443-06652-8.50020-X.

[85] A. M. Boustani, D. Pucar, and L. Saperstein, "Molecular imaging of prostate cancer," *Br J Radiol,* vol. 91, no. 1084, p. 20170736, Apr 2018, doi: 10.1259/bjr.20170736.

[86] Z. Keidar *et al.*, "68Ga-PSMA PET/CT in prostate cancer patients - patterns of disease, benign findings and pitfalls," *Cancer Imaging,* vol. 18, no. 1, p. 39, Nov 1 2018, doi: 10.1186/s40644-018-0175-3.

[87] N. P. Lenzo, D. Meyrick, and J. H. Turner, "Review of Gallium-68 PSMA PET/CT Imaging in the Management of Prostate Cancer," *Diagnostics (Basel),* vol. 8, no. 1, Feb 11 2018, doi: 10.3390/diagnostics8010016.

[88] M. Conti, "State of the art and challenges of time-of-flight PET," *Phys Med,* vol. 25, no. 1, pp. 1-11, Mar 2009, doi: 10.1016/j.ejmp.2008.10.001.

[89] R. Ganai, S. Mehta, M. Shiroya, M. Mondal, Z. Ahammed, and S. Chattopadhyay, "A Proof-of-Principle for Time of Flight-Positron Emission Tomography Imaging," in *XXII DAE High Energy Physics Symposium*, 2018: Springer, pp. 125-128.

[90] C. Burger, G. Goerres, S. Schoenes, A. Buck, A. H. Lonn, and G. K. Von Schulthess, "PET attenuation coefficients from CT images: experimental evaluation of the transformation of CT into PET 511-keV attenuation coefficients," (in eng), *Eur J Nucl Med Mol Imaging,* vol. 29, no. 7, pp. 922-7, Jul 2002, doi: 10.1007/s00259-002-0796-3.

[91] M. Unterrainer *et al.*, "Recent advances of PET imaging in clinical radiation oncology," *Radiat Oncol,* vol. 15, no. 1, p. 88, Apr 21 2020, doi: 10.1186/s13014-020-01519-1.

[92] J. L. Humm, A. Rosenfeld, and A. Del Guerra, "From PET detectors to PET scanners," *Eur J Nucl Med Mol Imaging,* vol. 30, no. 11, pp. 1574-97, Nov 2003, doi: 10.1007/s00259-003-1266-2.

[93] S. T. Lee and A. M. Scott, "Nuclear medicine in the era of personalised medicine," (in eng), *Intern Med J,* vol. 48, no. 5, pp. 497-499, May 2018, doi: 10.1111/imj.13789.

[94] C. J. Marriott, J. E. Cadorette, R. Lecomte, V. Scasnar, J. Rousseau, and J. E. van Lier, "High-resolution PET imaging and quantitation of pharmaceutical biodistributions in a small animal using avalanche photodiode detectors," (in eng), *J Nucl Med,* vol. 35, no. 8, pp. 1390-6, Aug 1994.

[95] L. Jødal, C. Le Loirec, and C. Champion, "Positron range in PET imaging: an alternative approach for assessing and correcting the blurring," (in eng), *Phys Med Biol,* vol. 57, no. 12, pp. 3931-43, Jun 21 2012, doi: 10.1088/0031-9155/57/12/3931.

[96] G. Tarantola, F. Zito, and P. Gerundini, "PET instrumentation and reconstruction algorithms in whole-body applications," (in eng), *J Nucl Med,* vol. 44, no. 5, pp. 756-69, May 2003.

[97] E. Burgio, P. Piscitelli, and L. Migliore, "Ionizing Radiation and Human Health: Reviewing Models of Exposure and Mechanisms of Cellular Damage. An Epigenetic Perspective," (in eng), *Int J Environ Res Public Health,* vol. 15, no. 9, Sep 10 2018, doi: 10.3390/ijerph15091971.

[98] H. Stadtmann, "Dose quantities in radiation protection and dosemeter calibration," (in eng), *Radiat Prot Dosimetry,* vol. 96, no. 1-3, pp. 21-6, 2001, doi: 10.1093/oxfordjournals.rpd.a006584.

[99] J. A. Siegel *et al.*, "MIRD pamphlet no. 16: techniques for quantitative radiopharmaceutical biodistribution data acquisition and analysis for use in human radiation dose estimates," *Journal of Nuclear Medicine,* vol. 40, no. 2, pp. 37S-61S, 1999.

[100] A. Allisy, W. A. Jennings, A. M. Kellerer, and J. W. Müller, "Report 51," *Journal of the International Commission on Radiation Units and Measurements,* vol. os26, no. 2, pp. NP-NP, 2016, doi: 10.1093/jicru/os26.2.Report51.

[101] A. J. Einstein, K. W. Moser, R. C. Thompson, M. D. Cerqueira, and M. J. Henzlova, "Radiation dose to patients from cardiac diagnostic imaging," *Circulation,* vol. 116, no. 11, pp. 1290-305, Sep 11 2007, doi: 10.1161/CIRCULATIONAHA.107.688101.

[102] W. E. Bolch, K. F. Eckerman, G. Sgouros, and S. R. Thomas, "MIRD pamphlet No. 21: a generalized schema for radiopharmaceutical dosimetry--standardization of nomenclature," (in eng), *J Nucl Med,* vol. 50, no. 3, pp. 477-84, Mar 2009, doi: 10.2967/jnumed.108.056036.

[103] D. R. Fisher and F. H. Fahey, "Appropriate Use of Effective Dose in Radiation Protection and Risk Assessment," (in eng), *Health Phys,* vol. 113, no. 2, pp. 102-109, Aug 2017, doi: 10.1097/hp.0000000000000674.

[104] O. Holmberg, J. Malone, M. Rehani, D. McLean, and R. Czarwinski, "Current issues and actions in radiation protection of patients," *Eur J Radiol,* vol. 76, no. 1, pp. 15-9, Oct 2010, doi: 10.1016/j.ejrad.2010.06.033.

[105] W. E. Bolch *et al.*, "MIRD pamphlet No. 17: the dosimetry of nonuniform activity distributions--radionuclide S values at the voxel level. Medical Internal Radiation Dose Committee," (in eng), *J Nucl Med,* vol. 40, no. 1, pp. 11s-36s, Jan 1999.

[106] M. S. Lee *et al.*, "Whole-Body Voxel-Based Personalized Dosimetry: The Multiple Voxel S-Value Approach for Heterogeneous Media with Nonuniform Activity Distributions," *J Nucl Med,* vol. 59, no. 7, pp. 1133-1139, Jul 2018, doi: 10.2967/jnumed.117.201095.

[107] P. Perez and M. Valente, "DOSIS: An integrated computational tool for patient-specific dosimetry in nuclear medicine by Monte Carlo and dose point kernel approaches," *Appl Radiat Isot,* vol. 150, pp. 135-140, Aug 2019, doi: 10.1016/j.apradiso.2019.05.031.

[108] M. G. Stabin, "Radiopharmaceuticals for nuclear cardiology: radiation dosimetry, uncertainties, and risk," (in eng), *J Nucl Med,* vol. 49, no. 9, pp. 1555-63, Sep 2008, doi: 10.2967/jnumed.108.052241.

[109] L. G. Bouchet *et al.*, "MIRD Pamphlet No 19: absorbed fractions and radionuclide S values for six age-dependent multiregion models of the kidney," (in eng), *J Nucl Med,* vol. 44, no. 7, pp. 1113-47, Jul 2003.

[110] N. Lanconelli *et al.*, "A free database of radionuclide voxel S values for the dosimetry of nonuniform activity distributions," (in eng), *Phys Med Biol,* vol. 57, no. 2, pp. 517-33, Jan 21 2012, doi: 10.1088/0031-9155/57/2/517.

[111] R. E. Toohey, M. G. Stabin, and E. E. Watson, "The AAPM/RSNA physics tutorial for residents: internal radiation dosimetry: principles and applications," (in eng), *Radiographics,* vol. 20, no. 2, pp. 533-46; quiz 531-2, Mar-Apr 2000, doi: 10.1148/radiographics.20.2.g00mc33533.

[112] R. Thompson, "RadOnc: An R Package for Analysis of Dose-Volume Histogram and Three-Dimensional Structural Data," *Journal Of Radiation Oncology Informatics,* vol. 6, pp. 98-110, 01/01 2014, doi: 10.5166/jroi-6-1-25.

[113] B. A. Faddegon, I. Kawrakow, Y. Kubyshin, J. Perl, J. Sempau, and L. Urban, "The accuracy of EGSnrc, Geant4 and PENELOPE Monte Carlo systems for the simulation of electron scatter in external beam radiotherapy," (in eng), *Phys Med Biol,* vol. 54, no. 20, pp. 6151-63, Oct 21 2009, doi: 10.1088/0031-9155/54/20/008.

[114] H. Yoriyaz, M. G. Stabin, and A. dos Santos, "Monte Carlo MCNP-4B-based absorbed dose distribution estimates for patient-specific dosimetry," (in eng), *J Nucl Med,* vol. 42, no. 4, pp. 662-9, Apr 2001.

[115] T. Goorley *et al.*, "Initial MCNP6 release overview. MCNP6 version 0.1," *Nuclear technology,* vol. 180, pp. 298-315, 12/01 2012, doi: 10.13182/NT11-135.

[116] D. R. White, J. Booz, R. V. Griffith, J. J. Spokas, and I. J. Wilson, "Report 44," *Journal of the International Commission on Radiation Units and Measurements,* vol. os23, no. 1, pp. NP-NP, 2016, doi: 10.1093/jicru/os23.1.Report44.

[117] S. Di Maria, A. Belchior, Y. Romanets, A. Paulo, and P. Vaz, "Monte Carlo dose distribution calculation at nuclear level for Auger-emitting radionuclide energies," (in eng), *Appl Radiat Isot,* vol. 135, pp. 72-77, May 2018, doi: 10.1016/j.apradiso.2018.01.013.

[118] K. Eckerman and A. Endo, "ICRP Publication 107. Nuclear decay data for dosimetric calculations," (in eng), *Ann ICRP,* vol. 38, no. 3, pp. 7-96, 2008, doi: 10.1016/j.icrp.2008.10.004.

[119] A. Belchior, S. Di Maria, C. Fernandes, P. Vaz, A. Paulo, and P. Raposinho, "Radiobiological and dosimetric assessment of DNA-intercalated (99m)Tc-complexes bearing acridine orange derivatives," (in eng), *EJNMMI Res,* vol. 10, no. 1, p. 79, Jul 13 2020, doi: 10.1186/s13550-020-00663-9.

[120] T. S. Lawrence, R. J. Tesser, and R. K. ten Haken, "An application of dose volume histograms to the treatment of intrahepatic malignancies with radiation therapy," (in eng), *Int J Radiat Oncol Biol Phys,* vol. 19, no. 4, pp. 1041-7, Oct 1990, doi: 10.1016/0360-3016(90)90031-e.

[121] F. Van den Heuvela, "Decomposition analysis of differential dose volume histograms," (in eng), *Med Phys,* vol. 33, no. 2, pp. 297-307, Feb 2006, doi: 10.1118/1.2147742.

[122] R. Nanabala, M. K. Anees, A. Sasikumar, A. Joy, and M. R. Pillai, "Preparation of [(68)Ga]PSMA-11 for PET-CT imaging using a manual synthesis module and organic matrix based (68)Ge/(68)Ga generator," (in eng), *Nucl Med Biol,* vol. 43, no. 8, pp. 463-9, Aug 2016, doi: 10.1016/j.nucmedbio.2016.05.006.

[123] K. Zhernosekov *et al.*, "Processing of Generator-Produced 68Ga for Medical Application," *Journal of nuclear medicine : official publication, Society of Nuclear Medicine,* vol. 48, pp. 1741-8, 10/01 2007, doi: 10.2967/jnumed.107.040378.

[124] A. Amor-Coarasa, M. Schoendorf, M. Meckel, S. Vallabhajosula, and J. W. Babich, "Comprehensive Quality Control of the ITG 68Ge/68Ga Generator and Synthesis of 68Ga-DOTATOC and 68Ga-PSMA-HBED-CC

for Clinical Imaging," (in eng), *J Nucl Med,* vol. 57, no. 9, pp. 1402-5, Sep 2016, doi: 10.2967/jnumed.115.171249.

[125] W. P. Fendler *et al.*, "(68)Ga-PSMA PET/CT: Joint EANM and SNMMI procedure guideline for prostate cancer imaging: version 1.0," (in eng), *Eur J Nucl Med Mol Imaging,* vol. 44, no. 6, pp. 1014-1024, Jun 2017, doi: 10.1007/s00259-017-3670-z.

[126] I. Rauscher, T. Maurer, W. P. Fendler, W. H. Sommer, M. Schwaiger, and M. Eiber, "(68)Ga-PSMA ligand PET/CT in patients with prostate cancer: How we review and report," (in eng), *Cancer Imaging,* vol. 16, no. 1, p. 14, Jun 8 2016, doi: 10.1186/s40644-016-0072-6.

[127] A. Fedorov *et al.*, "3D Slicer as an image computing platform for the Quantitative Imaging Network," *Magn Reson Imaging,* vol. 30, no. 9, pp. 1323-41, Nov 2012, doi: 10.1016/j.mri.2012.05.001.

[128] G. C. Sieck, "Physiology in Perspective: Anatomy and Physiology-Structure and Function in Biology," (in eng), *Physiology (Bethesda),* vol. 34, no. 6, pp. 379-380, Nov 1 2019, doi: 10.1152/physiol.00029.2019.

[129] P. F. Caracappa, T. C. E. Chao, and X. G. Xu, "A study of predicted bone marrow distribution on calculated marrow dose from external radiation exposures using two sets of image data for the same individual," (in eng), *Health Phys,* vol. 96, no. 6, pp. 661-674, 2009, doi: 10.1097/01.HP.0000346304.45813.36.

[130] J. A. Hayman *et al.*, "Distribution of proliferating bone marrow in adult cancer patients determined using FLT-PET imaging," *Int J Radiat Oncol Biol Phys,* vol. 79, no. 3, pp. 847-52, Mar 1 2011, doi: 10.1016/j.ijrobp.2009.11.040.

[131] T. M. Lehmann, C. Gönner, and K. Spitzer, "Survey: interpolation methods in medical image processing," (in eng), *IEEE Trans Med Imaging,* vol. 18, no. 11, pp. 1049-75, Nov 1999, doi: 10.1109/42.816070.

[132] E. A. Sobie, "An introduction to MATLAB," (in eng), *Sci Signal,* vol. 4, no. 191, p. tr7, Sep 13 2011, doi: 10.1126/scisignal.2001984.

[133] H. Xie, H. Yao, X. Sun, S. Zhou, and X. Tong, "Weighted Voxel: a novel voxel representation for 3D reconstruction," in *Proceedings of the 10th International Conference on Internet Multimedia Computing and Service*, 2018, pp. 1-4.

[134] C. Pinter, A. Lasso, A. Wang, D. Jaffray, and G. Fichtinger, "SlicerRT: radiation therapy research toolkit for 3D Slicer," *Med Phys,* vol. 39, no. 10, pp. 6332-8, Oct 2012, doi: 10.1118/1.4754659.

[135] M. M. Rehani, D. P. Frush, T. Berris, and A. J. Einstein, "Patient radiation exposure tracking: worldwide programs and needs--results from the first IAEA survey," *Eur J Radiol,* vol. 81, no. 10, pp. e968-76, Oct 2012, doi: 10.1016/j.ejrad.2012.07.004.

[136] K. O'Donnell, "Radiation exposure monitoring: a new IHE profile," (in eng), *Pediatr Radiol,* vol. 41, no. 5, pp. 588-91, May 2011, doi: 10.1007/s00247-010-1903-4.

[137] M. Mercuri, M. M. Rehani, and A. J. Einstein, "Tracking patient radiation exposure: challenges to integrating nuclear medicine with other modalities," *J Nucl Cardiol*, vol. 19, no. 5, pp. 895-900, Oct 2012, doi: 10.1007/s12350-012-9586-x.

[138] M. M. Rehani, "Patient radiation exposure and dose tracking: a perspective," *J Med Imaging (Bellingham)*, vol. 4, no. 3, p. 031206, Jul 2017, doi: 10.1117/1.JMI.4.3.031206.

[139] ICRP, "Protection of the Patients in Radionuclide Investigations," *Annals of the ICRP/ICRP Publication*, vol. 9, pp. i-27, 1965/09/17/ 1965, doi: 10.1016/S0074-2740(65)80004-6.

[140] Icrp, "Radiation dose to patients from radiopharmaceuticals. Addendum 3 to ICRP Publication 53. ICRP Publication 106. Approved by the Commission in October 2007," (in eng), *Ann ICRP*, vol. 38, no. 1-2, pp. 1-197, 2008, doi: 10.1016/j.icrp.2008.08.003.

A

Appendix 1 – S-values

Throughout the appendix, scientific notation was adopted when the absolute value of the results or uncertainties was close to zero.

A radial comparison between the results obtained by the MCNP6.1 and EGSnrc programs was performed to validate the S-values presented by the MCNP6.1 software. The S-values for the radionuclide ^{90}Y and soft tissue, considering its beta decay component, for voxels of 2.21 mm and 4.42 mm are presented in tables A.1 and A.2, respectively.

Table A.1: S-values for the ^{90}Y radionuclide, 2.21 mm voxels, and soft tissue, obtained by the EGSnrc and MCNP6.1 Monte Carlo programs. Since this was a radial comparison, only the *k*-index related to each voxel's spatial position was altered.

i	***j***	***k***	**S-value (EGSnrc)**	**S-value (MCNP6.1)**
0	0	0	3	$3.1 \pm 1.2 \times 10^{-4}$
0	0	1	0.57	$0.55 \pm 9.9 \times 10^{-4}$
0	0	2	0.07	$0.073 \pm 3.8 \times 10^{-4}$
0	0	3	0.01	$0.011 \pm 1.4 \times 10^{-4}$
0	0	4	7.52×10^{-4}	$0.0011 \pm 4.3 \times 10^{-5}$
0	0	5	1.25×10^{-5}	$2.6 \times 10^{-5} \pm 5.5 \times 10^{-6}$

Table A.2: S-values for the ^{90}Y radionuclide, 4.42 mm voxels, and soft tissue, obtained by the EGSnrc and MCNP6.1 Monte Carlo programs. Since this was a radial comparison, only the *k*-index related to each voxel's spatial position was altered.

i	***j***	***k***	**S-value (EGSnrc)**	**S-value (MCNP6.1)**
0	0	0	0.69	$0.72 \pm 7.2 \times 10^{-4}$
0	0	1	0.09	$0.094 \pm 4.7 \times 10^{-4}$
0	0	2	0.002	$0.0025 \pm 7.1 \times 10^{-5}$
0	0	3	3.11×10^{-6}	$3.2 \times 10^{-6} \pm 1.5 \times 10^{-6}$
0	0	4	7.83×10^{-7}	$4.9 \times 10^{-7} \pm 2.6 \times 10^{-7}$
0	0	5	4.70×10^{-7}	$9.9 \times 10^{-7} \pm 5.1 \times 10^{-7}$

Tables A.3 and A.4 represent the S-values for the ^{68}Ga radionuclide, 4 mm voxels, and for the soft tissue and red bone marrow materials. These octants with dimension 4×4×4 are constituted by 64 elements and were obtained from a weighted sum of the S-values of the following radiations: beta-plus, Auger electrons, X-rays, and gamma rays. All rounded values were rounded by excess.

Table A.3: S-values for the ^{68}Ga radionuclide, cubical voxels of 4×4×4 mm^3, and soft tissue.

i	***j***	***k***	**S-value (mGy/MBq·s)**
0	0	0	$0.83 \pm 5.4 \times 10^{-5}$
0	0	1	0.11 ± 0.0078
0	0	2	0.0021 ± 0.0017
0	0	3	$2.8 \times 10^{-4} \pm 0.0087$
0	1	0	0.11 ± 0.0078
0	1	1	$0.026 \pm 4.7 \times 10^{-4}$
0	1	2	$9.6 \times 10^{-4} \pm 0.0025$
0	1	3	$2.5 \times 10^{-4} \pm 0.013$
0	2	0	0.0021 ± 0.0017
0	2	1	$9.6 \times 10^{-4} \pm 0.0025$
0	2	2	$3.2 \times 10^{-4} \pm 0.0062$
0	2	3	$1.9 \times 10^{-4} \pm 0.024$

0	3	0	$2.8\times10^{-4}\pm0.0089$
0	3	1	$2.5\times10^{-4}\pm0.010$
0	3	2	$1.9\times10^{-4}\pm0.020$
0	3	3	$1.4\times10^{-4}\pm0.064$
1	0	0	0.11 ± 0.0080
1	0	1	$0.026\pm4.7\times10^{-4}$
1	0	2	$9.6\times10^{-4}\pm0.0025$
1	0	3	$2.5\times10^{-4}\pm0.012$
1	1	0	$0.026\pm4.7\times10^{-4}$
1	1	1	$0.0075\pm9.0\times10^{-4}$
1	1	2	$5.6\times10^{-4}\pm0.0034$
1	1	3	$2.3\times10^{-4}\pm0.017$
1	2	0	$9.6\times10^{-4}\pm0.0025$
1	2	1	$5.6\times10^{-4}\pm0.0035$
1	2	2	$2.8\times10^{-4}\pm0.0083$
1	2	3	$1.8\times10^{-4}\pm0.026$
1	3	0	$2.5\times10^{-4}\pm0.013$
1	3	1	$2.3\times10^{-4}\pm0.014$
1	3	2	$1.8\times10^{-4}\pm0.024$
1	3	3	$1.3\times10^{-4}\pm0.091$
2	0	0	0.0021 ± 0.0017
2	0	1	$9.6\times10^{-4}\pm0.0025$
2	0	2	$3.2\times10^{-4}\pm0.0063$
2	0	3	$1.9\times10^{-4}\pm0.024$
2	1	0	$9.6\times10^{-4}\pm0.0025$
2	1	1	$5.6\times10^{-4}\pm0.0035$
2	1	2	$2.8\times10^{-4}\pm0.0087$
2	1	3	$1.8\times10^{-4}\pm0.034$

2	2	0	$3.2\times10^{-4}\pm0.0067$
2	2	1	$2.8\times10^{-4}\pm0.0086$
2	2	2	$2.1\times10^{-4}\pm0.015$
2	2	3	$1.5\times10^{-4}\pm0.041$
2	3	0	$1.9\times10^{-4}\pm0.020$
2	3	1	$1.8\times10^{-4}\pm0.026$
2	3	2	$1.5\times10^{-4}\pm0.046$
2	3	3	$1.1\times10^{-4}\pm0.053$
3	0	0	$2.8\times10^{-4}\pm0.0085$
3	0	1	$2.5\times10^{-4}\pm0.011$
3	0	2	$1.9\times10^{-4}\pm0.025$
3	0	3	$1.4\times10^{-4}\pm0.041$
3	1	0	$2.5\times10^{-4}\pm0.013$
3	1	1	$2.3\times10^{-4}\pm0.013$
3	1	2	$1.8\times10^{-4}\pm0.026$
3	1	3	$1.3\times10^{-4}\pm0.091$
3	2	0	$1.9\times10^{-4}\pm0.024$
3	2	1	$1.8\times10^{-4}\pm0.026$
3	2	2	$1.5\times10^{-4}\pm0.0053$
3	2	3	$1.1\times10^{-4}\pm0.091$
3	3	0	$1.4\times10^{-4}\pm0.053$
3	3	1	$1.3\times10^{-4}\pm0.091$
3	3	2	$1.1\times10^{-4}\pm0.064$
3	3	3	$8.8\times10^{-5}\pm0.064$

Table A.4: S-values for the ^{68}Ga radionuclide, cubical voxels of 4×4×4 mm^3, and red bone marrow.

i	***j***	***k***	**S-value (mGy/MBq·s)**
0	0	0	$0.82\pm5.8\times10^{-5}$
0	0	1	0.11 ± 0.0079

0	0	2	0.0019 ± 0.0014
0	0	3	$2.8\times10^{-4}\pm0.0053$
0	1	0	0.11 ± 0.0078
0	1	1	$0.025\pm4.4\times10^{-4}$
0	1	2	$8.7\times10^{-4}\pm0.0020$
0	1	3	$2.5\times10^{-4}\pm0.0070$
0	2	0	0.0019 ± 0.0014
0	2	1	$8.7\times10^{-4}\pm0.0020$
0	2	2	$3.2\times10^{-4}\pm0.0041$
0	2	3	$1.9\times10^{-4}\pm0.013$
0	3	0	$2.8\times10^{-4}\pm0.0055$
0	3	1	$2.5\times10^{-4}\pm0.0062$
0	3	2	$1.9\times10^{-4}\pm0.012$
0	3	3	$1.4\times10^{-4}\pm0.022$
1	0	0	0.11 ± 0.0080
1	0	1	$0.025\pm4.4\times10^{-4}$
1	0	2	$8.7\times10^{-4}\pm0.0020$
1	0	3	$2.5\times10^{-4}\pm0.0065$
1	1	0	$0.025\pm4.4\times10^{-4}$
1	1	1	$0.0070\pm8.2\times10^{-4}$
1	1	2	$5.4\times10^{-4}\pm0.0025$
1	1	3	$2.3\times10^{-4}\pm0.0080$
1	2	0	$8.7\times10^{-4}\pm0.0019$
1	2	1	$5.4\times10^{-4}\pm0.0025$
1	2	2	$2.8\times10^{-4}\pm0.0051$
1	2	3	$1.8\times10^{-4}\pm0.014$
1	3	0	$2.5\times10^{-4}\pm0.0066$
1	3	1	$2.3\times10^{-4}\pm0.0083$

1	3	2	$1.8\times10^{-4}\pm0.013$
1	3	3	$1.3\times10^{-4}\pm0.046$
2	0	0	0.0019 ± 0.0014
2	0	1	$8.7\times10^{-4}\pm0.0020$
2	0	2	$3.2\times10^{-4}\pm0.0041$
2	0	3	$1.9\times10^{-4}\pm0.011$
2	1	0	$8.7\times10^{-4}\pm0.0020$
2	1	1	$5.4\times10^{-4}\pm0.0025$
2	1	2	$2.8\times10^{-4}\pm0.0051$
2	1	3	$1.8\times10^{-4}\pm0.015$
2	2	0	$3.2\times10^{-4}\pm0.0042$
2	2	1	$2.8\times10^{-4}\pm0.0052$
2	2	2	$2.1\times10^{-4}\pm0.0094$
2	2	3	$1.5\times10^{-4}\pm0.029$
2	3	0	$1.9\times10^{-4}\pm0.011$
2	3	1	$1.8\times10^{-4}\pm0.014$
2	3	2	$1.5\times10^{-4}\pm0.023$
2	3	3	$1.1\times10^{-4}\pm0.037$
3	0	0	$2.8\times10^{-4}\pm0.0052$
3	0	1	$2.5\times10^{-4}\pm0.0065$
3	0	2	$1.9\times10^{-4}\pm0.013$
3	0	3	$1.4\times10^{-4}\pm0.023$
3	1	0	$2.5\times10^{-4}\pm0.0065$
3	1	1	$2.3\times10^{-4}\pm0.0082$
3	1	2	$1.8\times10^{-4}\pm0.015$
3	1	3	$1.3\times10^{-4}\pm0.035$
3	2	0	$1.9\times10^{-4}\pm0.012$
3	2	1	$1.8\times10^{-4}\pm0.015$

3	2	2	$1.5\times10^{-4}\pm0.025$
3	2	3	$1.1\times10^{-4}\pm0.064$
3	3	0	$1.4\times10^{-4}\pm0.032$
3	3	1	$1.3\times10^{-4}\pm0.037$
3	3	2	$1.1\times10^{-4}\pm0.091$
3	3	3	$9.3\times10^{-5}\pm0.091$

B

Appendix 2 – 3D absorbed dose distributions

Figures B.1 to B.24 represent the absorbed dose distributions in the kidneys, liver, spleen, and red bone marrow. In these figures, axial, coronal, and sagittal slices are presented, as well as 3D perspectives.

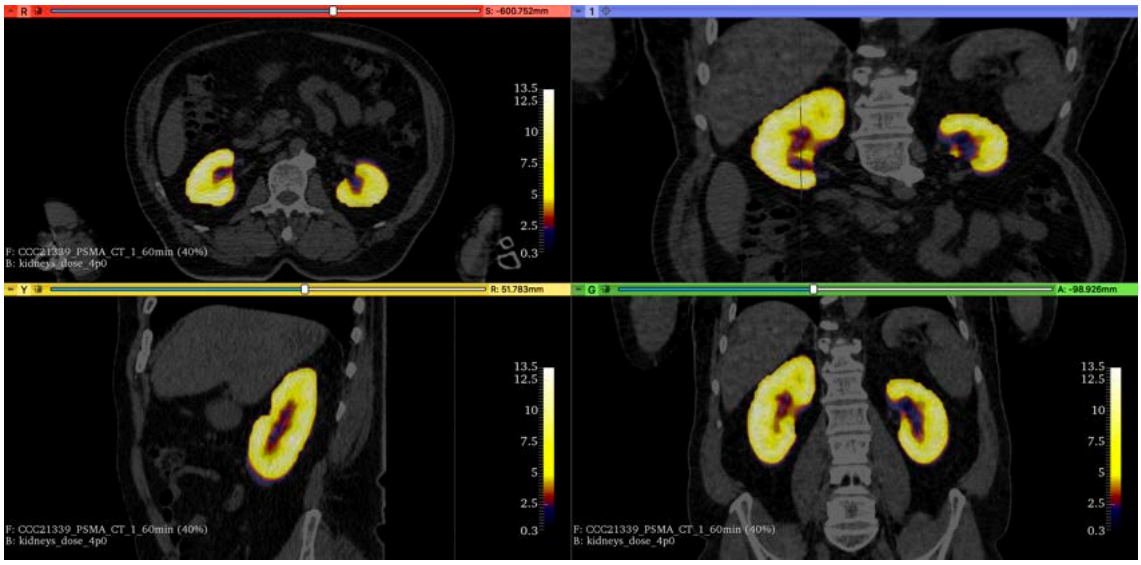

Figure B.1: Representative axial (R), coronal (G), and sagittal (Y) orthogonal slices as well as the 3D view (1) of the absorbed dose distribution in the kidneys of patient 1 in the 3D Slicer software. The scalar bar located on the right in the three images is expressed in mGy.

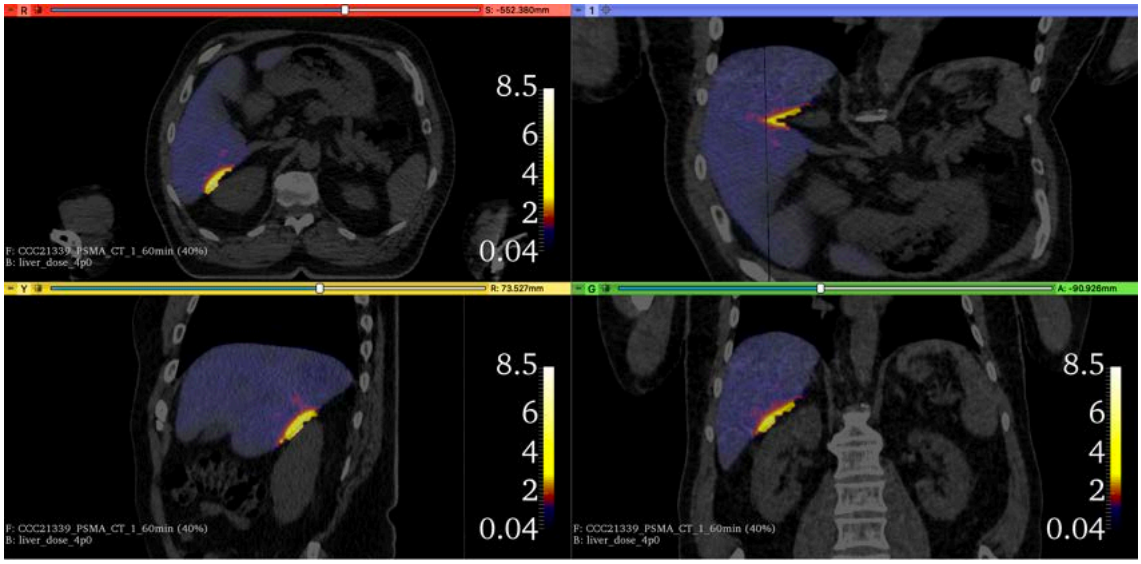

Figure B.2: Representative axial (R), coronal (G), and sagittal (Y) orthogonal slices as well as the 3D view (1) of the absorbed dose distribution in the liver of patient 1 in the 3D Slicer software. The scalar bar located on the right in the three images is expressed in mGy.

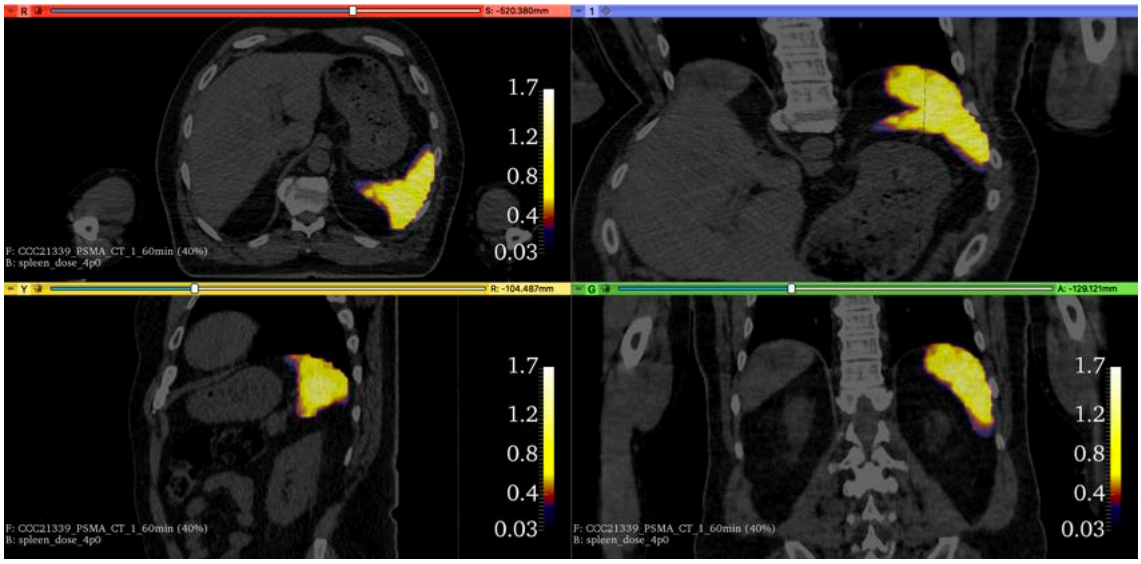

Figure B.3: Representative axial (R), coronal (G), and sagittal (Y) orthogonal slices as well as the 3D view (1) of the absorbed dose distribution in the spleen of patient 1 in the 3D Slicer software. The scalar bar located on the right in the three images is expressed in mGy.

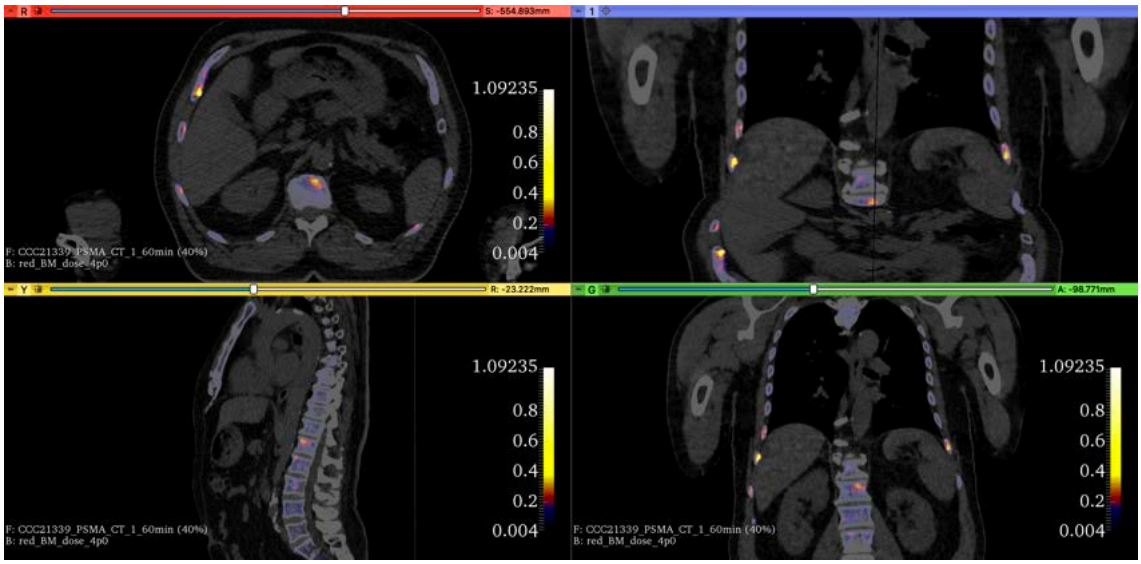

Figure B.4: Representative axial (R), coronal (G), and sagittal (Y) orthogonal slices as well as the 3D view (1) of the absorbed dose distribution in the red bone marrow of patient 1 in the 3D Slicer software. The scalar bar located on the right in the three images is expressed in mGy.

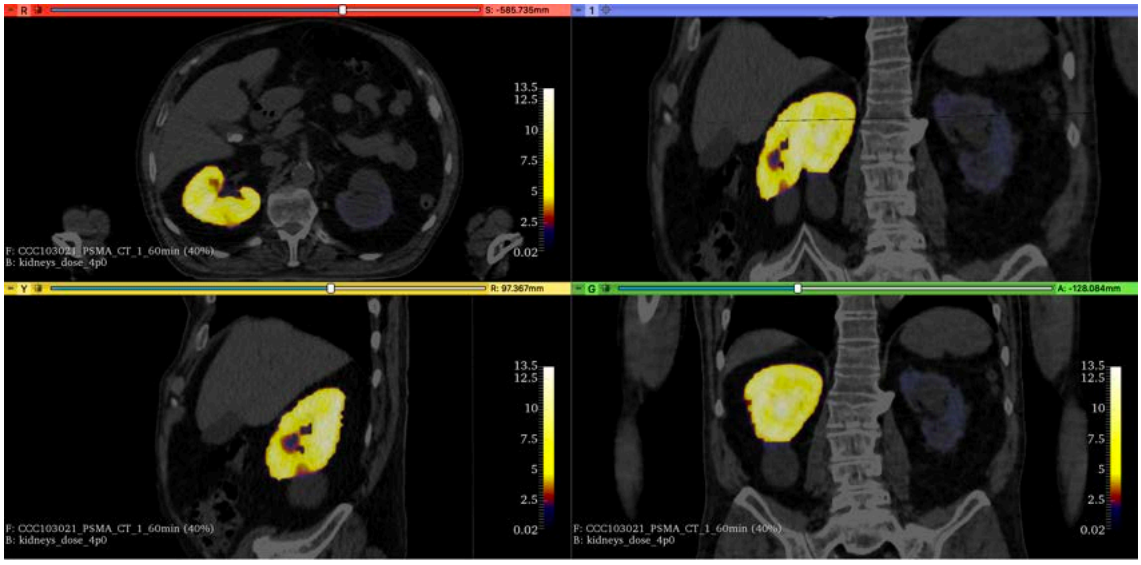

Figure B.5: Representative axial (R), coronal (G), and sagittal (Y) orthogonal slices as well as the 3D view (1) of the absorbed dose distribution in the kidneys of patient 2 in the 3D Slicer software. The scalar bar located on the right in the three images is expressed in mGy.

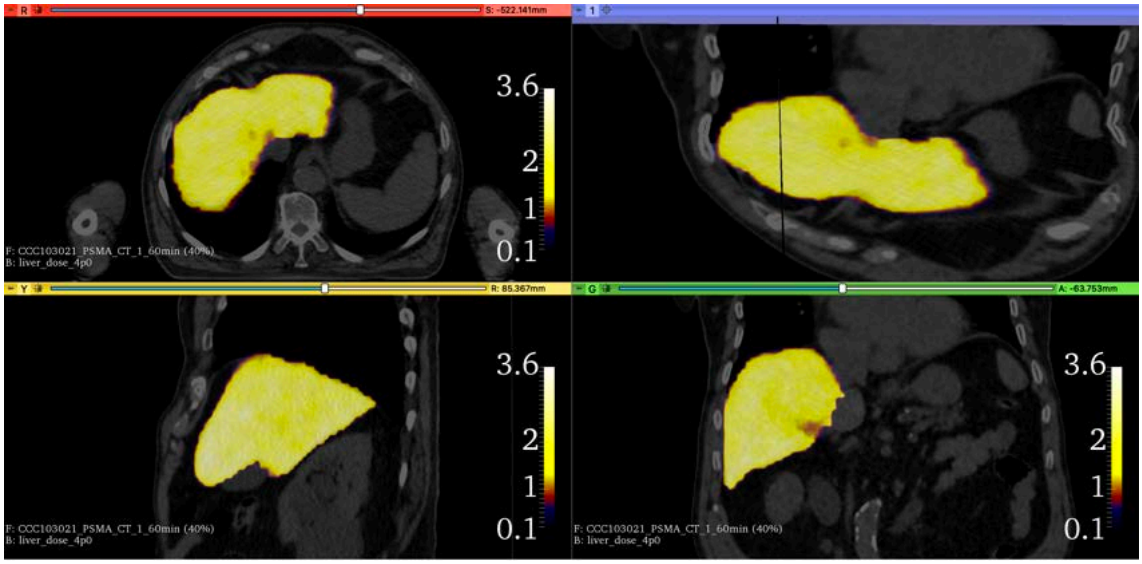

Figure B.6: Representative axial (R), coronal (G), and sagittal (Y) orthogonal slices as well as the 3D view (1) of the absorbed dose distribution in the liver of patient 2 in the 3D Slicer software. The scalar bar located on the right in the three images is expressed in mGy.

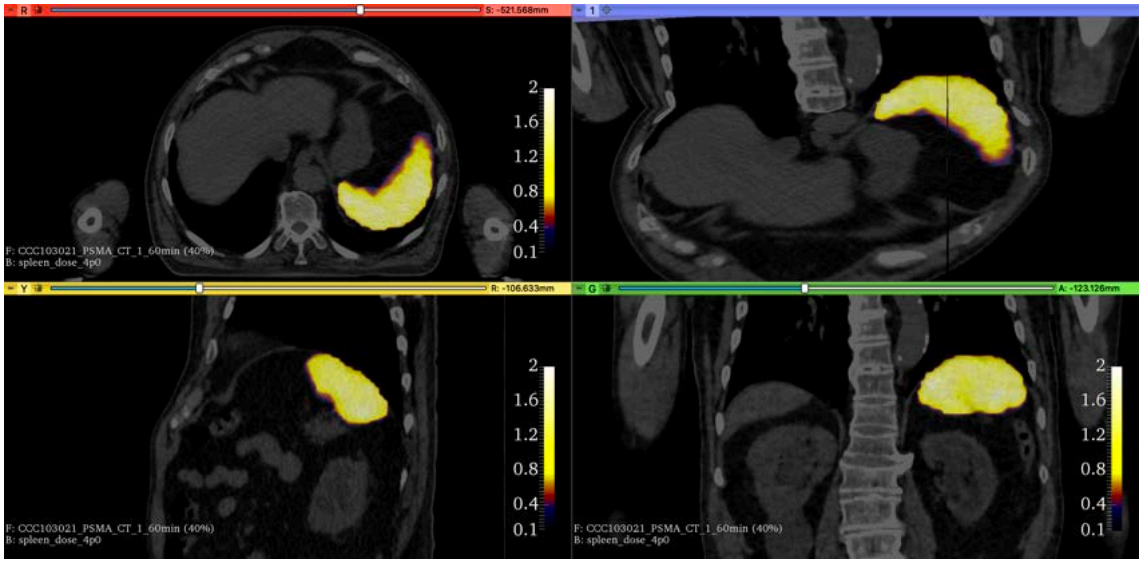

Figure B.7: Representative axial (R), coronal (G), and sagittal (Y) orthogonal slices as well as the 3D view (1) of the absorbed dose distribution in the spleen of patient 2 in the 3D Slicer software. The scalar bar located on the right in the three images is expressed in mGy.

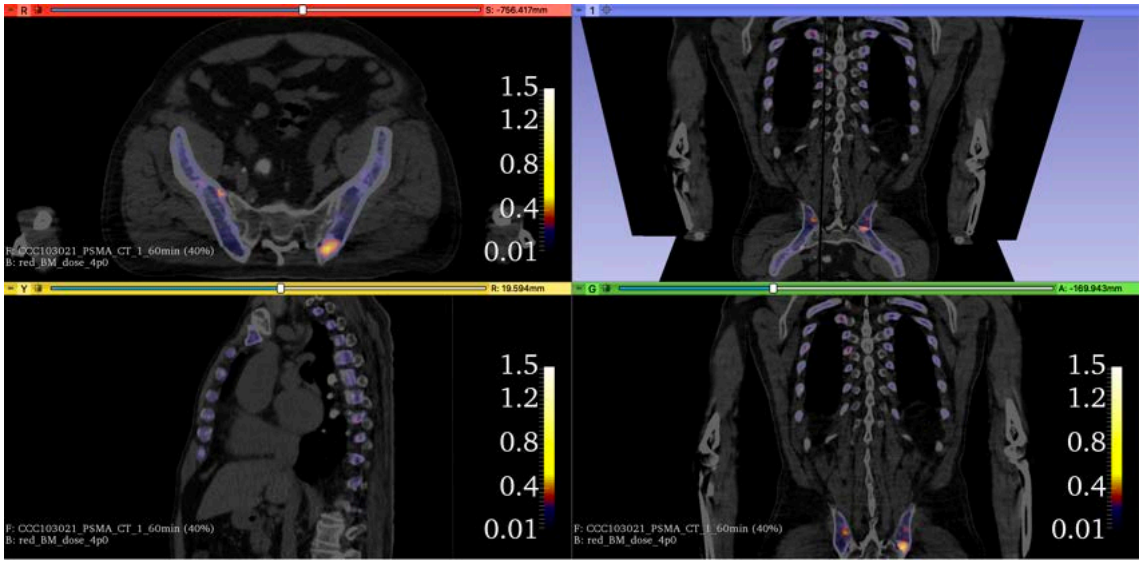

Figure B.8: Representative axial (R), coronal (G), and sagittal (Y) orthogonal slices as well as the 3D view (1) of the absorbed dose distribution in the red bone marrow of patient 2 in the 3D Slicer software. The scalar bar located on the right in the three images is expressed in mGy.

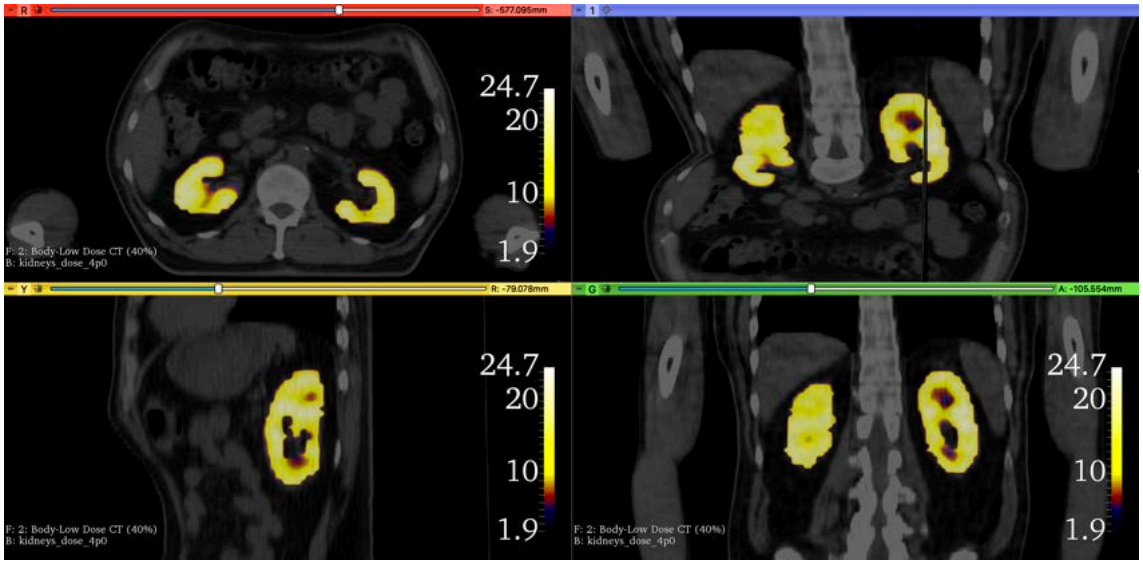

Figure B.9: Representative axial (R), coronal (G), and sagittal (Y) orthogonal slices as well as the 3D view (1) of the absorbed dose distribution in the kidneys of patient 3 in the 3D Slicer software. The scalar bar located on the right in the three images is expressed in mGy.

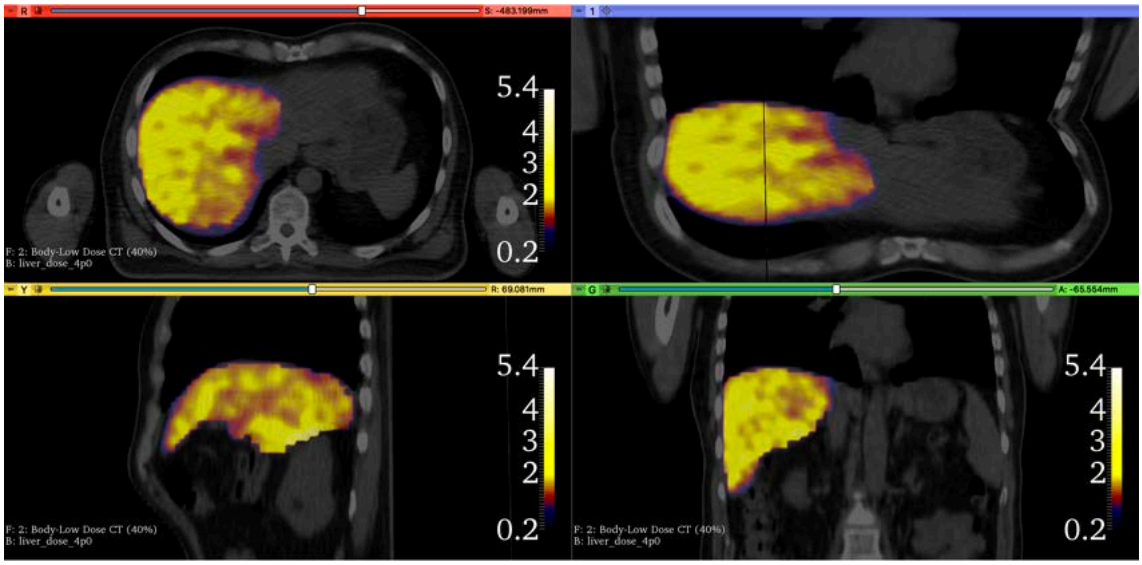

Figure B.10: Representative axial (R), coronal (G), and sagittal (Y) orthogonal slices as well as the 3D view (1) of the absorbed dose distribution in the liver of patient 3 in the 3D Slicer software. The scalar bar located on the right in the three images is expressed in mGy.

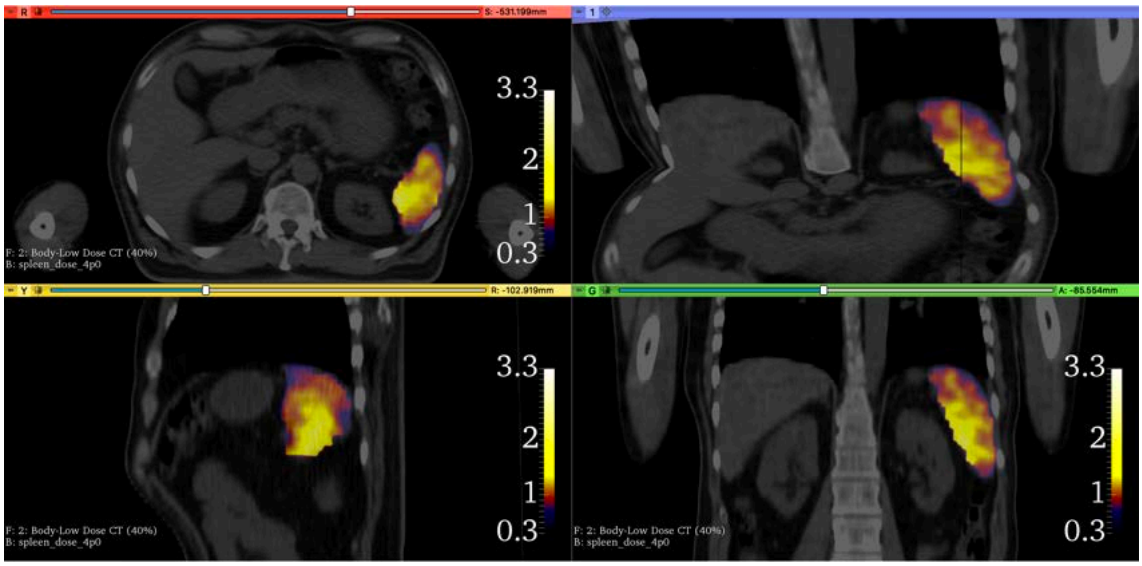

Figure B.11: Representative axial (R), coronal (G), and sagittal (Y) orthogonal slices as well as the 3D view (1) of the absorbed dose distribution in the spleen of patient 3 in the 3D Slicer software. The scalar bar located on the right in the three images is expressed in mGy.

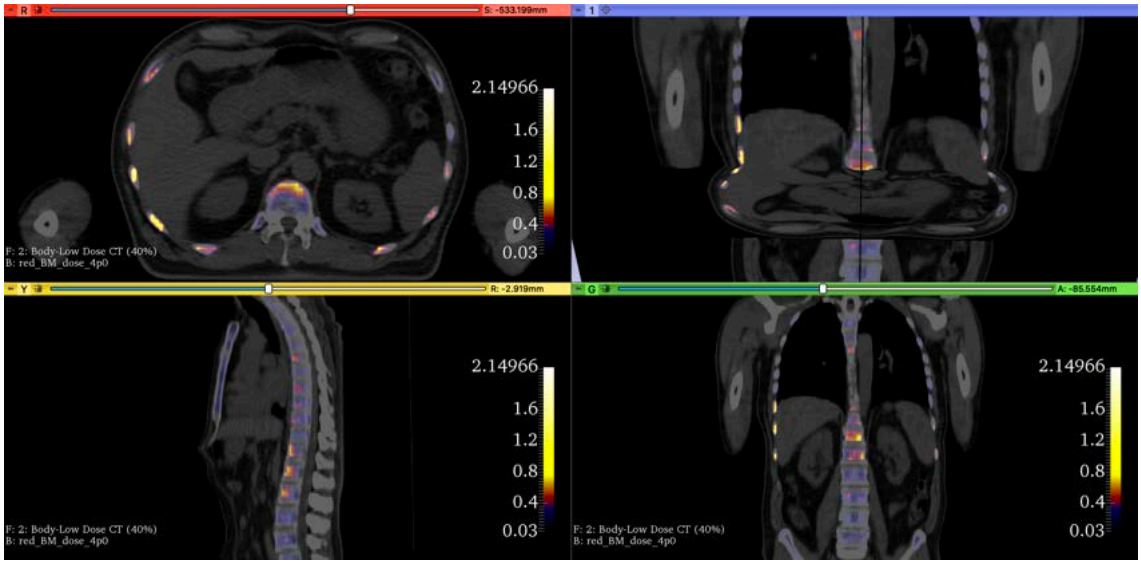

Figure B.12: Representative axial (R), coronal (G), and sagittal (Y) orthogonal slices as well as the 3D view (1) of the absorbed dose distribution in the red bone marrow of patient 3 in the 3D Slicer software. The scalar bar located on the right in the three images is expressed in mGy.

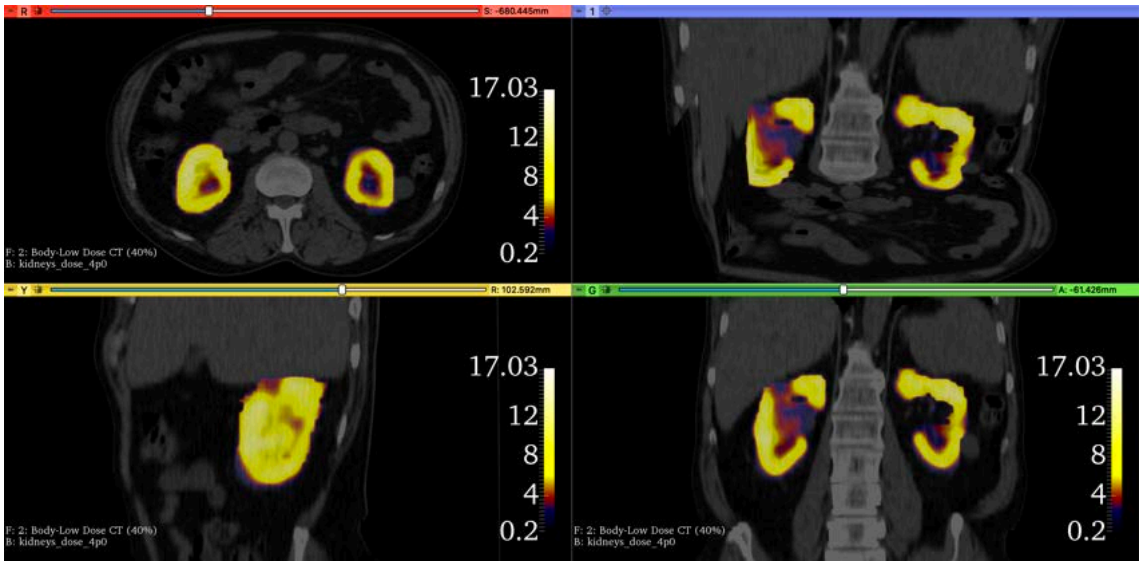

Figure B.13: Representative axial (R), coronal (G), and sagittal (Y) orthogonal slices as well as the 3D view (1) of the absorbed dose distribution in the kidneys of patient 4 in the 3D Slicer software. The scalar bar located on the right in the three images is expressed in mGy.

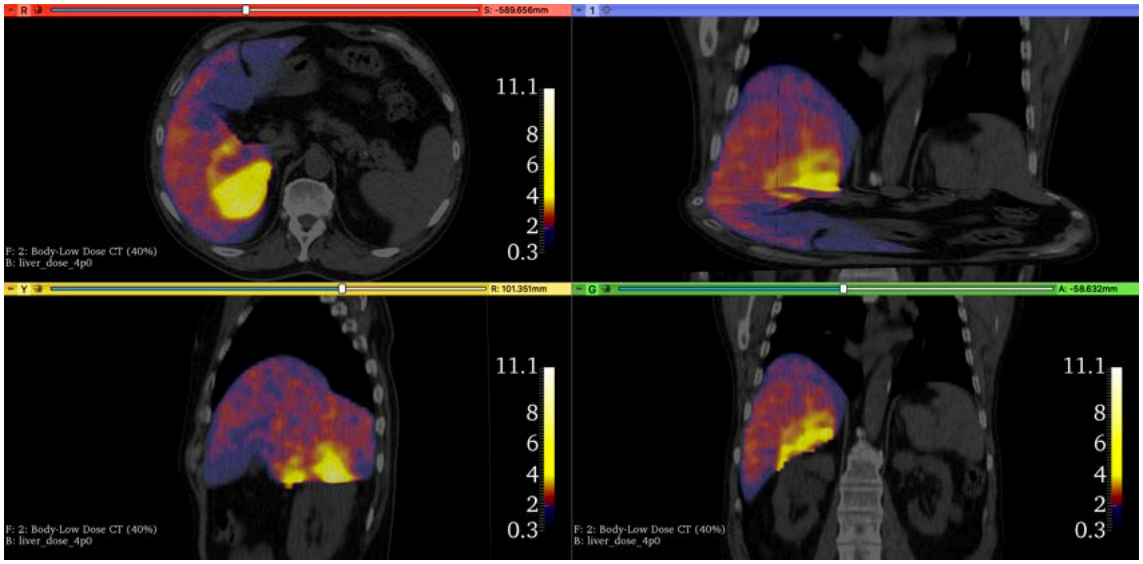

Figure B.14: Representative axial (R), coronal (G), and sagittal (Y) orthogonal slices as well as the 3D view (1) of the absorbed dose distribution in the liver of patient 4 in the 3D Slicer software. The scalar bar located on the right in the three images is expressed in mGy.

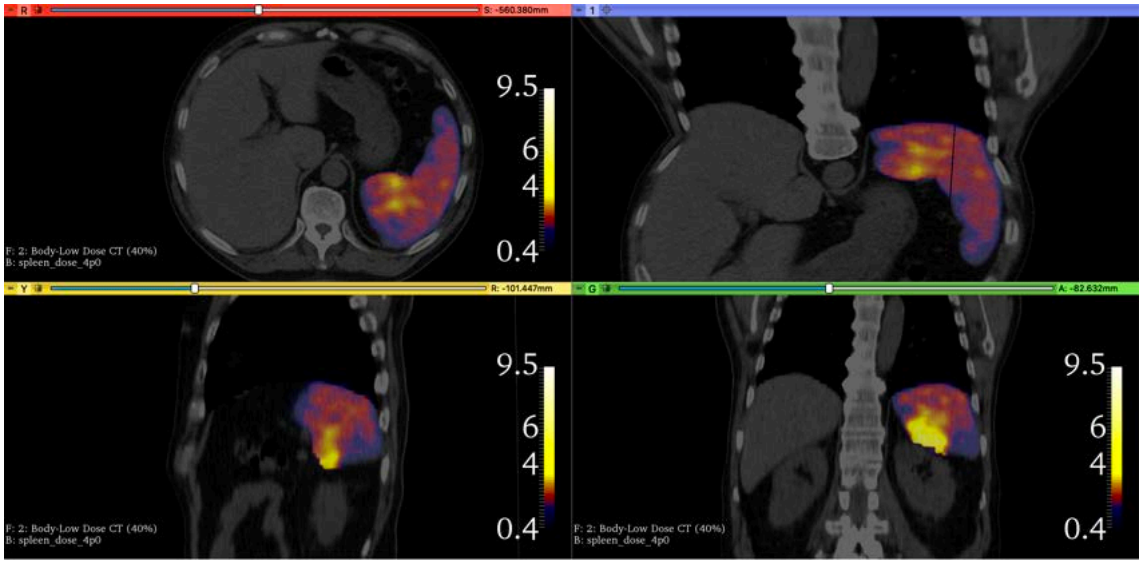

Figure B.15: Representative axial (R), coronal (G), and sagittal (Y) orthogonal slices as well as the 3D view (1) of the absorbed dose distribution in the spleen of patient 4 in the 3D Slicer software. The scalar bar located on the right in the three images is expressed in mGy.

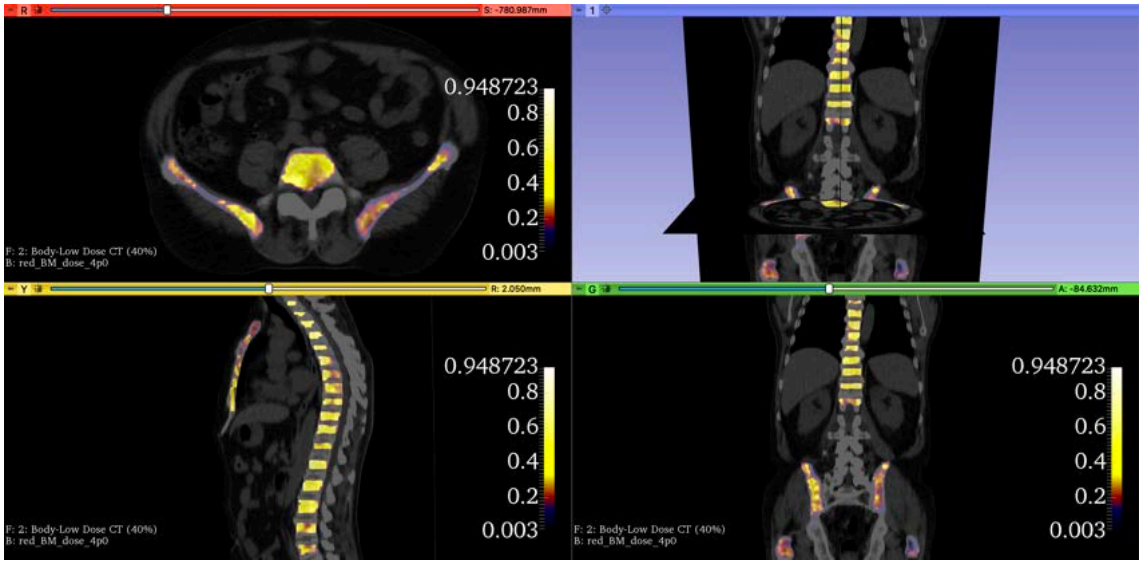

Figure B.16: Representative axial (R), coronal (G), and sagittal (Y) orthogonal slices as well as the 3D view (1) of the absorbed dose distribution in the red bone marrow of patient 4 in the 3D Slicer software. The scalar bar located on the right in the three images is expressed in mGy.

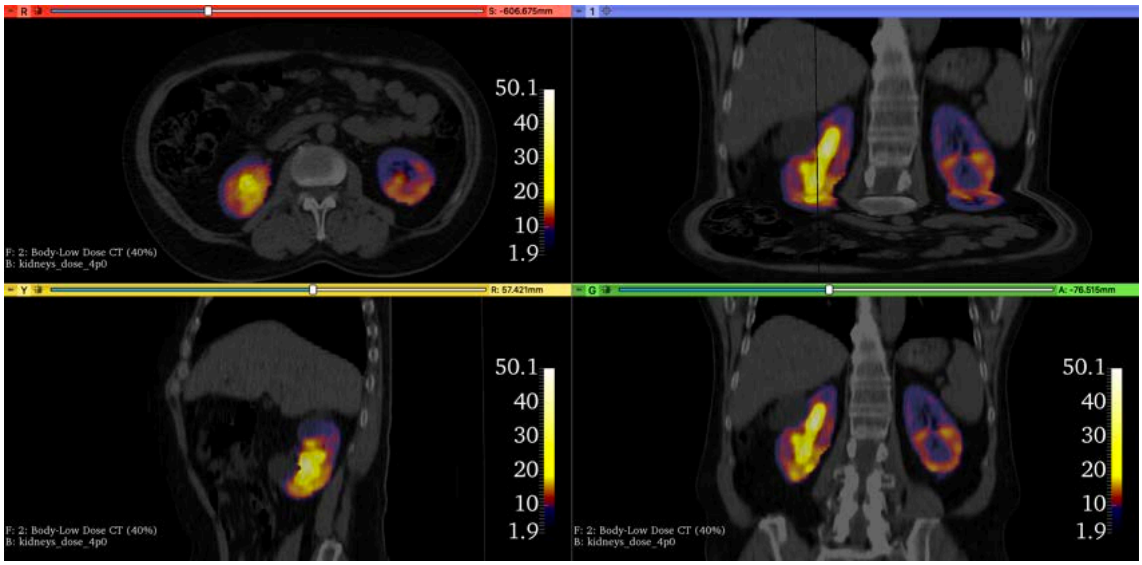

Figure B.17: Representative axial (R), coronal (G) and sagittal (Y) orthogonal slices as well as the 3D view (1) of the absorbed dose distribution in the kidneys of patient 5 in the 3D Slicer software. The scalar bar located on the right in the three images is expressed in mGy.

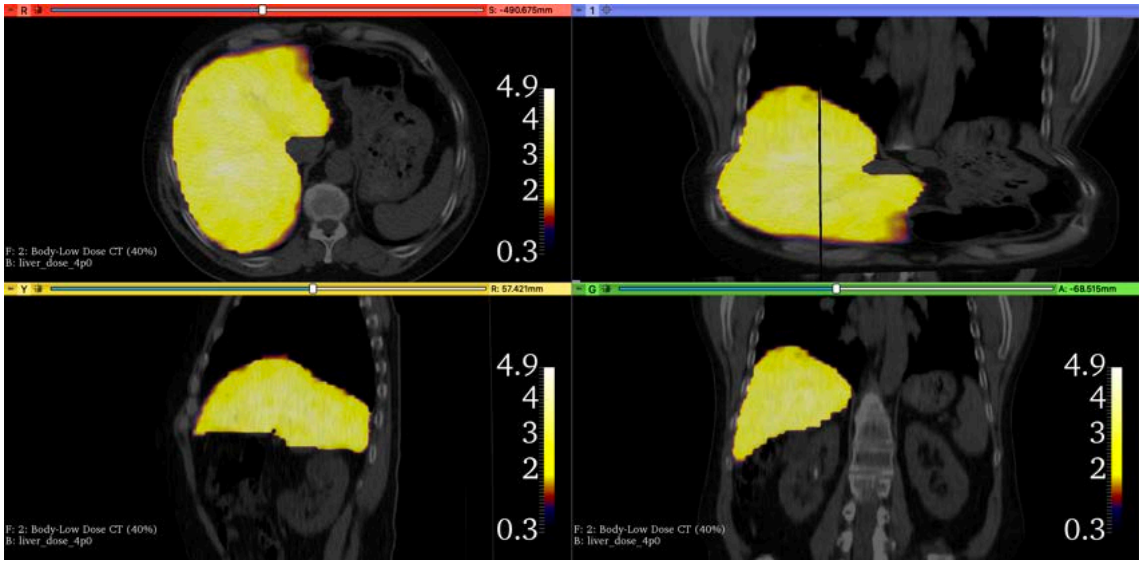

Figure B.18: Representative axial (R), coronal (G), and sagittal (Y) orthogonal slices as well as the 3D view (1) of the absorbed dose distribution in the liver of patient 5 in the 3D Slicer software. The scalar bar located on the right in the three images is expressed in mGy.

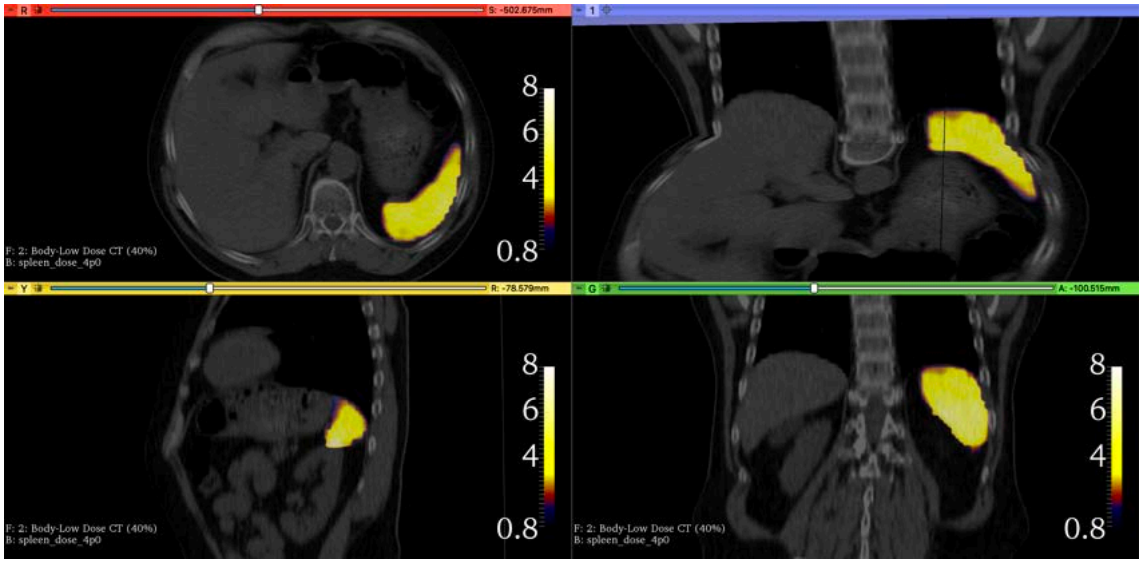

Figure B.19: Representative axial (R), coronal (G), and sagittal (Y) orthogonal slices as well as the 3D view (1) of the absorbed dose distribution in the spleen of patient 5 in the 3D Slicer software. The scalar bar located on the right in the three images is expressed in mGy.

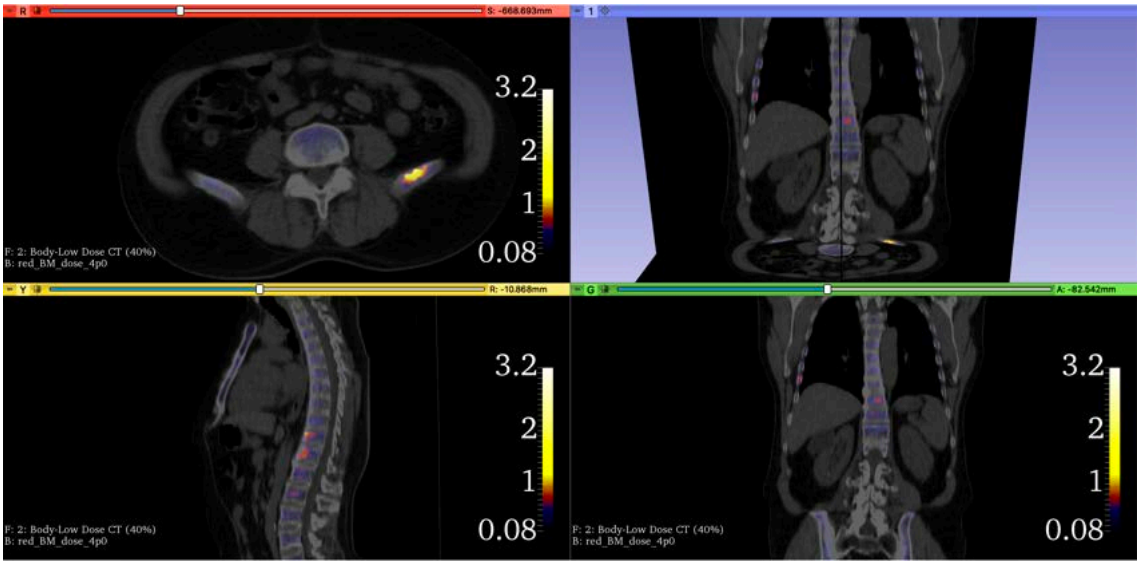

Figure B.20: Representative axial (R), coronal (G), and sagittal (Y) orthogonal slices as well as the 3D view (1) of the absorbed dose distribution in the red bone marrow of patient 5 in the 3D Slicer software. The scalar bar located on the right in the three images is expressed in mGy.

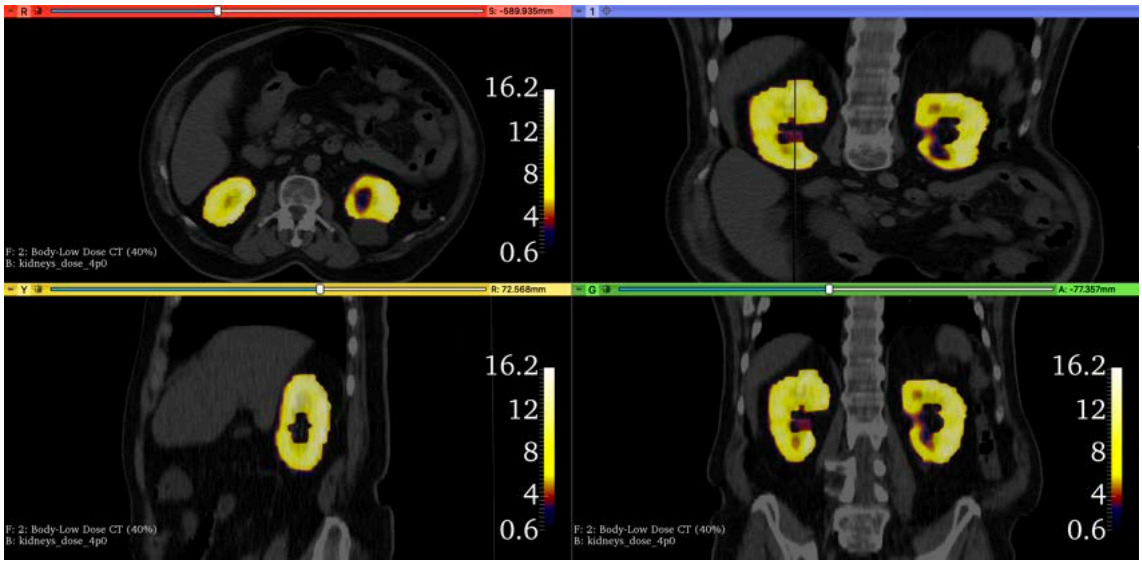

Figure B.21: Representative axial (R), coronal (G), and sagittal (Y) orthogonal slices as well as the 3D view (1) of the absorbed dose distribution in the kidneys of patient 6 in the 3D Slicer software. The scalar bar located on the right in the three images is expressed in mGy.

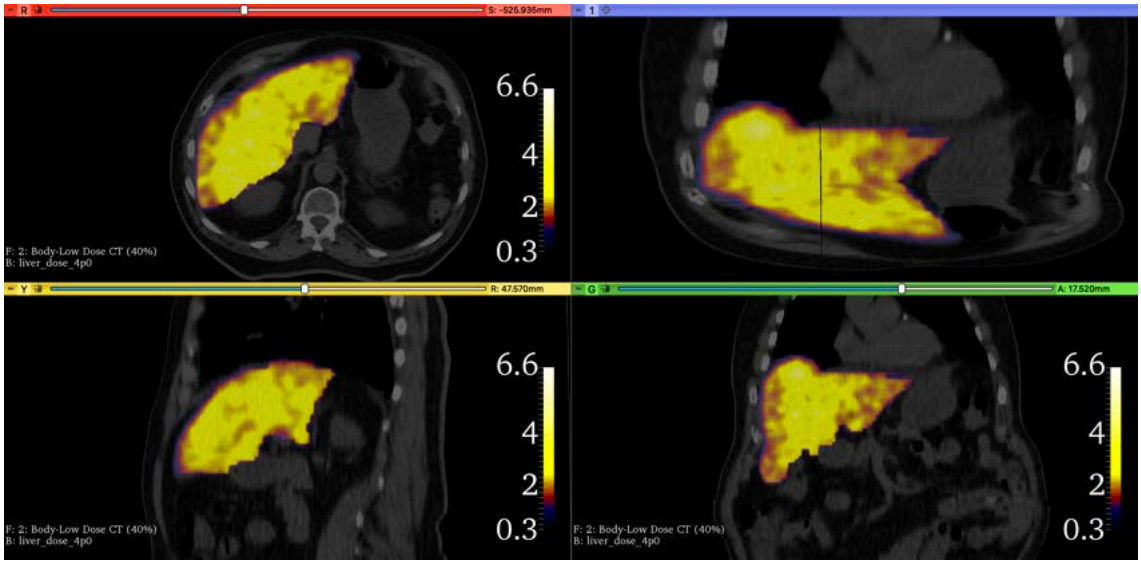

Figure B.22: Representative axial (R), coronal (G), and sagittal (Y) orthogonal slices as well as the 3D view (1) of the absorbed dose distribution in the liver of patient 6 in the 3D Slicer software. The scalar bar located on the right in the three images is expressed in mGy.

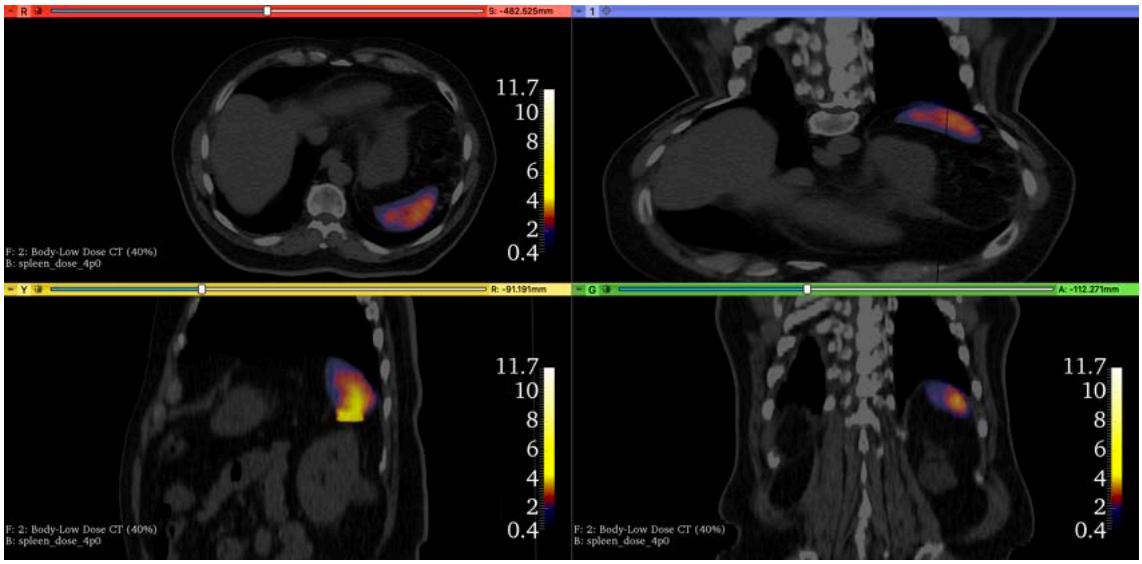

Figure B.23: Representative axial (R), coronal (G), and sagittal (Y) orthogonal slices as well as the 3D view (1) of the absorbed dose distribution in the spleen of patient 6 in the 3D Slicer software. The scalar bar located on the right in the three images is expressed in mGy.

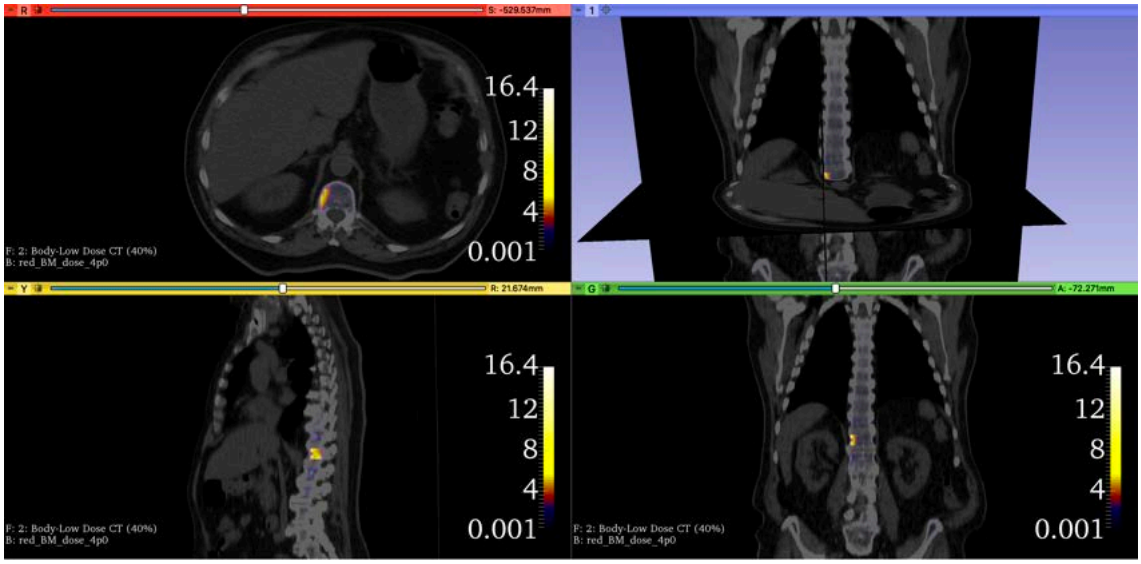

Figure B.24: Representative axial (R), coronal (G), and sagittal (Y) orthogonal slices as well as the 3D view (1) of the absorbed dose distribution in the red bone marrow of patient 6 in the 3D Slicer software. The scalar bar located on the right in the three images is expressed in mGy.

I

Annex 1 – Radiation yields assessment

The ICRP 107 database [124] was used to obtain the spectra and radiation yields of radionuclides. These constituted the input data for the MCNP6.1 Monte Carlo simulations. This annex presents a screenshot of the program where different forms of radiation emitted during the ^{68}Ga decay, and the respective number of ejected particles per type of decay (yield) are reported. This yield component was employed in the S-values weighted sum calculation.

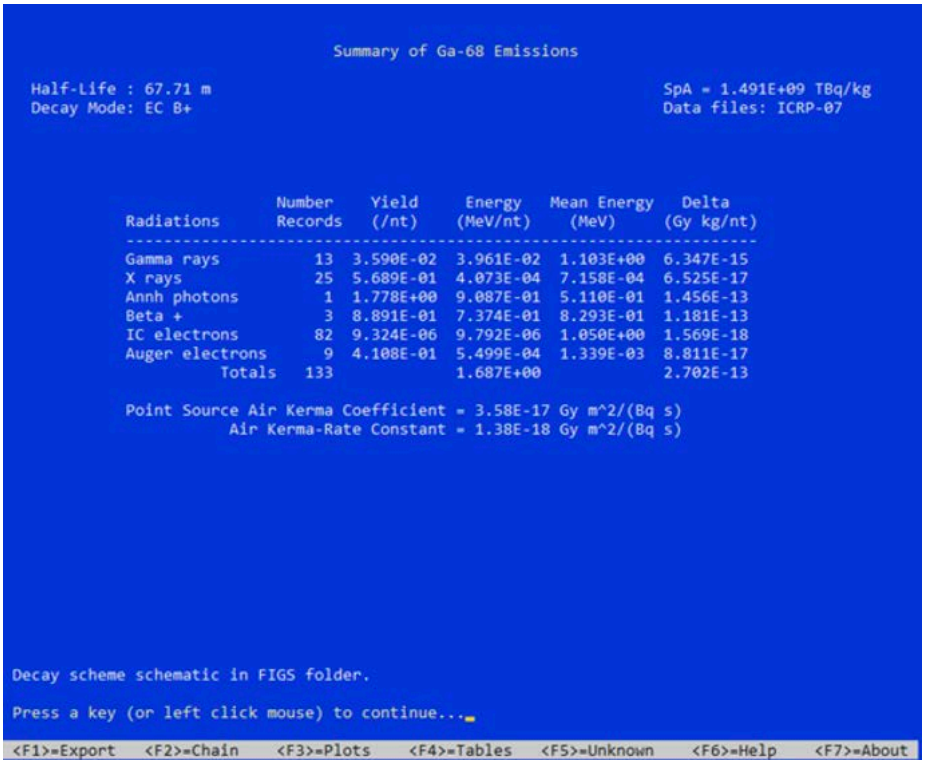

Summary of Ga-68 Emissions

Half-Life : 67.71 m
Decay Mode: EC B+

SpA = 1.491E+09 TBq/kg
Data files: ICRP-07

Radiations	Number Records	Yield (/nt)	Energy (MeV/nt)	Mean Energy (MeV)	Delta (Gy kg/nt)
Gamma rays	13	3.590E-02	3.961E-02	1.103E+00	6.347E-15
X rays	25	5.689E-01	4.073E-04	7.158E-04	6.525E-17
Annh photons	1	1.778E+00	9.087E-01	5.110E-01	1.456E-13
Beta +	3	8.891E-01	7.374E-01	8.293E-01	1.181E-13
IC electrons	82	9.324E-06	9.792E-06	1.050E+00	1.569E-18
Auger electrons	9	4.108E-01	5.499E-04	1.339E-03	8.811E-17
Totals	133		1.687E+00		2.702E-13

Point Source Air Kerma Coefficient = 3.58E-17 Gy m^2/(Bq s)
Air Kerma-Rate Constant = 1.38E-18 Gy m^2/(Bq s)

Decay scheme schematic in FIGS folder.

Press a key (or left click mouse) to continue...

<F1>=Export <F2>=Chain <F3>=Plots <F4>=Tables <F5>=Unknown <F6>=Help <F7>=About